Thesis for the Degree of Doctor of Philosophy

On Modeling and Optimal Control of Modular Batteries

Thermal and State-of-Charge Balancing

Faisal Altaf

Department of Signals and Systems
Chalmers University of Technology
Göteborg, Sweden 2016

On Modeling and Optimal Control
of Modular Batteries
Thermal and State-of-Charge Balancing
FAISAL ALTAF
ISBN 978-91-7597-392-0

Doktorsavhandlingar vid Chalmers tekniska högskola
Ny serie nr 4073
ISSN 0346-718X

Department of Signals and Systems
CHALMERS UNIVERSITY OF TECHNOLOGY
SE–412 96 Göteborg
Sweden

Telephone: +46 (0)31 – 772 1000

Email: faisal.altaf@chalmers.se

Typeset by the author using LaTeX.

Chalmers Reproservice
Göteborg, Sweden 2016

To my parents

Abstract

There has in recent years been an increasing interest in battery-powered electrified vehicles (xEVs) to reduce carbon footprint of transportation and the dependence on fossil fuels. Since the battery pack of xEVs is one of the most expensive but a key component in the powertrain, the battery lifetime is an important factor for the success of xEVs. Thermal and state-of-charge (SOC) imbalance is well known to cause non-uniform ageing in batteries. This thesis formalizes the simultaneous balancing of temperature and SOC, which are two conflicting objectives, using load sharing concept. This concept is realized using a cascaded converter based air-cooled modular battery, which allows cell-level control including cell-shunting. It can be operated using unipolar (UPC) and bipolar (BPC) control modes i.e., two- and four-quadrant module operation. The optimal control problem is to decide the power distribution among battery modules such that the total power/voltage demand is satisfied, all modules remain fairly balanced in terms of SOC and temperature, and physical limits are not violated. In addition to control design, the particular investigations include the requirements on battery control mode and the load intensity/prediction for the problem feasibility, the controller's structural and functional properties to understand and characterize its internal working, and control robustness under parametric variations.

The control problem is formulated offline as a constrained convex quadratic program, which uses the averaged battery electro-thermal model and the full future load information to generate global optimal load distribution as a benchmark for other suboptimal controllers. For online applications with limited future information, a model predictive control (MPC) scheme is proposed for load management under both UPC and BPC modes. It is based on a novel idea of orthogonal decomposition of controller into two additive components namely voltage and balancing controls. The performance is thoroughly evaluated through simulations under various driving situations, prediction horizons, and modeling uncertainty. Using the structural insight offered by the orthogonal control decomposition, two simple computationally efficient control algorithms (so-called projected LQ and gain-scheduled proportional control) are proposed for real-time implementation. These control simplifications reveal two dominant modes of the balancing controller and completely unfold its internal working, allowing its simple rule-based implementation. This study concludes that the UPC mode using one-step state prediction is sufficient to achieve robust balancing performance under most driving situations, which do not demand continuously high load current.

Keywords: Modular batteries, SOC balancing, thermal balancing, battery control, converters, model predictive control, convex optimization, electrified vehicles.

Acknowledgments

The quest for the PhD is like a voyage along highly uncertain path. The diligence and resilience are necessary traits for surviving this uncertainty, but not sufficient for achieving the target within reasonable time. The navigational support and feedback from others is also needed to optimize the trajectory. My quest for the PhD is also no exception in this regard.

I am highly grateful to my supervisor Prof. Bo Egardt for his endless navigational support and encouragement throughout my quest. He has always believed in me and provided me sufficient freedom in my research. His critical feedback helped me improve the technical as well as the structural quality of my thesis significantly. His affability, which always enabled me to have open academic discussions with him, deserves special recognition. I am also thankful to Dr. Lars Johannesson for his useful input and discussion of ideas as my co-supervisor during first three years of my PhD.

I would also like to acknowledge Prof. Anders Grauers for useful discussions on power electronics, Dr. Nikolce Murgovski for his initial help with convex optimization, and Björn Fridholm for discussion on batteries. My special thanks to Chalmers Energy Initiative for funding my PhD and Dr. Helna Holmberg for arranging very interesting events within SHC.

A conducive work environment is a prerequisite for thriving at work and I really feel lucky in this regard. It has been my utmost pleasure to work here during last five years. I would like to thank my all colleagues for enabling a great working environment, in particular Marcus, Hakan, and Claes for all the interesting discussions. My special thanks to Christine, Karin, Madeleine, and Natasha for their excellent administrative support.

I would like to thank my all sincere friends and Prof. Mojeeb-bin-Ehsaan (NUST, Pakistan) for always being a source of great motivation for me.

I have no words to show my deepest gratitude for my respected parents and siblings who have always been supportive and loving throughout my life. I am highly obliged to my wife for her love and patience despite my heavily loaded and unbalanced routine. Last but not least, I feel really blessed to have a lovely daughter Maryam who has added a new unimaginable dimension to my happiness space. My heart resonates with her pleasant smile, a real tranquilizer of my life that relieves my all stress.

List of publications

This thesis is based on the following papers:

Paper 1

F. Altaf, L. Johannesson, B. Egardt. “Simultaneous Thermal and State-of-Charge Balancing of Batteries: A Review,” in *Vehicle Power and Propulsion Conference (VPPC), 2014 IEEE*, pp. 1-7, 27-30 Oct. 2014, Coimbra.

Paper 2

F. Altaf, L. Johannesson, B. Egardt, "On Thermal and State-of-Charge Balancing using Cascaded Multi-level Converters," *Journal of Power Electronics*, vol. 13, Issue 4, pp. 569-583, 2013.

Paper 3

F. Altaf, B. Egardt, L. Johannesson, “Load Management of Modular Battery using Model Predictive Control: Thermal and State-of-Charge Balancing”, *IEEE Transactions on Control Systems Technology*. Accepted Feb. 2016.

Paper 4

F. Altaf, B. Egardt, “Comparative Analysis of Unipolar and Bipolar Control of Modular Battery for Thermal and State-of-Charge Balancing”, *IEEE Transactions on Vehicular Technology*, under second review cycle.

Paper 5

F. Altaf, B. Egardt, L. Johannesson, “Electro-thermal Control of Modular Battery using Model Predictive Control with Control Projections”, in *IFAC Workshop on Engine and Powertrain Control, Simulation and Modeling*, vol. 48, no. 15, pp. 368-375, August 2015, Columbus.

Paper 6

F. Altaf, B. Egardt, “Gain-Scheduled Control of Modular Battery for Thermal and SOC Balancing”, to appear in *IFAC Symposium on Advances in Automotive Control*, June 2016, Norrköping.

Other publications

In addition to these papers, the following papers by the thesis author are related to the topic of the thesis but not included:

F. Altaf, L. Johannesson, B. Egardt. "Evaluating the Potential for Cell Balancing Using a Cascaded Multi-Level Converter Using Convex Optimization," in *IFAC Workshop on Engine and Powertrain Control, Simulation and Modeling*, vol. 3, no. 1, pp. 100-107, Oct. 2012, Paris.

F. Altaf, L. Johannesson, B. Egardt. "Performance Evaluation of Multilevel Converter based Cell balancer with Reciprocating Air Flow," in *Vehicle Power and Propulsion Conference (VPPC), 2012 IEEE*, pp. 706-713, 9-12 Oct. 2012, Seoul.

F. Altaf, L. Johannesson, B. Egardt, "Feasibility Issues of using Three-Phase Multilevel Converter based Cell Balancer in Battery Management System for xEVs," in *IFAC Symposium on Advances in Automotive Control*, pp. 390-397, Sep. 2013, Tokyo.

Contents

Notation

Symbol	Units	Description
$\boxed{\text{Basic}}$		
$\mathbb{R}$	–	Set of real numbers
$\mathbb{R}_+$	–	Set of nonnegative real numbers
$\mathbb{R}^n$	–	Set of real vectors with n elements
$\mathbb{R}_+^n$	–	Set of real vectors with n nonnegative elements
$\mathbb{R}^{n\times m}$	–	Set of real matrices with order $n \times m$
I_n	–	Identity matrix of order $n \times n$
1_n	–	Column n-vector of ones
0_n	–	Column n-vector of zeros
$\|\cdot\|$	–	Euclidean norm
$\|\cdot\|_\infty$	–	Infinity norm
$\|x\|_Q^2$	–	$x^{\mathrm{T}}Qx$
$\lvert\cdot\rvert$	–	Absolute value
m_x	–	mean of a sequence of any variable x
σ_x	–	Std. deviation of a sequence of any variable x
`diag`	–	To denote diagonal matrices
`blkdiag`	–	To denote block-diagonal matrices
$\mathcal{R}$	–	To denote range-space
$\mathcal{N}$	–	To denote null-space
$\boxed{\text{Battery States}}$		
x	–	Battery state vector
ξ	–	SOC vector
ξ_i	–	SOC of Cell_i
T_s	K	Temperature vector
T_{si}	K	Temperature of Cell_i

T_{f0}	K	Coolant temperature at inlet
$\mathcal{X}_{E0}$	–	Set of initial SOCs
$\mathcal{X}_{Eg}$	–	Target set of SOCs
$\mathcal{X}_{T0}$	–	Set of initial temperatures
$\mathcal{X}_{Tg}$	–	Target set of temperatures
Battery Controls		
u	–	Full control vector
u^u	–	Unconstrained full control vector
u^+	–	Positive control vector
u_i^+	–	Positive control/duty of Cell_i
u^-	–	Negative control vector
u_i^-	–	Negative control/duty of Cell_i
u_g	–	SOC control vector
u_ℓ	–	Temperature control vector
u_v	–	Voltage control vector
u_b	–	Balancing control vector
u_b^u	–	Unconstrained balancing control vector
ρ_b	–	Control coefficients of null-space basis vectors
ρ_b^u	–	Unconstrained balancing control coefficients
$\mathcal{U}$	–	Set of feasible control u
$\mathcal{U}_b$	–	Set of feasible balancing control u_b (balancing control polytope)
Q_E/Q_T	–	SOC/Temperature penalty matrix
R_{u_b}	–	Balancing Control penalty
R_{ρ_b}	–	Balancing Control Coefficient penalty
$\bar{P}_x$	–	Terminal state penalty matrix
$K_{u_b}^e$	–	SOC control gain matrix
$K_{u_b}^t$	–	Temperature control gain matrix
$K_{u_b}^f$	–	Inlet temperature compensation gain matrix
$k_{\rho_b}^e$	–	Scalar SOC control gain
$k_{\rho_b}^t$	–	Scalar temperature control gain
h	s	Sampling interval
N	–	Prediction horizon

Balancing Performance Metrics		
$\delta\xi$	–	SOC deviation allowance
$\bar{\xi}$	–	Mean SOC of cells i.e., $\frac{1}{n}\sum_{i=1}^{n}\xi_i$
e_ξ	–	SOC balancing error (cell-to-mean)
$\\|e_\xi\\|_\infty$	–	Maximum cell-to-mean SOC balancing error (*SOC balancing performance metric I*)
Δ_ξ	–	SOC balancing error (cell-to-cell)
$\\|\Delta_\xi\\|_\infty$	–	Maximum cell-to-cell SOC balancing error (*SOC balancing performance metric II*)
δT_s	K	Temperature deviation allowance
$\bar{T}_s$	K	Mean temperature i.e., $\frac{1}{n}\sum_{i=1}^{n}T_{si}$
e_{T_s}	K	Thermal balancing error (cell-to-mean)
$\\|e_{T_s}\\|_\infty$	K	Maximum cell-to-mean thermal balancing error (*thermal balancing performance metric I*)
Δ_{T_s}	K	Thermal balancing error (cell-to-cell)
$\\|\Delta_{T_s}\\|_\infty$	K	Maximum cell-to-cell thermal balancing error (*thermal balancing performance metric II*)
M_e	–	Matrix that maps state to error vector
Battery Variables and Properties		
i_L	A	Battery terminal current
v_L	V	Terminal voltage of modular battery
v_{Li}	V	Terminal voltage of PU_i
P_L	W	Terminal power of modular battery
P_{Li}	W	Terminal power of PU_i
i_{Bi}	A	Terminal current of Cell_i
V_{Bi}	V	Terminal voltage of Cell_i
P_{Bi}	W	Terminal power of Cell_i
i_{Bai}	A	Average current of Cell_i over a switching cycle
i_{Bri}	A	RMS current of Cell_i over a switching cycle
I_{Bai}	A	Average of i_{Bai} over a drive cycle
I_{Bri}	A	RMS of i_{Bri} over a drive cycle
d_{vi}^{+}	V	Terminal voltage of Cell_i under u_i^{+}
d_{vi}^{-}	V	Terminal voltage of Cell_i under u_i^{-}
$C_{ed,i}/C_{ec,i}$	A h	Dischargeable/chargeable capacity of Cell_i

D_v^+	–	Row n-vector of d_{vi}^+:s
D_v^-	–	Row n-vector of d_{vi}^-:s
D_v	–	Row $2n$-vector containing D_v^+ and D_v^-
$\mathcal{N}(D_v)$	–	Null-space of D_v i.e., *battery null-space*
$\mathcal{N}(D_v)^\perp$	–	Orthogonal complement of the null-space
V_n	–	Matrix with basis vectors of the null-space
Battery Parameters		
n	–	Number of cells in the modular battery
v_{oci}	V	Open-circuit-voltage of Cell_i
C_{ei}	A h	Coulomb capacity of Cell_i
R_{ei}	Ω	Ohmic resistance of Cell_i
R_{ui}	KW^{-1}	Convective thermal resistance of Cell_i
C_{si}	JK^{-1}	Heat capacity of Cell_i
a_{tij}	–	Thermal coupling from Cell_j to Cell_i
w_{ti}	–	Influence of T_{f0} on Cell_i
Converter Variables		
s_i	–	Switching function or PWM
s_i^+	–	PWM for left half-bridge inside full-bridge
s_i^-	–	PWM for right half-bridge inside full-bridge
T_sw	s	PWM switching period
F_sw	Hz	PWM switching frequency
Load Variables		
i_L	A	Load current
v_{Ld}	V	Demanded load voltage
P_{Ld}	W	Demanded load power
N_d	–	Discrete time length of a load/drive cycle
Subscripts		
v	–	Refers to variable value under u_v
b	–	Refers to variable value under u_b
i	–	Refers to ith element of a vector
Superscripts		
$+$	–	Refers to variable value under u^+
$-$	–	Refers to variable value under u^-

List of Acronyms

BMS . . . . . Battery Management System
BM . . . . . . Battery Module
BP . . . . . . Battery Pack
BPC . . . . . Bipolar Control mode
BSM . . . . . Battery Submodule
Cell$_i$ . . . . . Cell/Module 'i' inside PU_i
DOD . . . . . Depth-of-Discharge
EM . . . . . . Electric Machine
EOC . . . . . End-of-charge
EOCV . . . . End-of-Charge-Voltage
EOD . . . . . End-of-Discharge
EODV . . . . End-of-Discharge-Voltage
EOL . . . . . End-of-Life
EV . . . . . . Electric Vehicle
FB . . . . . . Full Bridge 'i' inside PU_i
GOC . . . . . Global Optimal Control
HB$_i$ . . . . . . Half Bridge inside PU_i
HEV . . . . . Hybrid Electric Vehicle
LFP . . . . . . $LiFePO_4$/graphite based LIB
LIB . . . . . . Lithium-Ion Battery
LQ . . . . . . Linear Quadratic
MLC . . . . . Multilevel Converter
MPC . . . . . Model Predictive Control
OCV . . . . . Open-Circuit-Voltage
OCV-R . . . OCV in series with Resistance

PHEV . . . . Plug-in Hybrid Electric Vehicle

pLQ . . . . . . Projected LQ

PU$_i$ . . . . . . Power Unit 'i' consisting of HB$_i$/FB$_i$ and Cell$_i$

PWA . . . . . Piecewise Affine

PwGS . . . . Proportional controller with continuous Gain-Scheduling

PWM . . . . Pulse Width Modulation

PwSR . . . . Proportional controller with Simple Rule-based gain-scheduling

QP . . . . . . Quadratic Programming

RF . . . . . . Reciprocating coolant Flow

RMS/rms . . Root Mean Square

SEI . . . . . . Solid Electrolyte Interface

SOC . . . . . State-of-Charge

SOH . . . . . State-of-Health

xEVs . . . . . EV/HEV/PHEV

UDO . . . . . Uniform Duty Operation of cells (duty in terms of time)

UF . . . . . . Unidirectional coolant Flow

UPC . . . . . Unipolar Control mode

USABC . . . US Advanced Battery Consortium

List of Figures

List of Tables

List of Algorithms

Chapter 1

Introduction

1.1 Motivation

1.1.1 Vehicle Electrification

The transportation is going through a critical transition phase to lower dependence on fossil fuels, improve energy efficiency, and reduce CO_2 emissions. The battery-powered electrified/hybridized vehicles (xEVs) are one of the competitive solutions being adopted by automotive industry. The battery is a key component, which helps to downsize or completely eliminate the internal combustion engine (ICE) and may contribute to save fuel cost and reduce emissions. In a conventional vehicle, the kinetic (when going downhill) and braking energies are wasted, whereas the xEVs can store these regenerative energies in the battery and use it later for the propulsion. Thus, the electrification and hybridization of vehicle powertrain is believed to have a positive societal impact due to significant economic and environmental benefits. There are various alternatives like electric vehicles (EVs), hybrid electric vehicles (HEV) and plug-in hybrid electric vehicles (PHEV). The EV is purely electric i.e. no ICE, whereas HEVs and PHEVs use both electric machine (EM) and ICE in a blended fashion to power the wheels. Both EV and PHEV can be charged from the grid. The (P)HEVs may have various component configurations and different levels of hybridization (micro to full), see [1–3] for details. The (P)HEVs (mild electrification) are currently more popular than EVs, which are not being vastly adopted yet due to unavoidable compromise among initial cost, weight, and electric-range owing to immature battery technology.

1.1.2 Conventional Batteries

The conventional battery system of xEVs, shown in Figure 1.1, consists of long string of series connected cells/modules along with dc/dc converter for dc-link voltage regulation and *unidirectional coolant flow* (UF) for heat transfer. A cell is the smallest packaged form of a battery. A battery submodule (BSM) is a collection of two or more series-connected cells, battery module (BM) is a collection of two or more series/parallel-connected BSMs, and a battery pack (BP) is a collection of several BMs connected in series and parallel to meet voltage, energy and power requirements of xEVs.

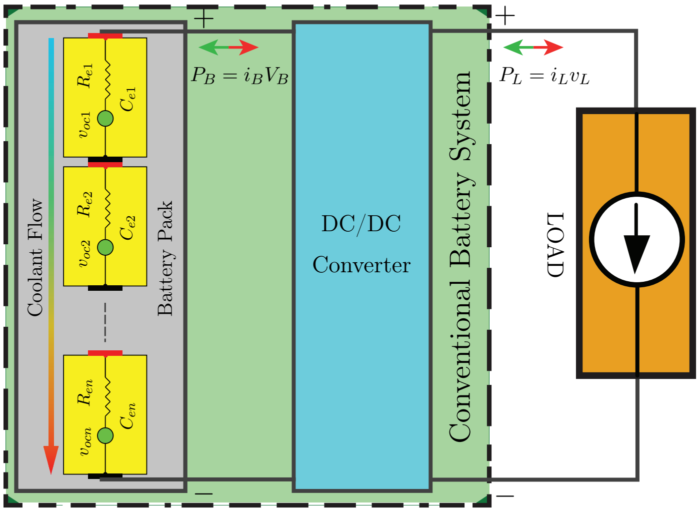

Figure 1.1: Conventional battery with n series-connected battery units and dc/dc converter to regulate dc-link voltage v_L.

The battery pack is one of the most expensive components in the powertrain of xEVs, contributing significantly to the total vehicle cost. The batteries have limited energy capacity, slower refueling/charging capability compared to gasoline, and higher ageing rate (resulting in performance degradation and lower life-time), which may cripple the whole vehicle and add significant extra replacement cost during the vehicle life-time. In addition, batteries also introduce some new safety hazards due to their low thermal stability, especially during direct impact or some other abuse. Due to these issues, the requirements for batteries in automotive applications are much more stringent than those in consumer electronics. The US Advanced Battery Consortium (USABC) has set separate performance goals for EVs(2020), HEVs(2010) and PHEVs(2015) [4–6]. Some of these performance goals are listed in Table 1.1. To address above issues and meet these goals, there has been extensive research on advanced battery materials and

Table 1.1: USABC battery performance goals for HEV, PHEV and EV

Goals at EOL	HEV (2010)	PHEV (2015)	EV (2020)
Cost ($/system)	500 – 800	1700 – 3400	4000
Pulse Disch. Power (kW)	25 – 40	38 – 50	80
Available Energy (kWh)	0.3 – 0.5	3.5 – 11.6	30 – 40
Cycle-life	300000	3000 – 5000	750
Calendar-life @30° (yrs)	15	15	10
Operat. Temp. ($°C$)	-30 to $+52$	-30 to $+52$	-40 to $+50$
Battery Sys. Wt. (kg)	60	70	200
Battery Sys. Vol. (L)	45	46	133
Max. Self-discharge	50 Wh/day	50 Wh/day	$<$ 15%/mon

electrochemical processes over last few decades [7–9]. As a result of these efforts, nickel metal hydride (NiMH) and lithium-ion battery (LIB) systems are two dominant technologies today for xEV applications. For example, NiMH has been successfully employed in HEVs (Toyota Prius I), whereas LIB is used in EVs (Tesla) and PHEVs (Toyota Prius II, Volvo V60 etc.). The LIBs, due to their relatively higher specific energy and longer cycle-life, are currently emerging as the major choice for future xEVs [9–12]. However, there is still a large room for improvement regarding cost, energy density, ageing, calendar-life, safety, reliability, and charging rate to meet all USABC requirements. Therefore, the quest for new materials is still going on to achieve the long term sustainable goal of full electrification. See [1,6,8,13] for further discussion on battery requirements for xEVs.

The health and ageing rate of Li-ion cells, like all other cell chemistries, is greatly affected by various factors like SOC level, depth-of-discharge (DOD), temperature, and c-rate etc [14–18]. The cells in the string being stored or cycled at higher SOC-level, DOD and temperature age faster than those at lower SOC, DOD, and temperature. Therefore, thermal, SOC, and DOD imbalances in a battery pack may cause nonuniform ageing of cells. The analysis of nonuniform ageing in Li-ion packs is given in [19]. Another serious issue is that the cell imbalance and nonuniform ageing are tightly coupled, which may lead to a vicious cycle: imbalance causes nonuniform ageing, which in turn causes even more imbalance and so on. If this cycle continues, it may severely affect the performance of a battery pack, resulting in significant reduction of its lifetime due to premature failure of only one cell in the string, regardless of the high state-of-health (SOH) of other cells. In addition, the SOC imbalance also has a detrimental impact on the total usable battery capacity. Therefore, thermal and SOC imbalance can be considered as an indirect indication of either temporary or permanent health imbalance among cells.

Thermal, SOC and DOD imbalance is inevitable in batteries of xEVs. The thermal imbalance is mainly caused by variations in internal resistances of cells and significant temperature gradient in the battery coolant [20–23]. The SOC imbalance is primarily caused by variations in capacities, leakage currents, and operating conditions of cells, whereas the DOD imbalance occurs as a result of the SOC and capacity imbalance. It is also pertinent to mention here that the the parametric variations are not negligible even in fresh cells of a same batch [20]. These variations may enhance further with time due to nonuniform ageing of cells in the absence of balancing. For example, consider a conventional battery pack, as shown in Figure 1.1, with parametric variations (nonuniform state-of-health) among its cells. Due to the fixed series connection, the same current passes through all the battery units. This is a so-called *uniform duty operation* (UDO) of cells. In this situation, the battery units may suffer from unequal stress, unequal energy drain, over-charging, and over-discharging, which can cripple the whole battery pack. Thus, thermal and SOC balancer is very critical for optimal performance of automotive batteries. It is also worth mentioning here that the potential of used automotive battery packs (so-called second life batteries) is being investigated for smart grid energy storage applications [24]. The need of thermal and SOC balancer may be even more critical in such applications due to very high probability of large variance in parameters of these second-life batteries.

Due to above mentioned issues, LIBs need a battery management system (BMS) with advanced control and monitoring. In this regard, the systems and control community have shown a lot of research interest in recent years, see for example [25–41]. The overall goal is to develop a knowledge base to design *battery health-conscious BMS* (power management algorithms) for optimal utilization of currently available cells to guarantee their long and uniform lifetime in large-scale energy storage applications like xEVs and smart grids. The BMS, consisting of hardware and software, monitors battery voltage, current, and temperature. Using these measurements, it performs SOC and parameter estimation to give indicators about remaining fuel and health status as battery ages. These indicators are then used to predict available battery power (both charging and discharging) at any time instant. Once the energy and power limits of battery are known, the BMS controls power flow into/out of the battery pack to guarantee optimal, reliable, and safe operation (i.e. to respect voltage, current, and temperature limits). In addition, the BMS uses this information to perform several other important functions like SOC balancing, control of coolant for thermal management, and fault detection and diagnosis. The SOC balancing can be achieved using various types of passive or active SOC balancers, see [42–46], whereas thermal balancing may potentially be achieved using active cooling with *reciprocating air-flow* (RF) i.e. frequently changing the direction of coolant flow to reduce thermal gradient in the coolant, see [23].

The notion of *simultaneous thermal and SOC balancing* using a single active balancing device is the main focus of this thesis, which according to the best of our knowledge has not been studied thoroughly before. This study has also inspired some preliminary work on this topic by other authors [47]. Thermal and SOC balancing are two tightly coupled and somewhat conflicting objectives, but we argue in this thesis that it is possible to achieve both simultaneously in an *average sense.* For this, load variations and surplus voltage in the battery pack are required. Also, a special balancing device that enables the *non-uniform load sharing/scheduling* among cells, is needed.

1.2 Modular Battery and Load Sharing

The *modular battery system*, shown in Figure 1.2, based on cascaded multilevel converter(MLC) [48] is a potential candidate for simultaneous thermal and SOC balancing purpose. The modular battery consists of n cascaded power units (PUs), each containing an isolated smaller battery module and a switching dc/dc converter, which can be externally controlled. This can be viewed as splitting a single large conventional battery system, shown in Figure 1.1, into n smaller controllable cascaded subsystems. Due to this special architecture, the modular battery is reconfigurable to generate a range of terminal voltage $v_L(t) = \sum_{i=1}^{n} v_{Li}(t) \in [0, v_{L,\max}]$ [or terminal power $P_L(t) = i_L(t)v_L(t)$] for a variable load with known power demand $P_{Ld}(t) = i_L(t)v_{Ld}(t)$, where $v_{Li}(t) \in \{-V_{Bi}, 0, +V_{Bi}\}$ is the terminal voltage of PU_i, V_{Bi} is the terminal voltage of battery module, i_L is the load current, and v_{Ld} is the demanded load voltage. It provides a large redundancy in the voltage synthesis, which gives extra degrees-of-freedom in control. This enables *control of bidirectional flow of power* P_{Bi} (P_{Li}) from each battery module (PU_i), making it possible to independently manipulate the state (SOC and temperature) of each module to achieve state balancing/synchronization/consensus, which is the main focus of this thesis. In addition, this modular architecture also provides a great opportunity to do *distributed battery management and cooling* at the module level, but this aspect has not been investigated in this study.

There are various dc/dc converter topologies like full-bridge, half-bridge, buck-boost etc. that can be employed inside PUs. Depending on the topology, we propose two types of battery control modes, namely *unipolar* and *bipolar* control modes. The unipolar control (UPC) mode does not allow polarity inversion of any module in the string, which implies that at any time instant, either all modules are charging or all are discharging (i.e. $\mathrm{sgn}(P_{Bi}) = \mathrm{sgn}(P_{Bj}), \forall i, j$) depending on the direction of load power P_L. On the other hand, the bipolar control (BPC) mode allows polarity inversion of some modules in the string, which implies that, at any time instant, it is possible to charge some modules while discharging others (i.e. $\mathrm{sgn}(P_{Bi}) \neq \mathrm{sgn}(P_{Bj})$ for some i and j) regardless of load power direction. The UPC only needs half-bridge converter with single unipolar pulse-width modulation (PWM) inside each module, whereas the BPC needs four-quadrant operation of full-bridge converter using three-level bipolar PWM (generated using two unipolar PWMs) inside each module.

The concept of modular battery is also studied recently by other authors for xEVs [49–54], smart grid energy storage [55,56], and three-phase electric drive applications [57,58]. However, only SOC balancing and voltage control problems are addressed at most in these studies. The modular battery control proposed in this thesis targets multiple conflicting control objectives including thermal balancing, SOC balancing, and dc-link voltage regulation for the first time. This requires a more advanced control algorithm to decide power flow from each module. In addition, many interesting research questions around simultaneous balancing of SOC and temperature as well as the balancing control structure are also formally investigated.

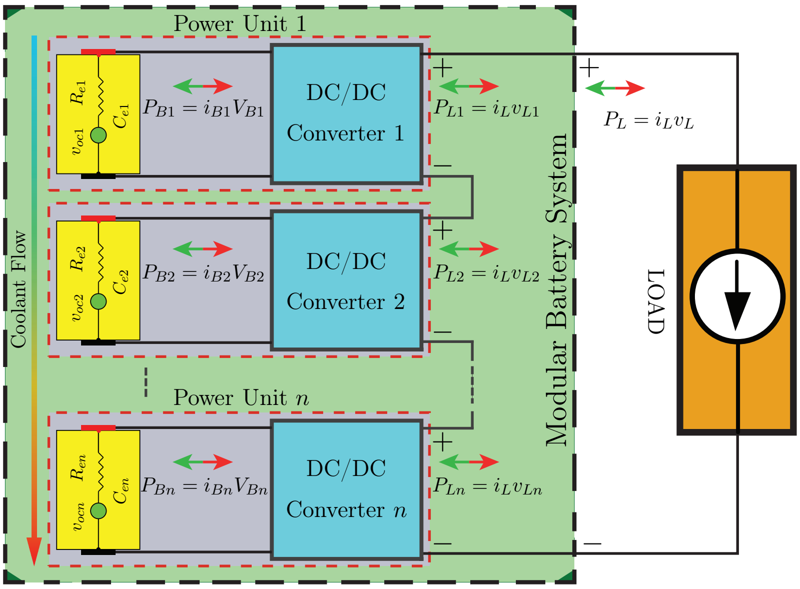

Figure 1.2: Modular battery with n cascaded power units/modules, each with its own dc/dc converter and isolated battery module/cell.

1.3 Problem Description

The control problem of modular battery boils down to the *load sharing or load management problem* as stated below.

Problem 1. *The optimal control problem of switched modular batteries is to decide, at each time instant, the power flow P_{Bi} out of (or into) each switched battery module without violating its physical (power and actuation) limits such that the total driving (or regenerating) power demand P_{Ld} is satisfied (i.e., $P_L(t) = P_{Ld}(t)$) and all modules remain fairly balanced in terms of SOC and temperature.*

The main goal is to satisfy the total power demand without draining out (SOC imbalance) and over-stressing (thermal imbalance) any single battery unit, thereby increasing the battery lifetime. Since cells are assumed to have variations in parameters (*health imbalance*) and operating conditions, the equal loading of battery modules ($P_{Bi} = P_{Bj}$) is not a good policy for optimal battery performance as discussed before. This thesis proposes multiple optimal control policies for the above problem while addressing the following specific research questions:

Q1. About problem feasibility:

- **a.** Is the control objective feasible? What are the requirements?
- **b.** Which battery control mode (UPC or BPC) is needed for this objective? What are the requirements for each?
- **c.** What is the effect of load power profile (i.e. driving behavior) on balancing performance?

Q2. About global optimal control solution:

- **a.** How to design a model-based control algorithm, which gives global optimal solution for the above problem? Can this be formulated as a convex optimization problem?
- **b.** Does it give any significant benefit compared to uniform duty operation (UDO) of cells?
- **c.** How does the choice of cooling scheme (UF or RF) affects the control performance?

Q3. About control design using limited future load information:

- **a.** How to design a model-based predictive controller to solve the above problem using limited future load information?

  b. How long future load demand forecast is needed to achieve acceptable balancing performance? Is it possible to achieve this using only current load demand?

Q4. About control analysis and characterization:

  a. What are the structural and functional properties of the optimal control scheme?

  b. How sensitive/robust is the control scheme to parametric uncertainties and variations?

  c. Are voltage and balancing control tasks separable?

  d. How to interpret the total control in terms of voltage and balancing control actions?

  e. How the controller behaves in various load ranges to achieve trade-off between temperature and SOC control objectives?

Q5. About control simplification and implementation in large packs:

  a. How to approximate the optimal control solution as a computationally efficient standard linear quadratic (LQ) *control policy* for fast implementation in large battery packs?

  b. Can we design a simple proportional or rule-based control scheme for fast embedded implementation?

In this thesis, we propose various optimal control methods with decreasing complexity, which makes the control problem and its solution more transparent and accessible. This enables us to progressively investigate the above questions in the rest of this thesis.

1.4 Thesis Outline and Contributions

The outline and the specific contributions of each chapter are given below.

Chapter 2

In this chapter, the basic working principle and ageing phenomena of lithium-ion cells are reviewed first, and then the effects of thermal and SOC imbalance among cells in a battery pack are discussed. This chapter motivates simultaneous thermal and SOC balancing by thoroughly reviewing the negative impact of thermal and SOC imbalance on battery's lifetime and its total capacity. This chapter is based on Paper 1 and [59].

Chapter 3

This chapter develops a control-oriented electro-thermal model of a single cell in an air-cooled battery pack for both unidirectional (UF) and reciprocating (RF) coolant flows. This model is used as a basic building block for deriving a full state-space model of the modular battery in Chapter 4. In addition to the cell model, this chapter also adds some preliminary discussion on the cell-level battery control for simultaneous thermal and SOC balancing. Thermal and SOC balancing are two tightly coupled objectives. However, we give simple arguments to show that it is possible to achieve these simultaneously by using a load sharing concept (health-conscious scheduling of cells' duties) in the modular battery (**Q1.a**). However, this non-uniform load sharing requires cell redundancy (voltage surplus) in the battery. In addition, it is favorable to have brake regeneration phases and load variations (mix of high and low load intensity) in the drive cycle. This chapter is mainly based on Paper 1 and Paper 2.

Chapter 4

This chapter formally presents the architecture and the averaged state-space electro-thermal model of the switched modular battery. First, two proposed control modes of the modular battery namely UPC and BPC are properly defined, and then the averaged model is derived carefully to get convex model under both modes. The model is used to formulate the load management problem of the modular battery as convex optimization problem (**Q2.a**) in Chapter 5. In addition, a preliminary comparison between UPC and BPC is also added (**Q1.b**). We argue, using simple analytical expressions and graphical illustrations, that the BPC improves the controllability properties of the modular battery system, which may make it easier to achieve simultaneous thermal and SOC balancing compared to that under UPC, which requires load variations. However, the BPC may require higher cell redundancy in the modular battery compared to that for UPC. This chapter is based on Paper 3 and Paper 4.

Chapter 5

In this chapter, the load management problem of the MLC-based modular battery is formulated as a state and control constrained convex optimization problem. The optimization problem is solved offline using perfect information of the battery state as well as of the complete future driving cycle. Therefore, it renders globally optimal control (GOC) solution for load sharing among modules (**Q2.a**). The solution is tested in simulations for a modular battery with parametric variations among its cells. The main research task in these simulations is to investigate if the GOC gives any significant benefit compared to UDO (**Q2.b**). We also investigate the potential benefits of RF for thermal balancing performance of GOC (**Q2.c**). Results show that the optimal policy under unidirectional coolant flow, exploiting the extra degree-of-freedom of modular battery, provides significant reductions in temperature and in SOC deviations compared with UDO. The GOC has no significant gain from reciprocating coolant flow for short battery strings. This chapter is based on Paper 2 and Paper 3.

Chapter 6

In this chapter, we propose a novel model predictive control (MPC) scheme to solve the load management problem of the modular battery in both UPC and BPC modes for cases where full future driving information is not accessible (**Q3**). The control scheme is based on decomposition of controller into two orthogonal components, one for *voltage control* and the other for *balancing control* (**Q4.c**). The voltage control decisions are made separately using a simple minimum norm problem, whereas the balancing problem is formulated on control constrained linear quadratic (LQ) form. This novel problem decomposition enables the application of constrained linear quadratic model predictive control scheme to elegantly solve the balancing problem (**Q3.a**). In addition, it adds a lot of insight into balancing control structure and its interpretations. The balancing controller acts as charge and heat shuffler (power redistributor) using information about battery state, load current, and voltage control decisions (**Q4.a**, **Q4.d**). It forms virtual resistance/capacity to compensate for resistance/capacity imbalance among cells. The control scheme is thoroughly evaluated through simulations of a four cell modular battery. The results show that a one-step prediction horizon is sufficient to achieve robust control performance under benign to normal driving behaviors with short load power pulses of varying intensity (**Q1.a**, **Q1.c**, **Q3.b**). We also analyze and compare the UPC and BPC operation of the modular battery in terms of their balancing performance as well as energy efficiency (**Q1.b**). This analysis is done particularly for aggressive driving cycles, which generate continuously high load current and thus pose some challenges for UPC. The simulation results show that BPC, without even need of load current variations, gives better balancing performance than UPC, but at the cost of reduced efficiency. The UPC requires at least current direction reversal for acceptable balancing performance. Therefore, looking over multiple charge/discharge cycles, the UPC is a promising solution due to higher energy efficiency and lower cost. This chapter is based on Paper 3 and Paper 4.

Chapter 7

In this chapter, we simplify the balancing controller (**Q5**) of Chapter 6. We propose to solve the balancing control problem in two simple stages (i.e. two sub-problems) instead of solving a single control-constrained LQ problem at each step of MPC. In the first stage, unconstrained optimal balancing control decisions are made based on *unconstrained LQ control policy* (**Q5.a**) and in the second stage the control constraint is handled via *projection* of unconstrained controls on control constraint set (polytope). This new method (so-called *projected LQ* MPC scheme) of solving balancing problem is fast as it is based on a simple Riccati recursion and projections. This control scheme also adds more insight into properties of MLC-based thermal and SOC balancer and offers some nice interpretations (**Q4.a**, **Q4.d**, **Q4.e**). The control algorithm is investigated in a simulation study of a four cell modular battery and compared with constrained LQ MPC of Chapter 6. Results show that this simplified control scheme has high computational efficiency without any significant compromise on balancing performance. The control analysis also shows that the projection stage is rarely needed if the SOC imbalance and/or the load demand is not too high, further reducing the computational time. The performance and the computational efficiency of the control algorithm make it attractive for real-time implementation in large battery packs. This chapter is based on Paper 5.

Chapter 8

Chapter 8 proposes a constrained proportional balancing controller (**Q5.b**) with simple gain scheduling. This balancing controller is devised by investigating structural properties of constrained LQ MPC introduced in Chapter 7. This investigation reveals a particular factorization of time-varying control gain matrices, which leads to approximation of matrix gains as scalar gains under the assumption of small parametric variations among battery cells. The gains are scheduled in load current for nominal cells. This special structure enables the identification of two dominant operational modes (**Q1.c**) of the balancing controller: SOC balancing mode in low to medium load current range and thermal balancing mode in high current range. This study also proposes a simple algorithm for control projection on constraint polytope. The proposed balancing controller is tested in simulations for a modular battery with four significantly mismatched cells. The controller shows balancing performance comparable to MPC, which uses true battery parameters, but has much higher computational efficiency. The simplicity of the controller makes it attractive for real-time implementation on small embedded hardware. This chapter is based on Paper 6.

Chapter 9

The proposed control algorithm is verified on a large battery pack (sized for Toyota Prius PHEV) through simulations. The main purpose is to show the scalability (**Q5**) of our complete control design methodology (including functional and structural properties) with increased pack size and large thermal gradient in the battery coolant. The control performance is tested under both UF and RF. The simulation results show that our control design is scalable with battery size and adds significant benefit under both UF and RF. In particular, it is also shown that the control performance (thermal balancing) is improved under RF in long battery strings (**Q2.c**).

Short Summary of Thesis Contributions

The main contributions of this thesis in short:

- Simultaneous balancing of temperature and SOC using load sharing/scheduling/management concept has been formalized for the first time according to the best of our knowledge.

- An averaged state-space electro-thermal model of air-cooled switched modular battery has been developed. The averaging has been carefully done to preserve model convexity under both UPC and BPC modes.

- The load management problem of the modular battery has been formulated as a constrained convex optimization problem, which uses full load information to generate global optimal load distribution among battery modules. The balancing performance has been thoroughly evaluated and used as a benchmark for other suboptimal controllers.

- An MPC scheme has been proposed to solve the battery load management problem in both UPC and BPC modes for cases where full future load information is not accessible. The control scheme is based on a novel idea of orthogonal decomposition of controller into two additive components, namely voltage and balancing controls.

- The MPC performance has been thoroughly evaluated under various driving situations and load prediction horizons. It is concluded that the UPC mode using one-step state prediction is sufficient to achieve good balancing performance under most urban and rural driving situations, which do not demand continuously high load current. The structural and functional properties of the controller have also been investigated to understand and characterize its internal working.

- Using the structural insight offered by the orthogonal control decomposition, two computationally efficient control algorithms have been proposed for real-time implementation in large battery packs. The first one (so-called projected LQ) solve the balancing control problem in two simple stages (unconstrained LQ + control projection). The second simplified controller (gain-scheduled control) has been proposed by investigating the structural properties of two-stage projected LQ controller. These control simplifications revealed two dominant modes of the balancing controller and completely unfolded its internal working, allowing simple rule-based implementation of the balancer.

Contributions Outside the Thesis

In addition to the above contributions, the author of this thesis also analyzed the concept of 3-ϕ MLC-based modular battery as *integrated cell balancer and motor driver*. In particular, the extra heating and the capacity fading of battery modules due to dc-link current ripple in 3-ϕ MLC are thoroughly analyzed and compared to the case of 3-ϕ two-level converter. It is concluded that, from battery's health viewpoint, it is unpromising to promote 3-ϕ MLC as an integrated cell balancer and a motor driver in xEVs unless some active compensation technique is used to filter the ripple. These results are presented in the following paper, which is not included in this thesis.

> F. Altaf, L. Johannesson, B. Egardt, "Feasibility Issues of using Three-Phase Multilevel Converter based Cell Balancer in Battery Management System for xEVs," In *IFAC Symposium on Advances in Automotive Control*, pp. 390-397, Sep. 2013, Tokyo.

Chapter 2

Lithium Ion Cells: Preliminaries

A battery cell stores energy in the form of chemical energy contained in the atomic bonds of its active materials and converts it to electrical energy by the mean of electrochemical redox reaction, which occurs on two electrodes when the external circuit is connected between them [60]. There are various kinds of batteries with main differences in their active materials and performance characteristics [see Appendix A for the basic terminology]. In this chapter, the main working principle, ageing mechanisms, the effect of various factors on ageing rates, and the balancing issues of lithium-ion battery (LIB) cells are thoroughly reviewed. The need of simultaneous thermal and SOC balancing is highlighted by thoroughly discussing the negative impact of thermal and SOC imbalance on battery's lifetime and its total capacity. The various types of cell balancing techniques are also reviewed.

2.1 Cell Working

The LIB consists of negative and positive porous electrodes, also known as anode and cathode respectively, the porous separator, the concentrated solution of electrolyte, and the current collectors. The most commonly used negative electrode is the lithiated graphite (LiC_6) and the most commonly used positive electrodes are metal oxides such as $LiCoO_2$, $LiMn_20_4$, and $LiFePO_4$ etc. The most commonly used electrolyte consists of the solution of lithium salt ($LiPF_6$) in a mixed organic solvent. This organic liquid electrolyte is embedded into the porous electrode. The copper and aluminium are commonly used as current collectors for negative and positive electrodes respectively. The LIB works based on intercalation reaction, which is briefly described below, see [31, 32, 34, 60] for details.

Intercalation reaction, a type of insertion reaction, is the process of moving guest ions (Li^+ in the LIB case) into and out of the interstitial sites in the host lattice. The electrodes, which can store charged species through intercalation process, are called intercalation (or insertion) electrodes. The intercalation electrodes commonly have layered structure and the charged species gets sandwiched between these layers during the intercalation process. In the LIB, the charged species which intercalates in the electrodes are lithium-ions (Li^+) and that is why they are named as lithium-ion batteries. The capacity of intercalation electrodes is limited by the number of interstitial sites, which can be occupied by charged species, in their lattice structure. Thus, the intercalation-based LIBs have less capacity than pure lithium-metal batteries. However, the great advantage with LIBs is that the host material does not suffer from any major structural changes during intercalation process. Thus, LIBs have much higher cycle life compared to lithium-metal batteries. Moreover, due to the absence of highly inflammable lithium metal, LIBs are much safer than lithium-metal batteries.

In a LIB both electrodes can act as hosts to store lithium ions. During charging process, the oxidation reaction occurs at the positive electrode and consequently the lithium atom stored in the positive electrode increases its oxidation state by losing an electron to the external circuit. The lithium-ions move out of the interstitial sites of the positive electrode and travel, through the electrolyte phase by the process of diffusion and ionic conduction, into the interstitial sites of the negative electrode and the electrons, on the other hand, move through the external circuit to the negative electrode. On the negative electrode, the lithium-ions get reduced and intercalated in the graphite to form Li_yC_6. During discharging, the whole process is reversed. Thus, in the fully charged state all the lithium-ions are hosted in the negative electrode and in the discharged state they are all hosted inside the positive electrode. The total energy stored in the LIB at any time instant is given by the difference in energy of intercalated lithium in positive and negative electrodes. The following reactions occur at the electrodes of any LIB. Note that, in these reactions, $LiMO_2$ represents some lithium metal oxide positive material such as $LiCoO_2$ (M=Co) and C represents some carbonaceous negative material such as graphite (C_6).

$$\mathrm{LiMO_2} \underset{\text{Discharge}}{\overset{\text{Charge}}{\rightleftharpoons}} \mathrm{Li_{1-x}MO_2} + \mathrm{x\,Li^+} + \mathrm{x\,e^-} \qquad \text{(Positive Electrode Reaction)}$$

$$\mathrm{C} + \mathrm{y\,Li^+} + \mathrm{y\,e^-} \underset{\text{Discharge}}{\overset{\text{Charge}}{\rightleftharpoons}} \mathrm{Li_yC} \qquad \text{(Negative Electrode Reaction)}$$

$$\mathrm{LiMO_2} + \frac{x}{y}\,\mathrm{C} \underset{\text{Discharge}}{\overset{\text{Charge}}{\rightleftharpoons}} \frac{x}{y}\,\mathrm{Li_yC} + \mathrm{Li_{1-x}MO_2} \qquad \text{(Total Cell Reaction)}$$

2.2 Cell Ageing

LIBs, like all other battery types, age with time both during storage and cycling. The ageing processes inside a cell result in energy capacity fade, power fade, and increase in self-discharge rates [14, 17, 31]. The capacity and power fades are defined below.

- Capacity fade is the loss of ability of an electrode's active mass to store or deliver the electrical charge. The capacity fade in LIBs is primarily caused by the loss of cyclable active lithium and reduction in interstitial sites in the lattice structure of the active material due to structural degradation, mainly, of anode [17, 61].

- Power fade is primarily caused by the internal resistance growth of a cell. There are various kinds of resistances in a cell and the resistance increase may be in one or all of them. The resistance may grow due to many mechanisms including degradation of current collectors, degradation of coating (which is used for electronic conduction in active mass), the degradation of binding interface between electrode and current collectors, the growth of extra resistive passivation film on electrodes, and loss of ionic conductivity in the electrolyte.

The capacity and power fading generally have different origins, but they also have some common electrochemical and mechanical ageing factors. The actual degradation mechanisms behind these effects are very complex, tightly coupled and still not very well understood. The ageing rate is highly dependent on electrode materials and the properties of electrolyte and additives.

2.2.1 Types of Ageing Mechanisms

The ageing mechanisms on anode and cathode are different [14]. There are various reasons of ageing but one main cause is the electro-chemical side reactions, which occur inside a cell in addition to the main intercalation reactions. These side reactions result in side-products, which consume the active material of a cell [62]. Some of these side reactions are completely reversible whereas others are irreversible. The irreversible side reactions result in permanent power and energy capacity fade of the battery and occur both on anode and cathode. In the following, we give a brief overview of the most important ageing mechanisms in anode and cathode and the various factors that accelerate the cell ageing. For details see [14–16, 63, 64].

Ageing Effects on Anode

The thermodynamical stability of the anode is the most critical factor for battery ageing. The lithiated graphite (LiC_6) anode lies below the lower limit of thermodynamic stability window of organic electrolytes [62]. It results in the strong reactivity between anode and the electrolyte which makes the organic electrolyte solvents highly susceptible to side reduction reaction at anode. This side reaction is on the form [15, 29, 63]

$$\mathrm{S} + \mathrm{Li}^{+} + \mathrm{e}^{-} \longrightarrow \mathrm{P} \tag{2.1}$$

where S refers to the solvent species and P is the product of this side reaction. The side reaction (2.1) is irreversible and thus results in capacity fade due to the loss of cyclable lithium. This side reaction occurs first during the cell formation process and forms a passivation film by depositing P on the solid-electrolyte interface (SEI) [63]. This initial passivation film is called *SEI layer*. The thickness of SEI layer should not increase, as it increases the ohmic resistance and results in power fade. In order to prevent the side reaction (2.1) from continuing further, the electrons from anode must not reach the molecules of electrolyte. Thus, the SEI layer must be fully permeable to lithium-ions but must act as a perfect electronic insulator. However, due to defects in SEI layer, the side reaction may continue on anode. This deposits precipitates on initial SEI layer and increases its thickness. This extra resistive film on SEI layer results in power fade. The side reaction also causes the corrosion of lithium in the anode which results in the capacity fade due to irreversible loss of cyclable lithium. Thus, the side reaction (2.1) is believed to be one of the main ageing mechanism on the negative electrode. Therefore, the ageing and proper operation of a LIB is highly dependent on the *stability of SEI layer*. The extra resistive film formed on SEI has temporal and spatial variations. The film growth rate is a function of cell SOC and the charging current [29]. Table 2.1 shows the main ageing mechanisms on anode, their effects and the factors affecting ageing rates, see [16] for further details.

Ageing Effects on Cathode

The ageing of positive electrode during cycling mainly occurs due to its volume variations. The volume increases during intercalation and decreases during de-intercalation of lithium. These repeated cycles of intercalation and de-intercalation cause strain in the active material particles and they may lose contact with the conductive additive network within the composite electrode [15]. Thus, the structural degradation is believed to be the main ageing mechanism in cathode. In addition, the cathode also has

Table 2.1: Main ageing mechanisms on lithiated carbon anode [see [16] for details]

Cause	**Effect**	**Leads to**	**Reduced by**	**Enhanced by**
Electrolyte reduction side reaction (Electrolyte Decomposition)	Loss of Lithium, Impedance rise	Capacity fade, Power fade	Stability of SEI layer	High Temperature, High SOC
Decrease in accessible surface area due to SEI film growth	Impedance rise	Power fade	Stability of SEI layer	High Temperature, High SOC
Changes in anode porosity due to volume changes and SEI film growth	Impedance rise, polarization losses	Power fade	Stability of SEI layer	High cycling rate, High SOC
Contact loss of active material particles due to volume changes during cycling	Loss of active material	Capacity fade	—	High cycling rate, High DOD
Corrosion of Current Collector	Impedance rise, polarization losses	Power fade	—	Over-discharge, Low SOC
Metallic lithium deposition and subsequent decomposition of electrolyte	Loss of lithium, loss of electrolyte	Capacity fade, Power fade	—	Charging at low temperatures, High cycling rate

strong oxidizing properties against the electrolyte solvent. Thus, cathode ageing may also occur due to electrochemical side oxidation reaction. The positive electrodes in LIBs normally operate close to the upper limit of thermodynamical stability of organic electrolytes. Since, during cell formation process, nothing like SEI protective layer forms on positive electrode, even the slight over-charge may trigger furious oxidation reaction between electrolyte solvent and the cathode. This may result in fire and explosion due to gas evolution, especially in lithium cobalt oxide based LIBs. The side oxidation reaction between cathode and electrolyte decomposes the electrolyte and forms the precipitates, which block the interstitial sites in the lattice of positive electrode. This leads to capacity fade due to the loss of active material in the cathode and electrolyte decomposition. The decomposition of electrolyte also forms passivation film on cathode, which increases the ohmic resistance and leads to power fade. The capacity and power fade in cathode is accelerated at higher temperature and SOC.

2.2.2 Ageing Conditions

In the view of battery's mode of utilization, the ageing can be divided into two main categories: the calendar ageing and the cycle ageing as described below. The ageing during cycling and rest are commonly considered *additive*, but complex interactions may occur as well [15].

Calendar Ageing

Calendar ageing is the proportion of irreversible capacity loss that occurs with time, especially during storage. During storage, the ageing is mainly governed by the thermodynamical stability of electrodes and separator etc in the electrolyte. The loss of cyclable lithium due to side reactions and SEI film growth at anode have been reported as the main source of ageing during storage [14, 65]. Cell ageing and self-discharge rate during storage highly depends on storage conditions. Thus, the ageing of battery can be controlled by choosing optimal storage conditions. The cell storage temperature and SOC level are two main factors, which strongly influence the rate of calendar ageing. High storage temperature accelerates side reactions on SEI and corrosion of current collectors, whereas too low temperature facilitates the lithium deposition on anode. Similarly, high SOC level also facilitates side reactions on SEI. Thus, thermal and SOC imbalance during storage will cause nonuniform ageing of cells in a battery pack. The effect of temperature and SOC on battery ageing is not additive [66, 67]. The calendar ageing is a nonlinear function of time, temperature and SOC.

Cycle Ageing

The ageing of a battery also occurs with each charge/discharge cycle, so-called cycle ageing. The main ageing mechanisms during cycling are changes in the porosity of electrodes [15] and the contact loss of active material particles due to volume variations of both anode and cathode. On anode, the SEI layer may crack due to volume changes during cycling, which is then automatically repaired by consuming available lithium and thus results in capacity fade [15]. On cathode, the volume variations induces the contact loss between particles of active material and the conductive additive network. Thus, the structural degradation of the active material is considered the main cause of ageing during cycling [65]. The cycle ageing is greatly influenced by battery operating temperature, SOC level, DOD, cycling frequency (or rate), and c-rate. Higher values of these variables accelerate the cycle ageing and thus reduce the cycle-life of a battery [14–17].

2.2.3 Cycle-life Model

The estimation of battery ageing is quite challenging due to highly intertwined internal and external stress factors (temperature, SOC level, DOD, c-rates etc). The ageing of batteries in real xEVs during operation is complicated further by the varying operating environment and the utilization mode. There are various estimation methods including phenomenological approach, which uses electrochemical model of battery processes [63,68–70], equivalent-circuit-model based approach [18,71], and the performance-based approach [72]. The performance-based approach uses battery performance metrics like energy capacity or power capacity to assess the age of a battery. The loss in performance is indicated by either capacity loss or resistance growth (power loss). A performance-based cycle-life model is given by [17, 73]

$$\Delta E_0 = B(c) \cdot \exp\left(\frac{-E_a(c)}{R \cdot T}\right) \cdot (A_h)^{0.55} \text{ with } B(c) = 10000 \left(\frac{15}{c}\right)^{1/3} \tag{2.2}$$

where ΔE_0 is the percentage of energy capacity loss of the cell w.r.t the cell's initial capacity $E_0(0)$, $E_a = (31700 - 370.3 \times c)\,\mathrm{J\,mol^{-1}}$ is the electrode reaction activation energy, c is the c-rate, R is the ideal gas constant, T is the lumped cell temperature, A_h is the ampere-hour throughput that represents the total amount of charge processed (delivered or absorbed) by the battery during cycling, and B is a c-rate dependent coefficient. The capacity fade model given by eq. (2.2) can be used to predict the capacity loss for a given A_h and c-rate.

2.3 Cell Imbalance

Let us consider a conventional battery pack, as shown in Figure 1.1, consisting of n series-connected cells, Cell_1 to Cell_n. In this study, we assume parametric imbalance among these cells i.e., we have

$$C_e = \begin{bmatrix} C_{e1} & \cdots & C_{en} \end{bmatrix}^{\mathrm{T}}, \tag{2.3}$$

$$R_e = \begin{bmatrix} R_{e1} & \cdots & R_{en} \end{bmatrix}^{\mathrm{T}}, \tag{2.4}$$

$$\xi(0) = \begin{bmatrix} \xi_1(0) & \cdots & \xi_n(0) \end{bmatrix}^{\mathrm{T}}, \tag{2.5}$$

which contain nonuniform capacities, resistances, and initial SOCs of cells respectively. These variations may result in cell imbalances i.e. imbalance among cell temperatures as well as *dischargeable* and *chargeable* capacities of cells. These aspects are discussed further in this section.

2.3.1 Impact of SOC Imbalance

If a battery pack has no balancing device then it may develop SOC variations among its cells. In this case, the charging is stopped when any cell in the string reaches its fully charged state (i.e., its end-of-charge-voltage (EOCV)) and similarly the discharging is stopped when any cell in the string reaches its fully discharged state (i.e., its end-of-discharge-voltage (EODV)). This SOC imbalance has a detrimental impact not only on the battery ageing but also on its total effective capacity as discussed below.

Reduction of Battery Capacity

In the following, we discuss the relationship of capacity and SOC of a battery pack with those of its constituent cells/units. Assuming that all the cells have zero leakage current, the time-varying *dischargeable capacity* and *chargeable capacity* of each cell are given by

$$C_{ed,i}(k) = \xi_i(k) C_{ei}, \quad C_{ec,i}(k) = \left(1 - \xi_i(k)\right) C_{ei}. \tag{2.6}$$

Since there is SOC and capacity imbalance among cells, cells may have imbalance among their dischargeable capacities and chargeable capacities as well i.e. we have

$$C_{ed}(k) = \begin{bmatrix} C_{ed,1}(k) & \cdots & C_{ed,n}(k) \end{bmatrix}^{\mathrm{T}}, \tag{2.7}$$

$$C_{ec}(k) = \begin{bmatrix} C_{ec,1}(k) & \cdots & C_{ec,n}(k) \end{bmatrix}^{\mathrm{T}}, \tag{2.8}$$

for a battery with n series cells. Under these imbalances, the *effective capacity* and SOC of the battery are given by [72–75]

$$C_{\mathrm{B}}(k) = C_{\mathrm{B},d}(k) + C_{\mathrm{B},c}(k), \tag{2.9}$$

$$\xi_{\mathrm{B}}(k) = \frac{C_{\mathrm{B},d}(k)}{C_{\mathrm{B}}(k)}, \tag{2.10}$$

respectively, where

$$C_{\mathrm{B},d}(k) = \xi_{\mathrm{B}}(k)C_{\mathrm{B}}(k) = \min_i(C_{ed,i}(k)), \tag{2.11}$$

$$C_{\mathrm{B},c}(k) = (1 - \xi_{\mathrm{B}}(k))\, C_{\mathrm{B}}(k) = \min_i(C_{ec,i}(k)), \tag{2.12}$$

are remaining dischargeable and chargeable pack capacities respectively. From the above equations, the capacity, $C_{\mathrm{B}}(t)$, and SOC, $\xi_{\mathrm{B}}(t)$, of the battery can not be easily related to the capacity and SOC of any single cell in the battery. Thus, in order to simplify the expressions, let us first assume that the battery is either in fully charged state ($\xi_{\mathrm{B}} = 1 \Rightarrow C_{\mathrm{B},c} = 0$) or in fully discharged state ($\xi_{\mathrm{B}} = 0 \Rightarrow C_{\mathrm{B},d} = 0$) and then define

$$C_{\min} = \min_i\{C_{ed,i} | \xi_{\mathrm{B}} = 1\} \quad \text{or} \quad C_{\min} = \min_i\{C_{ec,i} | \xi_{\mathrm{B}} = 0\}. \tag{2.13}$$

Now, we can see that the total capacity and SOC of the battery depends entirely on the capacity and SOC of a certain Cell_k that has minimum dischargeable (chargeable) capacity in the whole string at fully charged (discharged) state of the battery.

Let us now consider a simple example of unbalanced battery pack shown in Fig. 2.1. It contains two cells with equal self-discharge currents, but Cell_1 has higher capacity than Cell_2. The battery is depicted in the fully charged

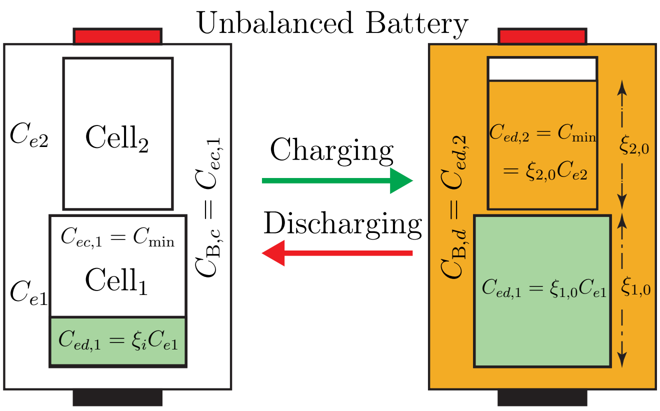

Figure 2.1: Unbalanced battery: Illustration of the impact of SOC imbalance. Note variations in cell capacities, initial cell SOCs, and the DODs.

and fully discharged state on the right and left hand sides of the figure respectively. During charging, Cell_1 will hit its fully charged state before Cell_2 and the battery cannot be charged further for safety reasons, despite of available chargeable capacity of Cell_2. This implies under-utilization of Cell_2. Similarly, during discharge process, as soon as Cell_2 will hit the fully discharged state, battery will stop discharging despite of remaining dischargeable capacity in Cell_1 and hence will result in its under-utilization. Thus, none of these cells are fully utilized during charge/discharge cycle. Note that $C_{\min}$, shown in the figure, is a function of SOC and capacity imbalance. For instance, in this particular case, the total battery capacity, $C_{\mathrm{B}} = C_{\min} = \xi_2(0)C_{e2}$, is a function of $\xi_2(0)$ and C_{e2}. If Cell_2 is not fully charged when the battery is fully charged (i.e. $\xi_2 \neq 1$ if $\xi_{\mathrm{B}} = 1$) then the C_{B} will only be a fraction of C_{e2}. In the worst case (i.e. $\xi_2(0) \ll \xi_1(0)$), C_{B} will be very low. Therefore, SOC imbalance can greatly reduce the total effective battery capacity.

Non-uniform Battery Ageing

As shown in Fig. 2.1, cells in the unbalanced battery cycle at different DODs ($\text{DOD}_1 = 0.68 < \text{DOD}_2 = 0.85$). In addition, each cell starts its cycle at different initial SOC-level. Since DOD and SOC-level affects the cell ageing rate, cells of unbalanced batteries suffer from nonuniform ageing. Since the lifetime of the battery is upper bounded by the fastest cell ageing rate in the string, an unbalanced battery may reach its end-of-life sooner due to the weakest link in the chain.

2.3.2 Impact of Thermal Imbalance

Temperature strongly influences capacity and power fading rates of cells as shown in Table 2.1. In particular, according to the cycle-life model (2.2), the capacity loss is exponential in temperature. Therefore, even a small temperature imbalance among cells over a long term may lead to significant non-uniform ageing. For example, in a conventional battery of xEVs as shown in Figure 1.1, cells with higher resistance (hot spots) and/or higher ambient temperature (downstream cells) may age faster than others. Since the lifetime of a battery is primarily defined by the ageing rate of its hottest cell, thermal imbalance may result in premature death of a battery pack. Therefore, thermal balancing, in addition to SOC balancing, of xEV packs is necessary to enhance their life-time. See [21–23] for a detailed review of thermal issues in lithium-ion batteries of xEVs.

2.4 Cell Balancing

The above discussion shows that SOC and thermal balancing is very critical for optimal performance of automotive batteries. In this section, we give a short review of various SOC and thermal balancing techniques.

2.4.1 SOC Balancing

SOC balancing is one of the most important functions of any advanced BMS, especially for long series string of cells. It improves not only the non-uniform ageing but also the total capacity of the battery. The significance of cell SOC balancing in large battery packs has been studied thoroughly in the literature, see [44, 76–78]. The SOC balancer requires an external circuit to interact with each cell in a string. The external circuit can be dynamically reconfigured to provide the dissipative or non-dissipative alternate paths for direct energy flow between various cells in a string. In the following, we discuss two main types of SOC balancers.

Passive Balancers

The passive balancer achieves cell equalization either by over-charging or by burning in shunt-resistors the excess charge of cells. It equalizes the SOC among cells only once, commonly at fully charged state of a battery, during a charge/discharge cycle [74, 78]. Since the passive balancing device at most consists of only resistors, it can not be actively controlled externally. Thus, it does not require any complicated control algorithm except charge control. However, it is dissipative and is therefore less efficient. Moreover, cells of a passively balanced battery are not equally utilized over whole charge/discharge cycle. Since cells cycle at different DODs, they may suffer from non-uniform ageing [79]. Note that this method can only be used for lead-acid and NiMH batteries due to their tolerance against over-charge conditions [42, 44].

Active Balancers

The active cell balancers use external switched circuits to actively transfer (shuttle, shuffle, shunt, or redistribute) the energy among cells of a battery to achieve SOC balancing. The active balancing network commonly consists of switches and energy storage elements, like capacitors and inductors, which provide alternate paths for energy flow. Therefore, active cell balancers are highly energy efficient due to their non-dissipative nature and they can also be actively controlled using an external controller. However, they generally require more advanced control algorithms, which may get quite complex for large battery packs. The active cell balancer is the only viable solution for a lithium-ion pack, because it cannot tolerate over-charging [42, 44, 80]. There are various active balancing methods like cell shunting, cell-to-cell, cell-to-pack, pack-to-cell and cell-to-pack-to-cell, see [42, 50] for further details on balancing hardware and see [81] for optimization-based thorough performance evaluation of various balancing methods.

The capacity and SOC of an ideal *actively balanced battery pack* is always given by the mean value of the cells' capacities and SOCs [72–75] i.e.,

$$C_{\mathrm{B}} = \frac{1}{n}\sum_{i=1}^{n} C_{ei}, \quad \xi_{\mathrm{B}} = \frac{\sum_{i=1}^{n} C_{ed,i}}{\sum_{i=1}^{n} C_{ei}}. \tag{2.14}$$

All cells are equally utilized in terms of their DODs. Therefore, an actively balanced battery is able to deliver higher Ah-throughput before its end-of-life. Thus, in order to maximize the capacity and to decelerate the ageing of a battery, the *use of an active balancer is desirable* [79].

2.4.2 Thermal Balancing

The purpose of thermal balancing is to reduce the highest cell ageing rate in a battery at the cost of slightly increasing the temperature (and hence the ageing rates) of other cells. Thermal imbalance in large battery packs can potentially be mitigated using the following two approaches.

Reciprocating Airflow

Unidirectional coolant flow (UF) is commonly used in battery packs. However, this cooling scheme leads to thermal imbalance among cells due to temperature gradient in the coolant. Reciprocating coolant flow (RF) scheme has been suggested in [23] to solve this issue. In this scheme, the coolant flows back and forth in the battery pack at a fixed reciprocating frequency. The frequency can be tuned to improve temperature uniformity. However, RF cannot solve imbalance arising from variation in cell resistance or variation in its other parameters like thermal resistance. For example, let us consider a four cell battery pack where cell 4 has 50% higher resistance than other cells, which have uniform characteristics. Each cell in the pack is equally loaded under US06 drive cycle. Figures 2.2(a) and 2.2(b) show the temperature evolution of each cell under UF and RF respectively. It can be seen that the RF, compared with UF, has reduced thermal imbalance among first three cells due to temperature gradient in the coolant, but it fails to achieve temperature uniformity for cell 4 that has higher resistance.

These figures clearly indicate that RF alone cannot solve the temperature non-uniformity problem in battery packs because it is quite unlikely to have a pack with identical cells.

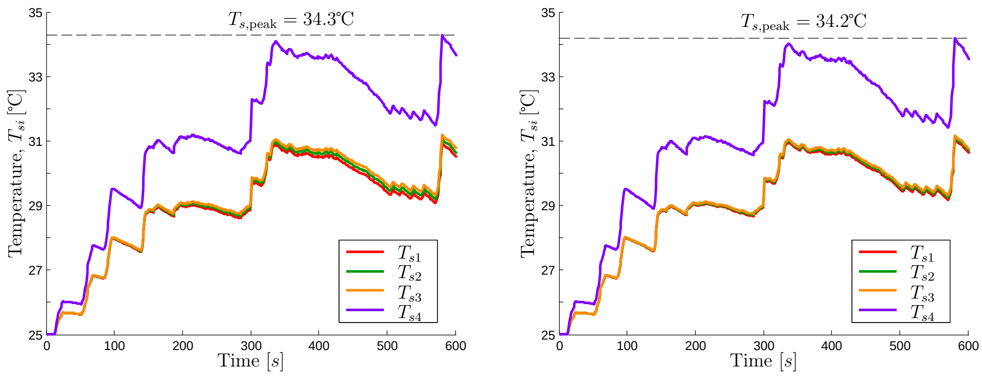

(a) Temperature evolution under UF. (b) Temperature evolution under RF.

Figure 2.2: Thermal balancing: comparison between UF and RF

Load Scheduling/Sharing/Management

In this study, we propose to achieve thermal balancing by equalizing losses among cells using load scheduling/management concept. In this method, cells in the string are used according to their thermal state. In simple terms, the load of the weakest link in the whole chain is shared by other cells. Thus, it has a full potential to compensate thermal imbalance due to both coolant temperature gradient and parametric variations. In addition, the load sharing concept is equally useful for SOC balancing purpose by discharging/charging each cell according to its remaining dischargeable/chargeable capacity ($C_{ed,i}/C_{ec,i}$). Therefore, the load sharing method opens up a window of opportunity for simultaneous thermal and SOC balancing. However, it requires a special hardware, which should

- be modular and distribute a battery into n smaller units.
- enable the *bypassing of the load current* around each cell.
- allow non-uniform use of cells.

The modular battery [Figure 1.2] meets all these requirements. In the rest of this thesis, we develop various model-based control algorithms to solve the load management problem (Problem 1 on page 7) of this modular battery.

2.5 Summary and Conclusions

This chapter underscores the need of thermal and SOC balancing to achieve longer battery lifetime and higher effective capacity. It is shown that RF cooling scheme alone cannot achieve thermal balancing among cells with significant resistance imbalance. In this regard, the importance of load sharing concept is emphasized for simultaneous thermal and SOC balancing.

Chapter 3

Cell Model and Control

In this chapter, a control-oriented electrothermal model of a cell in an air-cooled battery pack is presented. To prepare ourselves for a more formal study in upcoming chapters, a preliminary discussion on the battery load management problem (model-based cell-level battery control) for simultaneous thermal and SOC balancing is also added. It is shown that these two objectives are tightly coupled and their simultaneous feasibility requires an advanced control policy for optimal load sharing among cells. In addition, some specific characteristics of the load profile required for achieving these objectives are also discussed. The feasibility question is discussed using simple arguments without going into any mathematical intricacies.

3.1 Cell Model

There are two major types of cell models, namely physics-based electrochemical models and grey-box models with lumped parameters. The physics-based dynamic models are purely based on actual physical and chemical processes occurring inside a cell, whereas in the grey-box type models, the input-output experimental data of a cell is fitted to a parameterized model with known model structure. The physics-based models give better prediction of the cell behavior. However, they pose very high computational burden, due to the system of coupled partial differential equations, which renders them quite inconvenient for real-time control applications. An enthusiastic reader is referred to some great references [25, 32, 34, 82, 83] for further study on physics-based models. In BMS applications, it is normally sufficient to know the response of battery SOC, temperature, and terminal voltage to changes of the external input current. Therefore, equivalent circuit models are commonly used. Although the battery characteristics are distributed in nature, the electrical I-V characteristics can be approximated fairly well by using lumped electrical component models. In the following, we present electro-thermal dynamics of a cell using equivalent circuit modeling approach. The model is built based on the following assumptions:

- The electrical model is based on the *simple cell model* (OCV-R i.e. open-circuit-voltage in series with resistance) [84], which is one of the most widely used model for supervisory control in xEVs. In this model, dynamic losses due to activation and concentration polarizations are neglected. A comprehensive review of various equivalent circuit electrical models is given in [84].

- The thermal model is based on lumped capacitance and flow network modeling approach, see [23] and [35–37]. It considers only cell surface temperature. The coolant flow is assumed laminar with known constant inlet temperature and speed. Each cell in the string is thermally coupled with all cells in the upstream direction.

- The thermal model considers only joule heating of each cell. The entropic losses [85] (thermo-chemical heating/cooling due to exothermic/endothermic chemical reactions) are neglected in this study as typically done for xEV applications [23, 35–37, 86].

- The OCV of all cells is assumed constant for a battery operation in a typical SOC window of 20% to 90%. This approximation is somewhat justified particulary for $LiFePO_4$/graphite (LFP) cells, which are well known to have quite flat OCV curve. Their OCV varies only by $0.25mV$ per 1% SOC variation in $[0.4, 0.65]$ and varies in total by almost $90mV$ only with full SOC swing over $[0.2, 0.9]$, see [72].

- The cell series resistance has negligible SOC dependence over normal operating temperature range $[25, 50]$°C as shown in [35].

- The cell parameters are, in general, also nonlinear functions of cell temperature. In this thesis, they are assumed constant for control design, but control robustness under parametric variations and uncertainty is shown.

3.1.1 Electrical Model

Under the above assumptions, the electrical model of any Cell_i in a battery pack consisting of n cells is given by

$$\dot{\xi}_i(t) = -b_{ei}\, i_{Bi}(t), \tag{3.1}$$

$$V_{Bi}(t) = v_{oci} - R_{ei}\, i_{Bi}(t), \tag{3.2}$$

where $\xi_i \in [0,1]$ is the normalized SOC, i_{Bi} is the current, V_{Bi} is the terminal voltage, v_{oci} is the open-circuit voltage (OCV), $b_{ei} = \frac{1}{3600 C_{ei}}$, C_{ei} is the coulomb capacity, $V_{B\ell i} = R_{ei} i_{Bi}$ is the ohmic polarization, and R_{ei} is the resistance of Cell_i. Note that $i_{Bi} > 0$ implies the discharging of Cell_i.

3.1.2 Thermal Model

The cell temperature dynamics in an air-cooled battery pack depends on many factors like coolant properties, cell material properties, cell placement and pack configuration. The forced-convection cooled battery pack has been modeled in [23, 35–37] using a lumped-capacitance thermal modeling and flow network modeling approach. The lumped thermal model approximates the whole heat generation in a cell by a lumped thermal source and assumes uniform temperature distribution in a cell. The flow network modeling is a general methodology that represents the flow system as a network of components and fluid flow paths to approximate the temperature distribution inside it [87]. In this thesis, we adapt the modeling approach of [23] for deriving control-oriented thermal model.

Let us consider a series string of n cells as shown in Figure 3.1. The coolant flow inside the battery pack can be modeled using the network of fluid temperature nodes where each Cell_i exchanges heat with the coolant fluid, in the upstream and the downstream direction, through two fluid temperature nodes '$i-1$' and 'i' respectively, whereas each temperature node is shared between two consecutive cells as shown in Figure 3.1. A sufficient amount of free space is present between the cells to allow streams of laminar flow of the coolant (air).

In this thesis, the thermal balancing problem is studied under both uni-directional and reciprocating coolant flows (UF and RF). The model is first

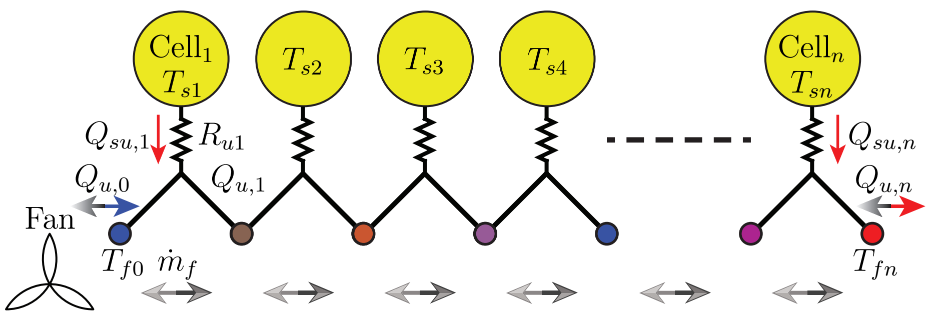

Figure 3.1: Battery thermal network diagram where $Q_{su,i}$ and $Q_{u,i}$ are heat transfer rates from Cell_i and at coolant fluid node 'i' respectively. Heat balance for left-to-right coolant flow is given by $Q_{u,i} = Q_{u,i-1} + Q_{su,i}$

Table 3.1: Definition of cell and coolant parameters

Parameters	**Expression**	**Units**
OCV of Cell$_i$	v_{oci}	V
Electrical Resistance of Cell$_i$	R_{ei}	Ω
Charge Capacity of Cell$_i$	C_{ei}	Ah
Mass of Cell$_i$	m_i	kg
Heat Capacity of Cell$_i$	$C_{si} = \rho_{si} c_{psi} V_{si}$	JK^{-1}
Thermal Resistance of Cell$_i$	R_{ui}	KW^{-1}
Air Density	ρ_f	$kg\, m^{-3}$
Air Specific Heat Capacity	c_{pf}	$JK^{-1}kg^{-1}$
Air Volumetric Flow Rate	$\dot{V}_f$	$m^3 s^{-1}$
Air Thermal Conductance	$c_f = \rho_f c_{pf} \dot{V}_f$	WK^{-1}
Temperature Coefficients	$a_{si} = \dfrac{1}{C_{si} R_{ui}}$	s^{-1}
Thermal Coupling Coefficients	$\alpha_i = R_{ui} c_f$	Unitless
Thermal Coupling Coefficients	$\beta_i = -1 + \alpha_i$	Unitless
Electrical Coefficient	$b_{ei} = \dfrac{1}{C_{si}}$	$(Ah)^{-1}$
Thermal Coefficient	$b_{ti} = \dfrac{R_{ei}}{C_{ei}}$	$J^{-1} K \Omega$

derived separately for the coolant flow in each direction and the two models are then combined to create the model for RF. The case of *forward coolant flow* (i.e., from Cell$_{i-1}$ to Cell$_i$) is designated as UF for ease of reference. For this case, the temperature dynamics of Cell$_i$ is given by [23]

$$\dot{T}_{si}(t) = -a_{si} T_{si}(t) + b_{ti} i_{Bi}^2(t) + a_{si} T_{fi-1}, \tag{3.3}$$

where T_{si} is the surface temperature and T_{fi-1} is the *local ambient temperature* of Cell$_i$ (i.e. temperature of upstream fluid node '$i-1$' of Cell$_i$, see Figure 3.1). The coefficients are given by $a_{si} = \dfrac{1}{C_{si} R_{ui}}$ and $b_{ti} = \dfrac{R_{ei}}{C_{si}}$, where C_{si} is the heat capacity (amount of heat energy required to raise the temperature of Cell$_i$ by 1 Kelvin) and R_{ui} is the convective thermal resistance of Cell$_i$ defined in Table 3.1. The value of these coefficients depend on the geometry and construction of the cell. The value of R_{ui} also depends on the coolant properties (like thermal conductivity) and on the Nusselt number, which, in turn, depends on the Reynolds (function of kinematic viscosity and flow speed of the coolant and cell diameter) and Prandtl numbers [88].

Equation (3.3) is not that interesting for control design because it explicitly depends on fluid temperature T_{fi-1}, which is not directly known. We can represent T_{fi-1} as a function of the upstream cell temperatures and the inlet fluid temperature T_{f0} as follows. According to [23], the temperatures of the fluid nodes '$i-1$' and 'i' are related by

$$T_{fi} = \frac{(T_{si} + \beta_i\, T_{fi-1})}{\alpha_i}, \tag{3.4}$$

where $\alpha_i = R_{ui} c_f$ and $\beta_i = -1 + \alpha_i$ with c_f as thermal conductance of the coolant fluid as defined in Table 3.1. Given that T_{f0} is a known quantity, then by forward recursion of equation (3.4), any T_{fi} can be expressed as a function of the inlet fluid temperature T_{f0} and the temperatures T_{s1} to T_{si} of the battery cells, such as

$$\begin{aligned}
T_{f1} &= \left(\frac{1}{\alpha_1}\right) T_{s1} + \left(\frac{\beta_1}{\alpha_1}\right) T_{f0},\\
T_{f2} &= \left(\frac{\beta_2}{\alpha_1\,\alpha_2}\right) T_{s1} + \left(\frac{1}{\alpha_2}\right) T_{s2} + \left(\frac{\beta_1\,\beta_2}{\alpha_1\,\alpha_2}\right) T_{f0},\\
T_{f3} &= \left(\frac{\beta_2\,\beta_3}{\alpha_1\,\alpha_2\,\alpha_3}\right) T_{s1} + \left(\frac{\beta_3}{\alpha_2\,\alpha_3}\right) T_{s2} + \left(\frac{1}{\alpha_3}\right) T_{s3} + \left(\frac{\beta_1\,\beta_2\,\beta_3}{\alpha_1\,\alpha_2\,\alpha_3}\right) T_{f0},
\end{aligned}$$

and so on. Therefore, the general equation for any T_{fi} is written as follows:

$$T_{fi} = a^{(1)}_{fi1}\, T_{s1} + a^{(1)}_{fi2}\, T_{s2} + \cdots + a^{(1)}_{fii}\, T_{si} + w^{(1)}_{fi}\, T_{f0}, \tag{3.5}$$

where

$$a^{(1)}_{fij} = \begin{cases} \dfrac{\prod_{k=(j+1)}^{i} \beta_k}{\prod_{k=j}^{i} \alpha_k}, & i > j,\\ \dfrac{1}{\alpha_i}, & i = j \geq 1,\\ 0, & i < j, \end{cases} \tag{3.6a}$$

$$w^{(1)}_{fi} = \frac{\prod_{k=1}^{i} \beta_k}{\prod_{k=1}^{i} \alpha_k} = 1 - \sum_{j=1}^{i} a^{(1)}_{fij}, \quad i \geq 1. \tag{3.6b}$$

Using equation (3.5) in (3.3), the thermal dynamics of Cell$_i$ for forward coolant flow can be re-written as follows:

$$\dot{T}_{si}(t) = a^{(1)}_{ti1}\, T_{s1}(t) + \cdots + a^{(1)}_{tin}\, T_{sn}(t) + b_{ti}\, i^2_{Bi}(t) + w^{(1)}_{ti}\, T_{f0}, \tag{3.7}$$

where the coefficients a_{tij} and w_{ti} are thermal circuit parameters given by

$$a^{(1)}_{tij} = \begin{cases} a^{(1)}_{f(i-1)j} \cdot a_{si} = \left(\dfrac{\prod_{k=(j+1)}^{(i-1)} \beta_k}{\prod_{k=j}^{(i-1)} \alpha_k}\right) a_{si}, & i > j,\\ -\, a_{si}, & i = j \geq 1,\\ 0, & i < j, \end{cases} \tag{3.8a}$$

$$w^{(1)}_{ti} = w^{(1)}_{f(i-1)} \cdot a_{si} = \left(\frac{\prod_{k=1}^{(i-1)} \beta_k}{\prod_{k=1}^{(i-1)} \alpha_k}\right) a_{si} = -\sum_{j=1}^{i} a^{(1)}_{tij}, \quad i \geq 1. \tag{3.8b}$$

The coefficient a_{tij} describes unidirectional thermal coupling from upstream Cell$_j$ to downstream Cell$_i$ due to convective heat transfer, whereas the coefficient w_{ti} describes the influence of T_{f0} on Cell$_i$.

Analogous to the forward coolant flow case, the thermal dynamics of Cell$_i$ is derived for *reverse coolant flow* (i.e., from Cell$_i$ to Cell$_{i-1}$). The result is given below

$$\dot{T}_{si}(t) = a_{ti1}^{(2)}\,T_{s1}(t) + \cdots + a_{tin}^{(2)}\,T_{sn}(t) + b_{ti}\,i_{Bi}^2(t) + w_{ti}^{(2)}\,T_{fn}, \tag{3.9}$$

where T_{fn} is the temperature of the inlet fluid entering battery pack from the Cell$_n$ side and thermal coupling coefficients are given by

$$a_{tij}^{(2)} = a_{tji}^{(1)}, \quad w_{ti}^{(2)} = w_{t(n-i+1)}^{(1)}. \tag{3.10}$$

The thermal model of Cell$_i$ under RF can now be easily constructed by combining (3.7) and (3.9). Note that from now onwards, we drop the superscripts on coefficients a_{tij} and w_{ti} to reduce notational clutter.

3.1.3 Electro-thermal Model

The complete electro-thermal model is summarized below

$$\dot{\xi}_i(t) = -b_{ei}\,i_{Bi}(t), \tag{3.11a}$$
$$\dot{T}_{si}(t) = a_{ti1}\,T_{s1}(t) + \cdots + a_{tin}\,T_{sn}(t) + b_{ti}\,i_{Bi}^2(t) + w_{ti}\,T_{f\text{in}}, \tag{3.11b}$$
$$V_{Bi}(t) = v_{oci} - R_{ei}\,i_{Bi}(t), \tag{3.11c}$$

where $T_{f\text{in}} \in \{T_{f0}, T_{fn}\}$ is the inlet coolant temperature and the values of thermal coefficients a_{tij} and w_{ti} are given by (3.8a) and (3.8b), or by (3.10) depending on the coolant flow direction given at any time instant. This cell model is adapted in the next chapter to derive complete state-space model of the modular battery under the switching action of dc/dc converters.

3.2 Cell-level Control: Preliminary Discussion

The load sharing concept is proposed in the previous chapter to achieve thermal and SOC balancing simultaneously. The realization of this concept requires cell-level battery control. This section adds some preliminary discussion in this regard as a preparation for a formal study in the following chapters.

3.2.1 Control Mechanism

The load sharing concept can be realized using $i_{Bi}(t)$ as an independent manipulating variable for each Cell$_i$. However, to achieve this, we need some external control circuit/mechanism. In case of modular battery, a dc/dc converter inside each module provides this mechanism, which enables the manipulation of i_{Bi} as follows

$$i_{Bi}(t) = u_i(t) i_L(t), \tag{3.12}$$

where $u_i(t)$ is a control knob (or duty cycle) of Cell$_i$ and $i_L(t)$ is the load current. Note that the range of u_i depends on the dc/dc converter topology. Since $i_L(t)$ is a given exogenous quantity at each time instant, the duty cycle $u_i(t)$ is used to adjust the cell current such that cells remain balanced in terms of SOC and temperature.

The battery pack develops thermal and SOC imbalance among its cells due to variations in cell resistances ($R_{ei} \neq R_{ej},\ \forall i, j$) and cell capacities ($C_{ei} \neq C_{ej},\ \forall i, j$) respectively. Therefore, assuming all the cell parameters are known, one straightforward way to choose u_i is based on the level of health (cell resistance and capacity) imbalance i.e. health of Cell$_i$ relative to the average health of battery cells. For example, for SOC balancing, the duty may simply be chosen as

$$u_i(t) = \begin{cases} \dfrac{C_{ed,i}(t)}{\bar{C}_{ed}(t)}, & \text{discharging} \\ \dfrac{C_{ec,i}(t)}{\bar{C}_{ec}(t)}, & \text{charging} \end{cases} \tag{3.13}$$

where $C_{ed,i}$ and $C_{ec,i}$ are dischargeable and chargeable capacities of Cell$_i$ as defined in (2.6) and $\bar{C}_{ed} = \text{mean}(C_{ed})$ and $\bar{C}_{ec} = \text{mean}(C_{ec})$ are mean of dischargeable and chargeable capacity vectors defined in (2.7) and (2.8) respectively. Similarly, for thermal balancing, the cell duty can be chosen as (assuming ambient-temperature imbalance is zero i.e. $T_{fi} = T_{fj}$)

$$u_i(t) = \frac{\bar{R}_e}{R_{ei}}, \quad \text{charging/discharging} \tag{3.14}$$

where R_{ei} is the resistance of Cell$_i$ and $\bar{R}_e = \text{mean}(R_e)$ is the mean resistance of cells where R_e is defined in (2.4). Since it is quite possible for any Cell$_i$ in the string to have $C_{ed,i} > \bar{C}_{ed}$ and $R_{ei} > \bar{R}_e$, relations (3.13) and (3.14) imply that Cell$_i$ may have conflicting duty requirements for SOC and thermal balancing. This shows that thermal and SOC balancing are two tightly coupled and somewhat conflicting objectives. Therefore, we need a more sophisticated way of choosing cell duties such that we get desired trade-off between two objectives depending on loading conditions. In other words, we want to have

$$u_i(t) = \kappa\left(\xi(t), T_s(t), i_L(t), v_{Ld}(t)\right), \tag{3.15}$$

where $\kappa(\cdot)$ is a control function/policy that is devised in this thesis. Here ξ and T_s are vectors of SOCs and temperatures of all cells, i_L is the load current, and v_{Ld} is the demanded battery load voltage at each time instant. It is pertinent to mention here that regardless of the control policy, it is infeasible to control SOC and temperature completely independent of each other because the cell current, which is the only manipulating variable, directly affects both states at each time instant. For example, during discharging, $i_{Bi}(t) > i_{Bj}(t)$ implies $i^2_{Bi}(t) > i^2_{Bj}(t)$ that implies $\dot{\xi}_i > \dot{\xi}_j$ and $\dot{T}_{si} > \dot{T}_{sj}$, which may not be desirable for balancing.

3.2.2 Feasibility and Requirements

To motivate the feasibility of thermal and SOC balancing, let us consider an alternative notion of *temperature and SOC control in average sense.* With this notion, we do not aim at exact equalization of SOC and temperature all the time. Instead, after decay of initial imbalance, the perfect equalization of only SOC is desired at the boundaries (start and end) of a charge/discharge phase. However, inside the boundaries, the only objective is to keep temperature and SOC deviations within certain reasonable limits, providing SOC and temperature *deviations allowance* during run time. In addition, we also know that cells always generate heat whether we charge them (increasing the SOC) or discharge them (decreasing the SOC). We can exploit this fact to increase cell temperature without affecting its SOC. This slight decoupling is favorable for simultaneous thermal and SOC balancing. Moreover, temperature rises quickly only during intensive load demand (aggressive acceleration/braking). During these short high power pulses, the controller may prioritize thermal balancing to keep temperature deviation small without significantly deteriorating SOC balancing performance.

To elaborate above concepts, let us define average and rms currents

$$I_{Bai} = \frac{1}{\Delta t}\int_{t_1}^{t_2} i_{Bi}(\tau)\mathrm{d}\tau, \quad I_{Bri} = \sqrt{\frac{1}{\Delta t}\int_{t_1}^{t_2} i^2_{Bi}(\tau)\mathrm{d}\tau}, \tag{3.16}$$

of each Cell$_i$ over a certain period $\Delta t = t_2 - t_1$ of a drive cycle of length T_d. Now suppose that the segment Δt of the drive cycle contains series of high and low current phases. Since temperature dynamics is quadratic and SOC is linear in input current $i_{Bi}(t)$, it may be possible to somewhat independently adjust I_{Bai} and I_{Bri} for each Cell$_i$ by appropriately scheduling the load (current) of each cell during Δt. This may help to achieve $I_{Bai} > I_{Baj}$ and $I_{Bri}^2 < I_{Brj}^2$ or $I_{Bai} < I_{Baj}$ and $I_{Bri}^2 > I_{Brj}^2$ for any Cell$_i$ and Cell$_j$, enabling somewhat independent control of their average temperature and SOC during Δt. This gives an opportunity to achieve simultaneous *thermal and SOC balancing in average sense*. For example, let us consider a battery pack consisting of two cells having capacity, dischargeable capacity, and resistance variations ($C_{e1} \neq C_{e2}$, $C_{ed,1}(0) \neq C_{ed,2}(0)$, and $R_{e1} \neq R_{e2}$). We have four possible cases in this example:

- Case-1: $C_{ed,1}(0) < C_{ed,2}(0)$ and $R_{e1} < R_{e2}$,
- Case-2: $C_{ed,1}(0) > C_{ed,2}(0)$ and $R_{e1} < R_{e2}$,
- Case-3: $C_{ed,1}(0) < C_{ed,2}(0)$ and $R_{e1} > R_{e2}$,
- Case-4: $C_{ed,1}(0) > C_{ed,2}(0)$ and $R_{e1} > R_{e2}$.

The objective is to minimize thermal and SOC deviations while meeting at the same time the total power demand of a load. Since two cells have nonuniform characteristics, the optimal policy is to also use them non-uniformly according to their temperature and SOC. Note that Case-2, during discharging, can be easily handled by using Cell$_1$ more ($I_{Ba1} > I_{Ba2}$ and $I_{Br1} > I_{Br2}$) and similarly Case-3 by using Cell$_1$ less compared to Cell$_2$. However, for cases 1 and 4, we have conflicting situation during discharging. For example, in Case-1, SOC balancing requires Cell$_1$ to be used less than Cell$_2$, but thermal balancing requires Cell$_1$ to be used more than Cell$_2$. These cases require a more sophisticated usage policy. For instance, in Case-1, thermal balancing can potentially be achieved by using (higher resistance) Cell$_2$ less than Cell$_1$ during *short high current phases* (either charging or discharging) of the drive cycle. This leads to relatively quick increase in temperature of Cell$_1$ compared to that of Cell$_2$ as losses are quadratic in current. The SOC balancing, on the other hand, is achieved simultaneously by using Cell$_2$ more than Cell$_1$ during *long low current phases*. In addition, the (lower resistance) Cell$_1$ should absorb most of the charging energy during short high regenerative braking phases and should deliver most of this energy during following high acceleration phases. This policy of cell usage may result in $I_{Ba2} > I_{Ba1}$ (for SOC balancing) and $I_{Br2} < I_{Br1}$ (for thermal balancing). Note that Case-4 can similarly be handled by using Cell$_1$ less during high current phases and more during low current intervals.

It should be noticed that a certain level of SOC and temperature deviation allowance is needed for flexibility. In addition, the *load variations* (i.e. a load consisting of long low-current and short high-current phases) are also desirable for the effectiveness of above rules. This kind of load profile is quite typical for xEVs due to natural variations (arise from variations in topography, traffic flow, and driver's behavior etc.) in their speed and acceleration. If future load current can be predicted, then the load for each cell can be scheduled using information about high and low current (including brake regeneration) phases in the drive cycle to keep thermal and SOC deviations within reasonable limits. In addition, we also need *sufficient cell redundancy* in the battery pack i.e. the maximum battery terminal voltage should be sufficiently greater than the maximum possible demanded load voltage, $v_{Ld}(t)$, at any time instant.

3.2.3 Cell Balancing as Optimization Problem

The above discussion hinges on the basic idea of planning the load distribution among cells based on present and future load profile. For this planning, we need an intelligent control policy that uses *accessible predictive (future) information* about each cell state and load to decide duty cycle of each cell at each sampling instant. We propose to formulate this problem as a *convex optimization* problem, which in words is stated below.

$$\begin{aligned}
&\textbf{minimize } \text{``SOC and temperature deviations among all cells''}\\
&\text{subject to}\\
&\begin{cases}
\text{Battery electro-thermal dynamic constraint,}\\
\text{Max } \textbf{SOC} \text{ deviations constraint,}\\
\text{Min/Max SOC constraint,}\\
\text{SOC terminal constraint,}\\
\text{Max } \textbf{Temperature} \text{ deviations constraint,}\\
\text{Max Temperature constraint,}\\
\text{Voltage tracking constraint,}\\
\text{Max Battery current constraint,}\\
\textbf{Duty cycle} \text{ zone constraint,}\\
\textbf{Given: } \text{Demanded load voltage and current.}
\end{cases}
\end{aligned} \tag{3.17}$$

for all time instances over a prediction horizon N with optimization variables SOC ($\xi_i(t)$), temperature ($T_{si}(t)$), and duty cycle $u_i(t)$ of each Cell$_i$. The variable $u_i(t)$ acts as control knob of Cell$_i$ and is provided by the balancing hardware. The output of this optimization problem over whole drive cycle of discrete time length N_d is the control sequence $\{u(t)\}_{t=1}^{N_d}$ where each control $u(t) \in \mathbb{R}^n$ consists of optimal duty cycles $u_i(t)$ for each Cell$_i$. Note that, for formulation of the above problem, we need to secure convexity of constraints and the model of the modular battery under the switching action of dc/dc converters. This is carefully done in the next chapter.

3.3 Summary and Conclusions

In this chapter, we have derived a control-oriented electro-thermal model of a cell. This model is used in the next chapter as a basic building block for complete state-space model of the modular battery. In addition, we have also added some preliminary discussion on load sharing problem based on cell-level control for simultaneous thermal and SOC balancing. The feasibility of achieving these two tightly coupled objectives is informally discussed. It is contended, using simple arguments, that this problem can be solved by

- exploiting the regeneration phases and variations in the load profile,
- exploiting the SOC and temperature deviation allowance,
- exploiting the cell redundancy in the battery pack,

to get optimal duty schedule of each cell in different load ranges to keep temperature and SOC deviations as small as possible. However, we may need a predictive control framework, using state and load predictions over a reasonable horizon, to generate an optimal policy for load distribution. We may also have to consider various kinds of dc/dc converter topologies inside the modular battery to get sufficient control range (controllability).

Chapter 4

Modular Battery: Modeling

In this chapter, we formally present the architecture and the state-space model of the modular battery. In particular, two dc/dc converter topologies (two- and four-quadrant operation) of the battery module are presented in the context of unipolar and bipolar control (UPC and BPC) modes. The model is derived carefully based on an average modeling approach to secure convexity under both UPC and BPC operation. This is made possible by employing a certain assumption during averaging of battery variables under the switching action of dc/dc converters. These aspects are discussed at length in this chapter.

4.1 Introduction

The modular battery, shown in Figure 4.1, consists of n series-connected PUs, each containing a dc/dc converter with ideal switches and an isolated battery module designated here as Cell_i. It supplies terminal power $P_L(t) = i_L(t)v_L(t)$ to a variable load with known power demand $P_{Ld}(t) = i_L(t)v_{Ld}(t)$, where i_L is the load current, v_{Ld} is the demanded load voltage, and

$$v_L(t) = \sum_{i=1}^{n} v_{Li}(t) \in [0, v_{L,\max}], \tag{4.1}$$

is the terminal voltage of the modular battery. Here $v_{L,\max}$ is the maximum voltage capacity of the modular battery, $v_{Li}(t) \in \{-V_{Bi}, 0, +V_{Bi}\}$ is the terminal voltage of PU_i with V_{Bi} as the terminal voltage of Cell_i.

4.1.1 Module Control Modes: UPC and BPC

The power flow from each PU_i is controlled using two control variables $u_i^+ \in [0, 1]$ and $u_i^- \in [0, 1]$ (so-called *positive and negative duty cycles*, see

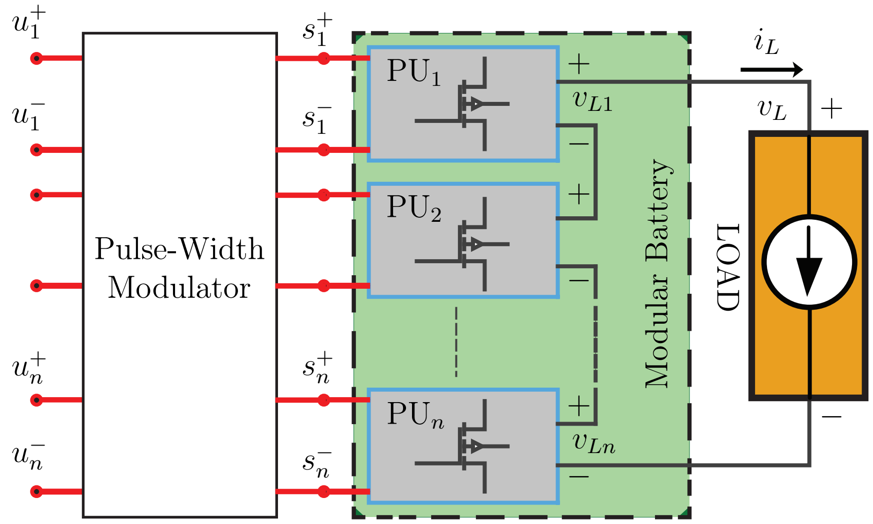

(a) Modular Battery with n modules, each denoted by PU$_i$.

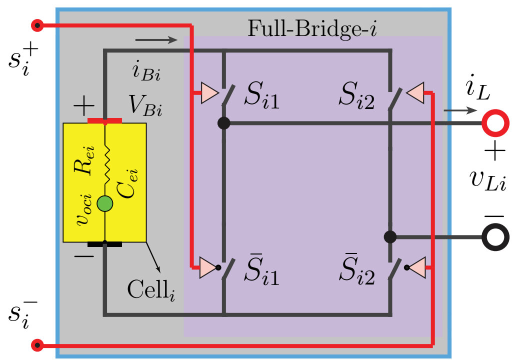

(b) FB-based PU$_i$.

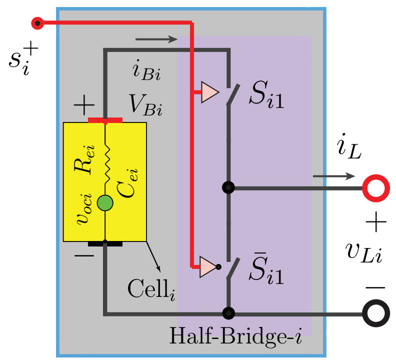

(c) HB-based PU$_i$.

Figure 4.1: Modular battery (inside green box) along with two alternative module topologies shown in figures 4.1(b) and 4.1(c).

section 4.2 for details). These control variables are fed into a pulse width modulator, which generates unipolar switching functions $s_i^+ \in \{0,1\}$ and $s_i^- \in \{0,1\}$, with switching period T_{sw}, to control transistors inside each PU_i as shown in Figure 4.1. From voltage control viewpoint, the variables u_i^+ and u_i^- can be viewed as control knobs to generate $v_{Li} \geq 0$ and $v_{Li} \leq 0$ respectively. Therefore, the positive control vector $u^+ = \begin{bmatrix} u_1^+ & \cdots & u_n^+ \end{bmatrix}^{\mathrm{T}} \in \mathcal{U}^+ \subseteq \mathbb{R}_+^n$ generates positive v_L with each $v_{Li} \geq 0$ and the negative control vector $u^- = \begin{bmatrix} u_1^- & \cdots & u_n^- \end{bmatrix}^{\mathrm{T}} \in \mathcal{U}^- \subseteq \mathbb{R}_+^n$ generates negative v_L with each $v_{Li} \leq 0$. The full control is given by $u(t) = \begin{bmatrix} (u^+(t))^{\mathrm{T}} & (u^-(t))^{\mathrm{T}} \end{bmatrix}^{\mathrm{T}} \in \mathcal{U} \subseteq \mathbb{R}_+^{2n}$, which gives the possibility of two control modes, defined below, of the modular battery. We also define three terms— *positive cell actuation*, *negative cell actuation*, and *bipolar cell actuation*— which are used frequently in this thesis. We have positive actuation of Cell_i if u_i^+ is active ($u_i^+ \neq 0$), negative actuation of Cell_i if u_i^- is active, and bipolar actuation if both u_i^+ and u_i^- are simultaneously active subject to some assumptions (discussed below) about subsequent PWM generation method. In the following, we broadly define two types of battery control modes based on how u^+ and u^- are employed.

Unipolar Control Mode

In *unipolar control* (UPC) mode, depending on the sign of demanded load voltage v_{Ld}, either u^+ is active (positive actuation of all cells) or u^- is active (negative actuation of all cells). Since v_{Ld} is always positive for xEVs, only positive actuation is considered under UPC here. This simpler mode does not allow polarity inversion of any cell in the string (i.e. $v_{Li}(t)v_{Lj}(t) \geq 0$) during any switching cycle. This implies that at any time, either all cells are charging or all are discharging depending on the sign of i_L.

Bipolar Control Mode

In the *bipolar control* (BPC) mode, both u^+ and u^- may be simultaneously active (i.e. bipolar cell actuation). The BPC mode allows polarity inversion (i.e. $v_{Li}(t)v_{Lj}(t) \leq 0$) of some cells in the string during each switching cycle. This simply implies that it is possible to charge some cells while discharging others at any time.

Note that the BPC mode, with two control variables per cell, improves the controllability properties of the modular battery system, which may make it easier to achieve the control objectives. However, it may require larger surplus voltage in the modular battery compared to that for UPC and may also generate extra battery losses due to negative cell actuation. In addition, the BPC mode also poses some modeling challenges (i.e. nonconvexity may arise, see Remark 4.2), which need a special consideration regarding pulse placement method for PWM signal generation, see condition (4.2) below.

4.1.2 Module Topology

There are various dc/dc converter topologies that can be used inside PUs. Two particular architectures of PU_i considered in this study are shown in Figures 4.1(b) and 4.1(c).

Full-Bridge Based $\mathbf{PU}_i$

The PU_i based on full-bridge (FB) converter is shown in Figure 4.1(b). The FB is a switch-mode dc-dc converter, which consists of four bidirectional switches (MOSFETs with anti-parallel body diodes). These switches are controlled using two unipolar switching functions $s_i^+(t)$ and $s_i^-(t)$ (one for each half-bridge). These bidirectional switches allow current flow in both directions, which makes it possible to voluntarily charge as well as discharge the battery module. We can generate three different discrete levels of output voltage $v_{Li}(t) \in \{-V_{Bi}, 0, +V_{Bi}\}$ from each PU_i while operating it as a stand-alone device. However, assuming PWM operation of switches and low-pass nature of load, we can generate average voltage output $v_{Lai}(t) \in [-V_{Bi}, +V_{Bi}]$ corresponding to duty cycles u_i^+ and u_i^-. Therefore, each PU_i can be operated in all four quadrants of the i_L–v_{Li} plane, which enables *active control* of bidirectional power flow from each module. Note that FB-based PU_i can be operated using both UPC and BPC modes.

Half-Bridge Based $\mathbf{PU}_i$

The second variant of PU_i (designated as HB-based PU_i) shown in Figure 4.1(c) is based on half-bridge (HB) converter. It consists of only two bidirectional switches, which are operated using only one unipolar switching function s_i^+. It also allows bidirectional current flow, but only positive output voltage can be generated i.e. $v_{Lai}(t) \in [0, +V_{Bi}]$ corresponding to duty cycle u_i^+. Therefore, each PU_i can be operated in only 1st and 2nd quadrants of the i_L–v_{Li} plane. The control in the 2nd quadrant is only possible during regeneration or external charging phases i.e. when load power $P_{Ld} < 0$. Note that only UPC mode is possible for HB-based PU_i.

Equivalence of Two Topologies

If FB-based PU_i is operated using UPC ($s_i^-(t) = 0$) then switch $\bar{S}_{i2}$ is turned ON permanently. This implies that the switch $\bar{S}_{i2}$ can be replaced with a short-circuit, which reduces FB-based PU_i to HB-based PU_i. Therefore, both topologies are equivalent under UPC.

4.1.3 Module Switched Behavior

There are three (two) different operational modes/switching states of each FB-based PU_i (HB-based PU_i). In Mode–1 $v_{Li} > 0$, in Mode–2 $v_{Li} < 0$ and in Mode–3 $v_{Li} = 0$. These modes can be modeled using two unipolar switching functions s_i^+ and s_i^-. For modeling convenience, this study assumes s_i^+ and s_i^- to be orthogonal (non-overlapping) i.e.,

$$\int_{t-T_{\mathrm{sw}}}^{t} s_i^+(\tau)s_i^-(\tau)\mathrm{d}\tau = 0, \tag{4.2}$$

where T_{sw} is the switching period of s_i^+ and s_i^-. This *orthogonality condition* simply implies that s_i^+ and s_i^- cannot be high simultaneously. Now using this condition, a single three-level bipolar PWM function $s_i(t)$ modeling three aforementioned modes is given by

$$s_i(t) = s_i^+(t) - s_i^-(t) = \begin{cases} 1, & \text{Mode–1} \\ -1, & \text{Mode–2} \\ 0, & \text{Mode–3.} \end{cases} \tag{4.3}$$

Note that according to the condition (4.2), $s_i = 0$ is generated using only $s_i^+ = s_i^- = 0$ i.e., by turning ON the lower transistors ($\bar{S}_{i1}$ and $\bar{S}_{i2}$) and not the upper ones. Also note that only Modes 1 and 3 are available for HB-based PU_i.

The signals $(i_{Bi}, V_{Bi}, i_L, v_{Li})$ on two ports of each PU_i are linearly related through $s_i(t)$ as follows. The switched current through each Cell_i for a given load current i_L is given by

$$i_{Bi}(t) = i_L(t)s_i(t). \tag{4.4}$$

The switched terminal voltage of each PU_i is given by

$$v_{Li}(t) = \begin{cases} d_{vi}^+(t), & s_i(t) = 1 \\ 0, & s_i(t) = 0 \\ -\, d_{vi}^-(t), & s_i(t) = -1 \end{cases} \tag{4.5}$$

where

$$d_{vi}^+(t) = v_{oci} - i_L(t)R_{ei}, \quad d_{vi}^-(t) = v_{oci} + i_L(t)R_{ei}, \tag{4.6}$$

are cell terminal voltages, $V_{Bi}(t)$, during discharging and charging respectively for $i_L(t) > 0$ where v_{oci} and R_{ei} denote cell OCV and resistance. Based on orthogonality condition (4.2), the piecewise linear function (4.5) is equivalently represented by the following linear relation

$$v_{Li}(t) = d_{vi}^{+}(t)s_i^{+}(t) - d_{vi}^{-}(t)s_i^{-}(t). \tag{4.7}$$

Now the variables d_{vi}^{+} and d_{vi}^{-} can also be interpreted as terminal voltages of Cell$_i$ during its positive and negative actuation respectively. The terminal voltage and power of the modular battery are given by $v_L = \sum_{i=1}^{n} v_{Li}$ and $P_L = \sum_{i=1}^{n} P_{Li}$, where $P_{Li} = v_{Li}i_L$ is the terminal power of each PU$_i$.

4.2 Module Averaged Behavior

We are interested in controlling the average behavior of the switched modular battery during each switching period T_{sw} of $s_i(t)$ under both UPC and BPC modes. For this purpose, *averaging of cell variables* is done in this section in a setting, which is applicable to both UPC and BPC. We employ only two assumptions: 1) the orthogonality condition (4.2) is satisfied and 2) $i_L(t)$ is constant during each cycle of a high-frequency PWM $s_i(t)$.

Positive and Negative Controls (Duty Cycles)

Assuming the orthogonality condition (4.2) is satisfied, the positive and negative controls (or duty cycles) of Cell$_i$ during switching period $[t - T_{\text{sw}}, t]$ are defined by

$$u_i^{+}(t) := \frac{1}{T_{\text{sw}}} \int_{t-T_{\text{sw}}}^{t} s_i^{+}(\tau)\mathrm{d}\tau = \frac{T_i^{+}(t)}{T_{\text{sw}}}, \tag{4.8}$$

$$u_i^{-}(t) := \frac{1}{T_{\text{sw}}} \int_{t-T_{\text{sw}}}^{t} s_i^{-}(\tau)\mathrm{d}\tau = \frac{T_i^{-}(t)}{T_{\text{sw}}}, \tag{4.9}$$

where $T_i^{+}(t)$ and $T_i^{-}(t)$ are ON time intervals of $s_i^{+}(t)$ and $s_i^{-}(t)$ respectively during switching period $[t - T_{\text{sw}}, t]$. Note that the duty cycles can only be chosen such that $u_i^{+} \in [0,1], u_i^{-} \in [0,1]$, and $u_i^{+} + u_i^{-} \in [0,1]$. These constraints can be represented as a polytope

$$\mathcal{U}_i = \{(u_i^{+}, u_i^{-}) | H_{ui}u_i \leq h_{ui}\}, \tag{4.10}$$

for suitably defined constraint matrix H_{ui} and vector h_{ui}, where $u_i = \begin{bmatrix} u_i^{+}(t) & u_i^{-}(t) \end{bmatrix}^{\mathrm{T}}$. The set $\mathcal{U}_i$ is shown in Fig. 4.2(a) for UPC (using $u_i^{-} = 0$ in (4.10)) and in Fig. 4.2(d) for BPC.

SOC and Temperature Controls

Using u_i^+ and u_i^-, we define two new control variables

$$u_{gi}(t) = u_i^+(t) - u_i^-(t), \tag{4.11}$$
$$u_{\ell i}(t) = u_i^+(t) + u_i^-(t). \tag{4.12}$$

The variables u_{gi} and $u_{\ell i}$ respectively control average and rms currents in Cell_i during each switching period (see next subsection). Since the average and rms cell currents govern SOC and temperature respectively, u_{gi} and $u_{\ell i}$ are so-called SOC and temperature controls. The set of admissible SOC and temperature control actions can be represented by the following electro-thermal control polytope

$$\mathcal{U}_i^{g\ell} = \{(u_{gi}, u_{\ell i}) | H_{ug\ell,i} u_{g\ell,i} \leq h_{ug\ell,i}\}, \tag{4.13}$$

for suitably defined constraint matrix $H_{ug\ell,i}$ and vector $h_{ug\ell,i}$, where $u_{g\ell,i} = \begin{bmatrix} u_{gi}(t) & u_{\ell i}(t) \end{bmatrix}^{\mathrm{T}}$. The set $\mathcal{U}_i^{g\ell}$ is shown in Fig. 4.2(b) for UPC and in Fig. 4.2(e) for BPC.

Average and RMS Currents

Using definitions (4.3), (4.8), (4.9), and relation (4.4), we can compute average and rms cell currents during each switching period as follows. The average current of Cell_i is given by

$$\begin{aligned} i_{Bai}(t) &= \frac{1}{T_{\text{sw}}} \int_{t-T_{\text{sw}}}^{t} i_{Bi}(\tau) \mathrm{d}\tau \\ &= i_L(t) \left[u_i^+(t) - u_i^-(t)\right] = i_L(t) u_{gi}(t). \end{aligned} \tag{4.14}$$

Similarly, the rms current of Cell_i is defined by

$$i_{Bri}^2(t) = \frac{1}{T_{\text{sw}}} \int_{t-T_{\text{sw}}}^{t} i_{Bi}^2(\tau) \mathrm{d}\tau = \frac{i_L^2(t)}{T_{\text{sw}}} \int_{t-T_{\text{sw}}}^{t} {s_i}^2(\tau) \mathrm{d}\tau,$$

which, using (4.3) and orthogonality condition (4.2), is given by

$$i_{Bri}^2(t) = i_L^2(t) \left[u_i^+(t) + u_i^-(t)\right] = i_L^2(t) u_{\ell i}(t). \tag{4.15}$$

Now, defining $i_{Bar,i} = \begin{bmatrix} i_{Bai} & i_{Bri}^2 \end{bmatrix}^{\mathrm{T}}$, the set of admissible average and rms currents can be represented by a polytope

$$\mathcal{I}_i^{ar} = \{(i_{Bai}, i_{Bri}^2) | H_{iBar,i}(t) i_{Bar,i} \leq h_{iBar,i}\}, \tag{4.16}$$

for suitably defined $H_{iBar,i}$ and $h_{iBar,i}$. The set is shown in figures 4.2(c) and 4.2(f) for UPC and BPC respectively.

Remark 4.1 (UPC and BPC Comparison based on $\mathcal{I}_i^{ar}$)**.** *Note that there is a linear relationship (* one-to-one coupling*) between average and rms cell currents under constant load for UPC mode, see line segments representing set of feasible average and rms cell currents in Figure 4.2(c). For any constant load current, average and rms currents* (i_{Bai} *and* i^2_{Bri}) *of any Cell*$_i$ *can be chosen only along a certain line. To change rms value of cell current without affecting its average value requires change in magnitude of load current. Similarly, to change cell average current without affecting the rms requires reversal in direction of load current. Therefore, load current variation, both in magnitude and direction, is favorable for achieving simultaneous thermal and SOC balancing using UPC mode otherwise it may be a daunting task under constant high load current. For BPC mode, on the other hand, average and rms cell currents are loosely coupled under constant loads, see triangular polytopes representing set of feasible average and rms cell currents in Figure 4.2(f). This larger set gives a possibility of somewhat independent adjustment of* i_{Bai} *and* i_{Bri}*, which is favorable for simultaneous thermal and SOC balancing. Therefore, variation in magnitude and direction of load current is not strictly needed for BPC.*

From this simple reasoning, it can be readily seen that BPC would result in tighter balancing subject to negative cell actuation ($u_i^-(t) > 0$)*, which is feasible if the voltage demand* $v_{Ld}(t)$ *is sufficiently lower than the maximum voltage capacity* $v_{L,\max}(t)$ *(see equation* (4.26) *for definition) of the modular battery. This may require redundant modules in the battery pack.*

Average Voltage

Using (4.7), the average terminal voltage of PU$_i$ is given by

$$\begin{aligned} v_{Lai}(t) &= \frac{1}{T_{\text{sw}}}\int_{t-T_{\text{sw}}}^{t} v_{Li}(\tau)\mathrm{d}\tau \\ &= d_{vi}^+(t)u_i^+(t) - d_{vi}^-(t)u_i^-(t). \end{aligned} \tag{4.17}$$

The terminal voltage of the modular battery is thus given by

$$v_{La}(t) = \textstyle\sum_{i=1}^{n} v_{Lai}(t) = D_v^+(t)u^+(t) - D_v^-(t)u^-(t), \tag{4.18}$$

where

$$D_v^+(t) = \begin{bmatrix} d_{v1}^+(t) & \cdots & d_{vn}^+(t) \end{bmatrix}, \tag{4.19a}$$

$$D_v^-(t) = \begin{bmatrix} d_{v1}^-(t) & \cdots & d_{vn}^-(t) \end{bmatrix}, \tag{4.19b}$$

are vectors of terminal voltages of n cells during discharging and charging respectively for $i_L(t) > 0$.

Average Power

The total terminal power of modular battery is given by

$$P_{La}(t) = \sum_{i=1}^{n} P_{Lai}(t) = D_p^+(t)u^+(t) - D_p^-(t)u^-(t), \tag{4.20}$$

where $P_{Lai} = v_{Lai}i_L$ is the average terminal power of each Cell_i and $D_p^+ = i_L D_v^+$ and $D_p^- = i_L D_v^-$ are vectors of cell terminal powers during discharging and charging respectively for $i_L(t) > 0$.

Remark 4.2. *The use of two switching functions and orthogonality condition* (4.2) *has greatly simplified the derivation of averaged quantities (affine functions of duty cycles) for BPC compared to another approach [89], which results in non-convex terms like product of variables* $(u_i^+ \cdot u_i^-)$.

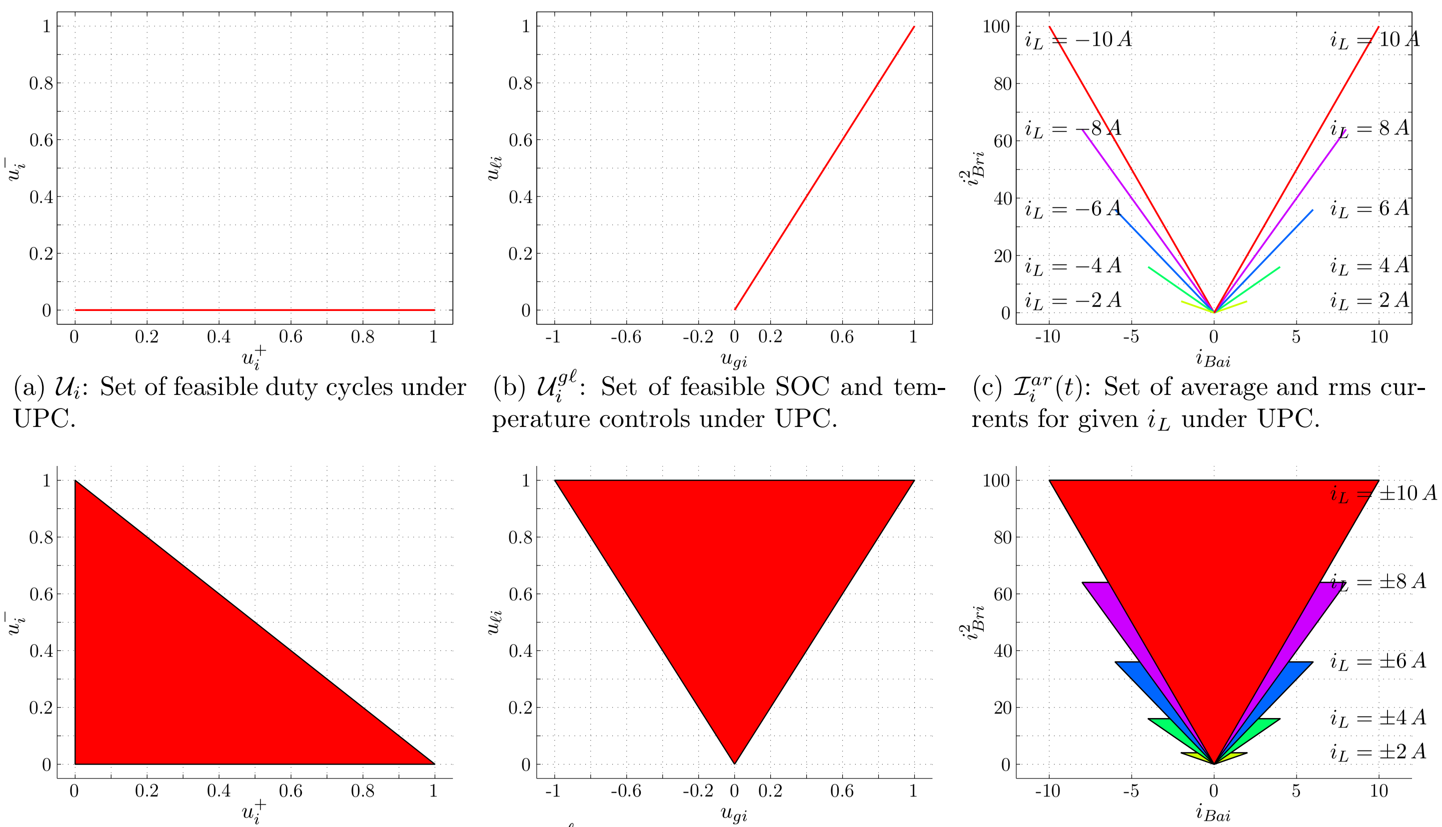

(a) $\mathcal{U}_i$: Set of feasible duty cycles under UPC.

(b) $\mathcal{U}_i^{g\ell}$: Set of feasible SOC and temperature controls under UPC.

(c) $\mathcal{I}_i^{ar}(t)$: Set of average and rms currents for given i_L under UPC.

(d) $\mathcal{U}_i$: Set of feasible duty cycles under BPC.

(e) $\mathcal{U}_i^{g\ell}$: Set of feasible SOC and temperature controls under BPC.

(f) $\mathcal{I}_i^{ar}(t)$: Set of average and rms currents for given i_L under BPC.

Figure 4.2: *Various constraint sets for $Cell_i$*: Unipolar (first row) and Bipolar (second row) control modes. Note that 4.2(c) and 4.2(f) can be obtained respectively by scaling 4.2(b) and 4.2(e) along the parabola given by i_L^2.

4.3 Averaged State-Space Model

The *averaged* state space electro-thermal model of an air-cooled modular battery consisting of n modules with ideal switches is presented on standard form here using averaged variables i_{Bai} and i^2_{Bri} [see (4.14) and (4.15)] as inputs for SOC dynamics (3.11a) and thermal dynamics (3.11b) respectively.

4.3.1 Model of One Module

The averaged electro-thermal model of each battery module PU_i of the modular battery for a given load current $i_L(t)$ is given by

$$\dot{\xi}_i(t) = -b_{ei} i_L(t)\Big(u_i^+(t) - u_i^-(t)\Big), \tag{4.21a}$$

$$\dot{T}_{si}(t) = \sum_{j=1}^{n} a_{tij} T_{sj}(t) + b_{ti} i_L^2(t)\Big(u_i^+(t) + u_i^-(t)\Big) + w_{ti} T_{f\mathrm{in}}, \tag{4.21b}$$

$$v_{Lai}(t) = d_{vi}^+(t) u_i^+(t) - d_{vi}^-(t) u_i^-(t), \tag{4.21c}$$

where temperature, T_{si}, and SOC, ξ_i, are states, $T_{f\mathrm{in}} \in \{T_{f0}, T_{fn}\}$ is the constant coolant temperature (measured disturbance) in one of the two inlets depending on the direction of the coolant flow, v_{Lai} is the terminal voltage of PU_i, u_i^+ and u_i^- are control variables defined in (4.8) and (4.9), and d_{vi}^+ and d_{vi}^- are defined in (4.6). Note that (4.21a) and (4.21b) are derived from (3.11a) and (3.11b) by substituting i_{Bi} and i^2_{Bi} with i_{Bai} and i^2_{Bri} respectively and then using (4.14) and (4.15). The parameters b_{ei} and b_{ti} are given in Table (3.1), whereas a_{tij} and w_{ti} are given by (3.8a) and (3.8b), or by (3.10) depending on the given coolant flow direction.

4.3.2 Complete Model

Using (4.21a)–(4.21c) as basic building block and treating $T_{f\mathrm{in}}$ as a dummy state, the averaged electro-thermal model of an n-cell modular battery is given by the following standard linear time-varying state-space system

$$\dot{x}(t) = Ax(t) + B(i_L(t))u(t), \tag{4.22a}$$

$$y(t) = Cx(t) + D(i_L(t))u(t). \tag{4.22b}$$

Here $x = \begin{bmatrix}\xi^{\mathrm{T}} & \vartheta^{\mathrm{T}}\end{bmatrix}^{\mathrm{T}} \in \mathbb{R}^{2n+1}$ is the full state vector, $\xi = \begin{bmatrix}\xi_1 & \cdots & \xi_n\end{bmatrix}^{\mathrm{T}} \in \mathbb{R}^n$ is a vector of SOCs, $\vartheta(t) = \begin{bmatrix}T_s^{\mathrm{T}}(t) & T_{f\mathrm{in}}\end{bmatrix}^{\mathrm{T}} \in \mathbb{R}^{n+1}$ is an augmented thermal state with $T_s(t) = \begin{bmatrix}T_{s1} & \cdots & T_{sn}\end{bmatrix}^{\mathrm{T}} \in \mathbb{R}^n$, $u(t) = \begin{bmatrix}(u^+)^{\mathrm{T}} & (u^-)^{\mathrm{T}}\end{bmatrix}^{\mathrm{T}} \in \mathbb{R}^{2n}$ is the control vector, $y(t) = \begin{bmatrix}\vartheta^{\mathrm{T}}(t) & v_{La}(t)\end{bmatrix}^{\mathrm{T}} \in \mathbb{R}^{n+2}$ is the output vector, and

$$v_{La}(t) = D_v(t)u(t), \tag{4.23}$$

is the battery terminal voltage. All the state-space matrices are given by

$$
\begin{aligned}
A &= \begin{bmatrix} A_E & 0 \\ 0 & A_\vartheta \end{bmatrix},\ B(i_L(t)) = \begin{bmatrix} B_E i_L & 0 \\ 0 & B_\vartheta i_L^2 \end{bmatrix} M_3, \\
A_E &= 0_{n\times n},\ B_E = -\mathrm{diag}\,(b_{e1},\cdots,b_{en}) \in \mathbb{R}^{n\times n}, \\
A_\vartheta &= \begin{bmatrix} A_T & W_T \\ 0_n^{\mathrm{T}} & 0 \end{bmatrix},\quad B_\vartheta = \begin{bmatrix} B_T \\ 0_n^{\mathrm{T}} \end{bmatrix},\quad M_3 = \begin{bmatrix} I_n & -I_n \\ I_n & I_n \end{bmatrix}, \\
A_T &= [a_{tij}] \in \mathbb{R}^{n\times n},\quad B_T = \mathrm{diag}\,(b_{t1},\cdots,b_{tn}) \in \mathbb{R}^{n\times n}, \\
W_T &= \begin{bmatrix} w_{t1} & \cdots & w_{tn} \end{bmatrix}^{\mathrm{T}} \in \mathbb{R}^n, \\
C &= \begin{bmatrix} 0 & I_{n+1} \\ 0_n^{\mathrm{T}} & 0_{n+1}^{\mathrm{T}} \end{bmatrix},\ D(i_L(t)) = \begin{bmatrix} 0 \\ D_v(t) \end{bmatrix}, \\
D_v(t) &= \begin{bmatrix} D_v^+(t) & -D_v^-(t) \end{bmatrix} \in \mathbb{R}^{1\times 2n}, \qquad (4.24)
\end{aligned}
$$

where A_T is a constant lower triangular (upper triangular) thermal subsystem matrix for forward (reverse) coolant flow and the coefficients a_{tij} and w_{ti} are thermal circuit parameters. Note that D_v is a direct feedthrough gain from control u to terminal voltage v_{La} and D_v^+ and D_v^- are defined in (4.19a) and (4.19b) respectively.

The discrete-time state-space model is given by

$$x(k+1) = A_d x(k) + B_d(i_L(k))u(k), \qquad (4.25a)$$

$$y(k) = Cx(k) + D(i_L(k))u(k), \qquad (4.25b)$$

where A_d and $B_d(k)$ are obtained using Euler approximation of (4.22a) assuming i_L to be constant during each sampling interval $[kh, (k+1)h]$ where h is a sampling step size.

4.3.3 Voltage Capacity/Limit

We introduce the notion of *voltage capacity* for the modular battery. It is limited to an interval $v_{La}(k) \in [v_{L,\min}(k), v_{L,\max}(k)]$ where

$$v_{L,\min}(k) = -D_v^-(k)\cdot 1_n, \quad v_{L,\max}(k) = D_v^+(k)\cdot 1_n, \qquad (4.26)$$

are so-called minimum and maximum voltage capacities of the modular battery at any time instant for any $i_L(k) > 0$.

4.3.4 Control Constraint/Limit

The control constraint set $\mathcal{U}_i$ for Cell$_i$ is defined in (4.10). For the n-cell modular battery we get the constraint set

$$\mathcal{U} = \textstyle\prod_{i=1}^n \mathcal{U}_i = \{u | H_u u \le h_u, \}, \qquad (4.27)$$

for suitably defined H_u and h_u.

Remark 4.3. *The averaged state-space electro-thermal model of a switched modular battery is derived in a general setting applicable to both UPC and BPC mode of operation. The model is derived with careful considerations required for standard convex control problem formulation under both UPC and BPC modes in the next chapter.*

Note that the cell resistance may vary significantly over large temperature range. However, the variation is small in normal operating range $[25, 40]$ °C*. Therefore, we can assume cell resistance to be constant, during each small sampling interval, for control design [see section 6.3.3 for sensitivity analysis]. The resistance variation over large temperature range can be compensated using gain-scheduling at much slower rate.*

Chapter 5

Global Optimal Control of Modular Battery

In this chapter, the global optimal control (GOC) problem of the modular battery under both UPC and BPC modes is formulated as a state and control constrained convex optimization problem. The problem formulation is formalized such that it also becomes readily accessible for standard LQ MPC design in the next chapter. The problem is solved offline using perfect information of the battery state as well as of the complete future driving to get globally optimal power distribution among battery modules under UPC mode[1]. Under this optimal load distribution, the balancing performance of the modular battery with unidirectional coolant flow (UF) is evaluated in simulations. The performance is also compared with that under uniform duty operation (UDO) of the modular battery. In addition, the effect of reciprocating coolant flow (RF) on balancing is also analyzed.

5.1 Convex Control Problem Formulation

The GOC cannot be implemented online due to its dependence on future load demand, which is almost impossible to predict in the real world applications. However, we study it to get a performance benchmark for comparison with real-time suboptimal controllers presented in the following chapters.

The modular battery control problem boils down to the load management problem as discussed in chapters 2 and 3. The main purpose is to satisfy the power demand without draining out (SOC imbalance) and overstressing (thermal imbalance) any single battery unit. Since cells are assumed to have variations in parameters (health imbalance) and operating

[1]The control simulations in this chapter are restricted only to UPC mode of modular battery. The detailed comparative analysis of UPC and BPC is presented in next chapter.

conditions, the equal loading of cells is not a good policy for optimal battery performance. A natural question is then how to distribute demanded load among cells. For this purpose, we formulate a convex optimization problem using a criterion based on level of thermal and SOC deviations. The optimizer decides optimal power distribution among cells to minimize these deviations while meeting the total driving (or regenerating) power demand at each time instant. The decisions are globally optimal if full future driving information (i.e. load demand) is accessible. In the following, the objective function and the polyhedral constraints are carefully formulated to get the optimization problem on standard QP (quadratic programming) form.

5.1.1 State Deviations/Balancing Errors

Let us define *SOC and temperature balancing errors* for each Cell$_i$

$$e_{\xi_i}(k) = \xi_i(k) - \bar{\xi}(k), \qquad \bar{\xi}(k) = \frac{1}{n}1_n^{\mathrm{T}}\xi(k) \tag{5.1}$$

$$e_{T_{si}}(k) = T_{si}(k) - \bar{T}_s(k), \quad \bar{T}_s(k) = \frac{1}{n}1_n^{\mathrm{T}}T_s(k) \tag{5.2}$$

where $\bar{\xi}(k)$ and $\bar{T}_s(k)$ are instantaneous *mean SOC* and *mean temperature* of the modular battery and can be considered as reference signals here. Now using (5.1) and (5.2), we can define *SOC and temperature error vectors*

$$e_{\xi}(k) = \xi(k) - \bar{\xi}(k) \cdot 1_n = M_e\xi(k), \tag{5.3}$$

$$e_{T_s}(k) = T_s(k) - \bar{T}_s(k) \cdot 1_n = M_eT_s(k), \tag{5.4}$$

where the matrix

$$M_e = \left(I_n - \tfrac{1}{n}1_{n\times n}\right) \in \mathbb{R}^{n\times n}, \tag{5.5}$$

maps each state vector to its corresponding error vector. The *control objective* is to minimize these errors (simultaneous thermal and SOC balancing) and reduce mean battery temperature while regulating the battery terminal voltage at the demand setpoint using $u \in \mathcal{U}$ as described below.

5.1.2 Design of Objective Function

The SOC balancing is needed to keep cells balanced at least at SOC-boundaries (i.e. end-of-charge (EOC) and end-of-discharge (EOD) states) during charge/discharge cycling of the battery to avoid non-uniform ageing [18]. In other words, a *temporary SOC imbalance* during cycling may be allowed if cells are balanced at EOC and EOD. However, in vehicle applications, the lower SOC boundary (terminal time of journey) is normally not fixed due to uncertainties in the drive cycle. Therefore, we propose to reduce SOC deviations as much as possible during cycling to get fairly balanced DODs by the end of the drive cycle. Similarly, we propose to minimize temperature deviations all the time during cycling because cell ageing is exponential in cell temperature [17]. These minimizations must be achieved without increasing average battery temperature relative to that of unbalanced battery and by using minimum possible actuation of cells. These objectives are formulated as the following cost functions

$$J_E = \sum_{k=0}^{N-1} \|e_\xi(k)\|^2_{Q_E} + \|e_\xi(N)\|^2_{P_E}, \tag{5.6a}$$

$$J_T = \sum_{k=0}^{N-1} \|e_{T_s}(k)\|^2_{Q_T} + \|e_{T_s}(N)\|^2_{P_T}, \tag{5.6b}$$

$$J_{\bar{T}} = \sum_{k=0}^{N-1} \|\bar{T}_s(k)\|^2_{q_{\bar{t}}} + \|\bar{T}_s(N)\|^2_{p_{\bar{t}}}, \tag{5.6c}$$

$$J_u = \sum_{k=0}^{N-1} \|u(k)\|^2_{R_u}, \tag{5.6d}$$

where N is prediction horizon, $Q_E = q_e I_n, P_E = p_e I_n, Q_T = q_t I_n$, and $P_T = p_t I_n$ are positive semidefinite penalty matrices for deviations, $q_e, p_e, q_t, p_t, q_{\bar{t}}$, and $p_{\bar{t}}$ are nonnegative scalar weights, and $R_u = \text{blkdiag}(R_{u^+}, R_{u^-})$ is a positive definite penalty matrix for control where R_{u^+} and R_{u^-} are penalties on u^+ and u^- (positive and negative controls) respectively. We use $R_{u^-} \gg R_{u^+}$ to reduce subsequent extra losses due to negative cell actuation. We have multiple objectives and it is impossible to minimize them individually. Therefore, we formulate a scalar objective function, given by

$$J = \gamma_1 J_E + \gamma_2 J_T + \gamma_3 J_{\bar{T}} + \gamma_4 J_u, \tag{5.7}$$

where $\gamma_i \geq 0$ are *trade-off weights*, which signify the relative importance of each objective. These weights are chosen such that $\sum_i^4 \gamma_i = 1$.

Objective Function on Standard Form

The objective function (5.7) is quadratic in terms of state errors, whereas system dynamics (4.25a) is written in terms of states. Therefore, we apply transformations (5.3) and (5.4) to get the following standard quadratic objective function

$$J = \sum_{k=0}^{N-1} \left[\|x(k)\|^2_{\bar{Q}_x} + \gamma_4 \|u(k)\|^2_{R_u} \right] + \|x(N)\|^2_{\bar{P}_x}, \tag{5.8}$$

in terms of $x(k)$ and $u(k)$, where

$$\bar{Q}_x = \text{blkdiag}\left(\gamma_1 \bar{Q}_E, \gamma_2 \bar{Q}_T + \gamma_3 \bar{Q}_{\bar{T}}, 0\right), \tag{5.9}$$

$$\bar{P}_x = \text{blkdiag}\left(\gamma_1 \bar{P}_E, \gamma_2 \bar{P}_T + \gamma_3 \bar{P}_{\bar{T}}, 0\right), \tag{5.10}$$

are new penalty weight matrices with

$$\bar{Q}_E = M_e^{\mathrm{T}} Q_E M_e, \ \ \bar{P}_E = M_e^{\mathrm{T}} P_E M_e, \tag{5.11a}$$

$$\bar{Q}_T = M_e^{\mathrm{T}} Q_T M_e, \ \ \bar{P}_T = M_e^{\mathrm{T}} P_T M_e, \tag{5.11b}$$

$$\bar{Q}_{\bar{T}} = \frac{q_{\bar{t}}}{n^2} 1_{n\times n}, \qquad \bar{P}_{\bar{T}} = \frac{p_{\bar{t}}}{n^2} 1_{n\times n}, \tag{5.11c}$$

where the matrix M_e is defined in (5.5).

5.1.3 State Constraints

Running State Constraints

The balancer must ensure the following constraints

$$\xi_{\min} \le \xi(k) \le \xi_{\max}, \ \forall k \tag{5.12a}$$

$$|e_{\xi_i}(k)| \le \delta\xi, \ \forall i, \ \forall k \ge k_b, \tag{5.12b}$$

$$T_{s,\min} \le T_s(k) \le T_{s,\max}, \ \forall k \tag{5.12c}$$

$$|e_{T_{si}}(k)| \le \delta T_s, \ \forall i, \ \forall k \tag{5.12d}$$

for ideal SOC and thermal balancing during driving, where vectors $\xi_{\min}/T_{s,\min}$ and $\xi_{\max}/T_{s,\max}$ give minimum and maximum limits of SOC/temperature for each cell, scalars $\delta\xi$ and δT_s are *SOC and thermal deviation allowances* for all cells, and k_b is an initial *balancing time period.* From constraint (5.12a) for $k = 0$, we can define the *initial set* of SOCs as the following polyhedron

$$\mathcal{X}_{E0} = \{\xi | H_{E0}\xi \le h_{e0}\}, \tag{5.13}$$

for suitably defined constraint matrix H_{E0} and vector h_{e0}. Similarly, by first applying transformations (5.3) and (5.4) to (5.12b) and (5.12d) respectively and then using (5.12a)–(5.12b) and (5.12c)–(5.12d), we can easily define *goal/target sets* of SOCs and temperatures as the following polyhedra

$$\mathcal{X}_{Eg} = \{\xi | H_{Eg}\xi \le h_{eg}\}, \ \mathcal{X}_{Tg} = \{T_s | H_{Tg} T_s \le h_{tg}\}, \tag{5.14}$$

for suitably defined constraint matrices H_{Eg}, H_{Tg} and vectors h_{eg}, h_{tg}. The *primary goal* of thermal and SOC balancing during is to first drive SOC of all cells from $\xi(0) \in \mathcal{X}_{E0}$ to $\xi(k_b) \in \mathcal{X}_{Eg}$ within a certain balancing time $t_b = hk_b$ and then keep them there for all $k \ge k_b$, whereas temperature of all cells must stay within $\mathcal{X}_{Tg}$ all the time.

Terminal State Constraint

If the drive cycle is known a priori (as in this chapter) then the balancer may also achieve a *secondary goal* i.e., perfect SOC equalization by the end of driving trip. This can be specified as the following terminal constraint

$$\xi_i(N_d) = \xi_j(N_d), \forall i, j. \tag{5.15}$$

5.1.4 Output Voltage Tracking Constraint

In addition to balancing, the battery must strictly satisfy the load voltage demand $v_{Ld}(k)$. Using voltage equation (4.23), this is modeled as the following voltage tracking constraint

$$v_{La}(k) = D_v(k)u(k) = v_{Ld}(k) \tag{5.16}$$

where $D_v(k)$ is defined in equation (4.24).

5.1.5 Constrained Convex Optimization Problem

Let us assume the load demand $(i_L(k), v_{Ld}(k))$ over the whole driving cycle of length N_d is fully accessible. Now using the objective function and constraints defined above along with the battery dynamic and control constraints (see (4.25a) and (4.27)), the globally optimal load sharing (GOC) is achieved by solving offline the following convex optimization problem,

$$\begin{aligned}
&\text{minimize } J(x(0), u(0:N_d-1)) \\
&\text{subject to} \\
&x(k+1) = A_d x(k) + B_d(k)u(k), \\
&D_v(k)u(k) = v_{Ld}(k), \\
&\xi(k) \in \mathcal{X}_{Eg},\ \forall k \geq k_b,\ T_s(k) \in \mathcal{X}_{Tg}, \\
&\xi_i(N_d) = \xi_j(N_d),\ \forall i, j \\
&u(k) \in \mathcal{U},
\end{aligned} \tag{P-I}$$

with optimization variables $x(k)$ and $u(k)$ for all $k \in \{0, \cdots, N_d - 1\}$ where the objective function J is defined in (5.8) and the control constraint set $\mathcal{U}$ is defined in (4.27). Note that the initial balancing time period k_b is not fixed as it depends on characteristics of the load profile. To make the problem independent of k_b, we can soften state inequality constraints using a slack variable approach [90]. The GOC is summarized as Algorithm 1.

Algorithm 1 Global optimal control (GOC)

Data: Current state $x(k)$ and load demand for complete drive cycle
Compute full control sequence $\{u(k)\}_{k=1}^{N_d}$ by solving (P-I) offline
for $k = 1$ to N_d **do**
    Apply control $u(k)$ to the modular battery system
end for

5.2 Simulation Setup

5.2.1 Battery Performance Variables

To illustrate the balancing performance in next section, we use $\|e_\xi(k)\|_\infty$ and $\|e_{T_s}(k)\|_\infty$ [e_ξ and e_{T_s} are defined in (5.3) and (5.4)] i.e., the maximum SOC and temperature deviations (balancing errors) in the battery at any time instant. Similarly, to analyze the control behavior, we introduce average and rms cell currents over the whole drive cycle, given by

$$I_{Bai} = \frac{1}{N_d} \sum_{k=1}^{N_d} h \cdot i_{Bai}(k), \tag{5.17a}$$

$$I_{Bri}^2 = \frac{1}{N_d} \sum_{k=1}^{N_d} h \cdot i_{Bri}^2(k), \tag{5.17b}$$

where i_{Bai} and i_{Bri}^2 are defined in (4.14) and (4.15) respectively.

5.2.2 Battery Configuration

The modular battery considered for this simulation study consists of 4 modules, each containing one cell (3.3V, 2.3Ah, A123 ANR26650M1A). The nominal values of the electro-thermal parameters, shown in Table 5.1, have been taken from [35–37]. The true cells are assumed to have capacity, resistance, and initial SOC variations (i.e., $C_{ei} \neq C_{ej}$, $R_{ei} \neq R_{ej}$, and $\xi_i(0) \neq \xi_j(0), \forall i, j$) to thoroughly evaluate the controller performance. All other electro-thermal parameters are assumed equal. It is also realistic to assume that all cells have same initial temperature. There are various possible initial conditions of the battery depending on capacity, resistance, and initial SOC combination for each cell. For instance, for any two cells (Cell$_i$ and Cell$_j$) in the modular battery, we have four possible cases:

- Case-1: $C_{ed,i}(0) < C_{ed,j}(0)$ and $R_{ei} < R_{ej}$,

Table 5.1: Cell parameters and controller setting

Parameter	**Symbol**	**Value**	Unit
	Cell Parameters		
No. of Cells	n	4	-
Nominal OCV	$v_{oci}^{\star}$	3.3	V
Nominal Resistance	$R_{ei}^{\star}$	11.4	$m\Omega$
Nominal Capacity	$C_{ei}^{\star}$	2.3	Ah
Cell Heat Capacity	C_{si}	71.50, $\forall i$	JK^{-1}
Convective Thermal Resistance	R_{ui}	3.03, $\forall i$	KW^{-1}
Air Flow Rate	$\dot{V}_f$	0.0095	m^3s^{-1}
Air Thermal Conductance	c_f	11.1105	WK^{-1}
Inlet Fluid Temperature	T_{f0}	25	℃
Load Voltage Demand	v_{Ld}	9.25	V
OCV Vector	v_{oc}	$v_{oci}^{\star}1_n$	V
	Controller Setting		
SOC Deviation Allowance	$\delta\xi$	2.5%	-
Temp. Deviation Allowance	δT_s	1	℃
Sampling Interval	h	1	s

- Case-2: $C_{ed,i}(0) > C_{ed,j}(0)$ and $R_{ei} < R_{ej}$,
- Case-3: $C_{ed,i}(0) < C_{ed,j}(0)$ and $R_{ei} > R_{ej}$,
- Case-4: $C_{ed,i}(0) > C_{ed,j}(0)$ and $R_{ei} > R_{ej}$.

Note that, during discharging, case-1 and case-4 are more challenging because a cell with higher resistance is also the one with higher initial dischargeable capacity. This implies conflicting cell usage requirements for thermal and SOC balancing. Therefore, it is interesting to consider a parametric variation profile of the modular battery, as shown in Figure 5.1, where at least one cell pair in the string satisfies either case-1 or case-4. The true values of parameters and initial SOCs of cells are given below.

$$\begin{aligned} R_e &= \begin{bmatrix} 11.7 & 13.3 & 16.1 & 16.8 \end{bmatrix}^{\mathrm{T}} \; m\Omega, \\ C_e &= \begin{bmatrix} 2.29 & 2.26 & 2.11 & 1.98 \end{bmatrix}^{\mathrm{T}} \; Ah, \\ \xi(0) &= \begin{bmatrix} 0.75 & 0.78 & 0.88 & 0.90 \end{bmatrix}^{\mathrm{T}}. \end{aligned}$$

5.2.3 Battery Load Profile

The balancing performance, in this study, has been thoroughly evaluated under various driving behaviors/situations. We show results particularly for three drive cycles namely

- *SCM17kmA6* [91]: It is a representative of low speed urban stop-n-go real world driving behavior (benign to mild) on a 17 km route in west Sweden.
- *Standard ARTEMIS Rural*: It is a representative of high speed rural driving behavior (normal to intensive).
- *US06*: It is a representative of very high speed highway driving behavior (aggressive).

The real battery current measurement data for *SCM17kmA6* were obtained from *Swedish Car Movement database* [92], whereas the battery current data for ARTEMIS Rural and US06 were obtained by simulation of Toyota Prius PHEV in full EV mode in *Advisor* [93]. The scaled battery load current data and its histogram for each drive cycle are shown in Figure 5.2. The demanded battery load voltage is assumed as a constant dc-link voltage of a three-phase two-level inverter of Toyota Prius PHEV. A certain level of surplus voltage (or cell redundancy) needed to achieve voltage regulation and balancing depends on the drive cycle. The voltage setting $v_{Ld} = 9.25\,V$ is used to ensure problem feasibility [cf. condition (6.8)] for all three drive cycles for the case of four cell battery considered in this study.

5.2.4 Control Setting and Solution

The control objective is to bring SOC deviation within maximum 2.5% as fast as possible while keeping temperature deviation within 1℃ all the time for all the selected drive cycles. The controller has been tuned using first Bryson's rule [94, pg.537] and then iterative trial and error method. The simulation study is based on the numerical solution of the global optimal control problem (P-I) with the above setting. To solve problem (P-I), we used SDPT3 solver in `CVX`, which is a MATLAB-based package for specifying and solving convex programs using disciplined convex programming ruleset [95–97].

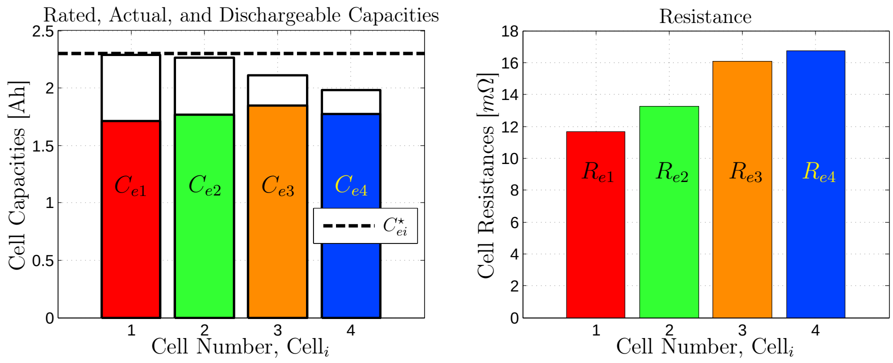

(a) Capacity distribution. (b) Resistance distribution.

Figure 5.1: Capacity and resistance distribution of cells. In Fig. 5.1(a), the level inside each container shows initial dischargeable capacity of cell.

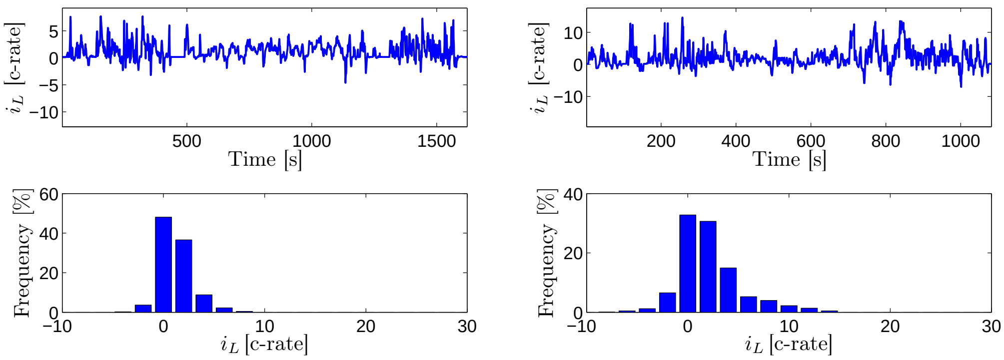

(a) SCM17kmA6. (b) Standard ARTEMIS Rural.

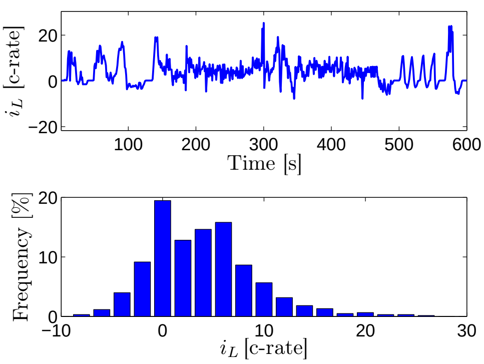

(c) US06.

Figure 5.2: Battery load current and the histogram for three drive cycles. The histograms show the spread of load intensity in each drive cycle.

5.3 Simulation Results and Discussion

In this section, the performance of GOC is evaluated for the modular battery under unidirectional coolant flow. The performance is also compared with uniform usage of battery cells. In addition, the significance of using reciprocating coolant flow for GOC is also briefly discussed. The results are presented here only for US06 drive cycle.

5.3.1 Global Optimal Control Performance

The simulation results are shown in Figure 5.3 for both UDO and GOC. The figure is a 4×2 matrix of subfigures where two columns correspond to UDO and GOC respectively and each row corresponds to one of the four battery performance variables: $v_L(k), \xi(k), T_s(k)$, and $\{\|e_\xi(k)\|_\infty, \|e_{T_s}(k)\|_\infty\}$.

The uniform usage (UDO) of cells is not optimal because cells are not uniform in parameters. For example, if all cells in the string, with variations in dischargeable capacities, are equally loaded (same average current) then Cell_1 with lower dischargeable capacity gets empty prior to other cells as shown in Figure 5.3(c). Similarly, if all cells in the string, with variations in resistances, are equally loaded (same rms current) during whole drive cycle then Cell_4 with higher resistance naturally generates more heat, which leads to higher temperature as shown in Figure 5.3(e). Therefore, the UDO may reduce the effective capacity as well as the lifetime of the battery.

The GOC, on the other hand, reduces SOC deviation among cells with the passage of time and makes it zero by the end of journey as shown in Figures 5.3(d) and 5.3(h). This is achieved while keeping temperature deviation within the specified limit of 1 ℃, despite significant deviation among cell resistances, during whole driving as shown in Figures 5.3(f) and 5.3(h). The simultaneous thermal and SOC balancing performance is achieved while regulating the battery voltage at the demand setpoint as shown in Figure 5.3(b). It is important to note that the GOC achieves balancing without increasing peak battery temperature. In fact, it reduces temperature of Cell_4 by more than 1 ℃ as shown in Figure 5.3(f). Since cell capacity fading is exponential in temperature (see the cycle-life model (2.2)), Cell_4 of the modular battery may have longer lifetime than that under UDO. Therefore, the optimal load sharing among cells of the modular battery may increase its lifetime as well as its effective capacity.

5.3.2 Optimal Load Sharing

Figure 5.4 shows bar plots of average and rms currents (I_{Bai}, I_{Bri}), defined in (5.17a) and (5.17b), of each cell computed under UDO and GOC over

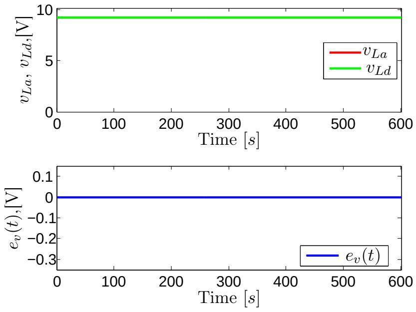

(a) *UDO*: Voltage response.

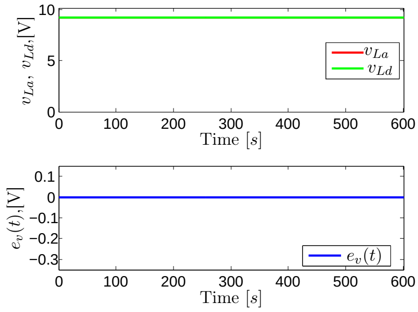

(b) *GOC*: Voltage response.

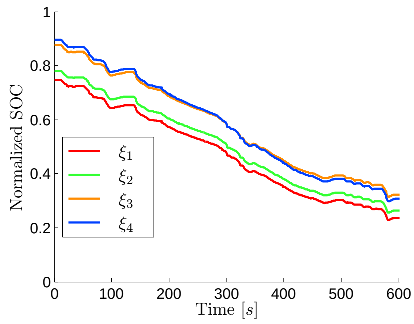

(c) SOC balancing.

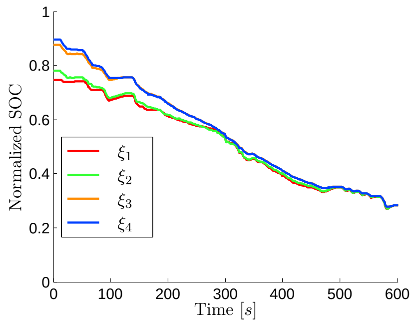

(d) SOC balancing.

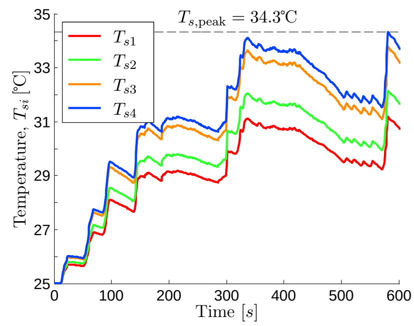

(e) Thermal balancing.

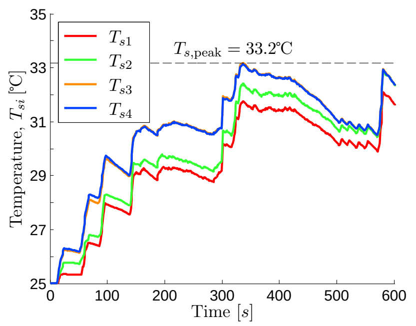

(f) Thermal balancing.

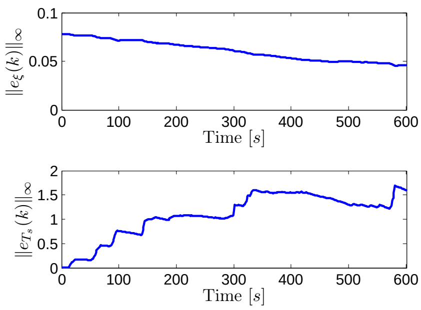

(g) Balancing errors.

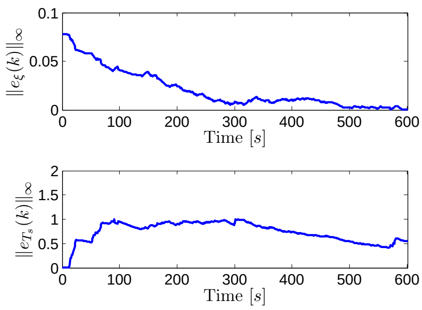

(h) Balancing errors.

Figure 5.3: Simulation results for electro-thermal control performance under *US06 drive cycle* are shown: *Uniform Duty Operation (UDO)*: first column; *Global Optimal Control (GOC)*: second column.

whole drive cycle. The figure is a 2×2 matrix of subfigures where the first row corresponds to average currents and the second row corresponds to rms currents under UDO and GOC in the first and second column respectively.

The UDO results in equal average and rms current for each cell. This is of course not optimal as cells have different dischargeable capacities and resistances as shown in Figure 5.1. The GOC, on the contrary, generates load distribution according to cell parameters. For example, it decides the average current distribution that resembles the dischargeable capacity distribution (compare Figure 5.4(b) with 5.1(a)). This is the optimal load distribution pattern because cells with lower dischargeable capacity (Cell_1 and Cell_2) must see less average current relative to those with higher dischargeable capacity (Cell_3 and Cell_4) for SOC balancing. Similarly, it decides rms current distribution that resembles the mirror image of resistance distribution (compare Fig. 5.4(d) with 5.1(b)). This is also optimal because cells with higher resistance (Cell_3 and Cell_4) must see less rms current relative to those with lower resistance (Cell_1 and Cell_2) for thermal balancing.

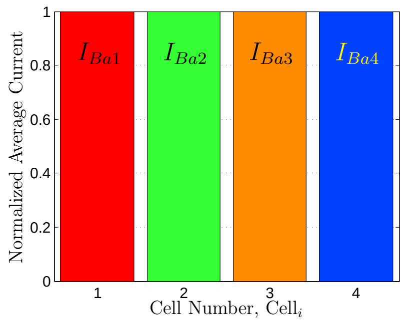

(a) *UDO*: Cell average currents.

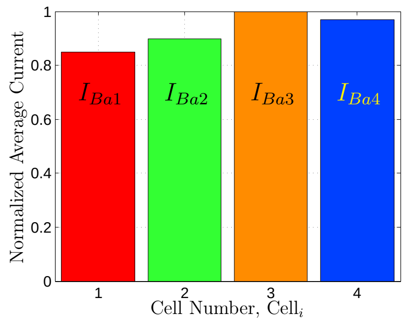

(b) *GOC*: Cell average currents.

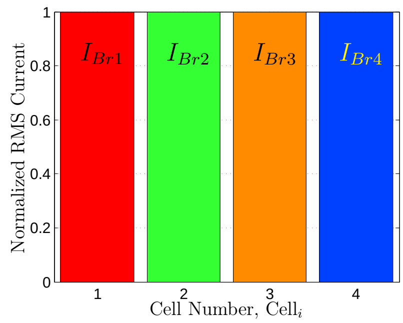

(c) *UDO*: Cell rms currents.

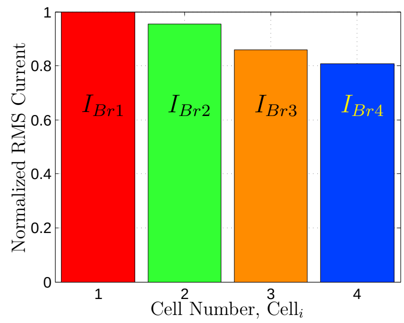

(d) *GOC*: Cell rms currents.

Figure 5.4: GOC versus UDO: Cell average and rms current behavior under US06 drive cycle. Note that the GOC assigns average and rms current level for each cell according to its dischargeable capacity and resistance.

5.3.3 Impact of Reciprocating Air Flow

The effect of RF on thermal balancing performance of GOC is investigated and compared with that under UF. The results are shown in Figure 5.5. These figures clearly show that GOC has no significant gain from RF for short battery strings because the coolant gradient is not that large. The GOC with UF is sufficient indeed to achieve temperature uniformity by optimally shifting the power losses among the cells. However, the temperature gradient may be quite significant in large battery packs with long strings of cells. In such applications, the RF can save some control effort of GOC by reducing the coolant temperature gradient. This extra control effort can then be invested for better compensation of state deviations arising from parametric variations. Thus, the use of RF in large battery packs may complement optimal load sharing for thermal balancing [see Chapter 9].

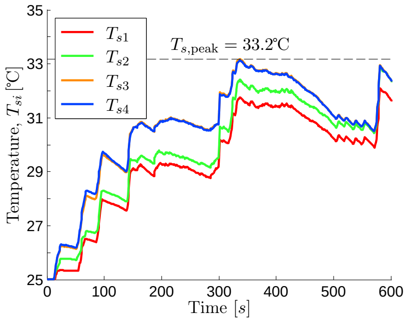

(a) *GOC-UF*: thermal balancing.

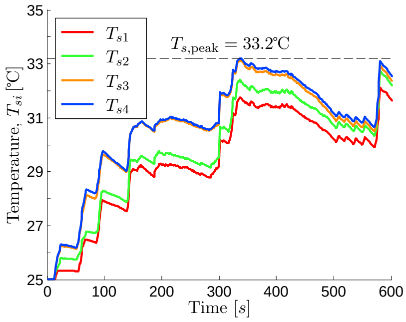

(b) *GOC-RF*: thermal balancing.

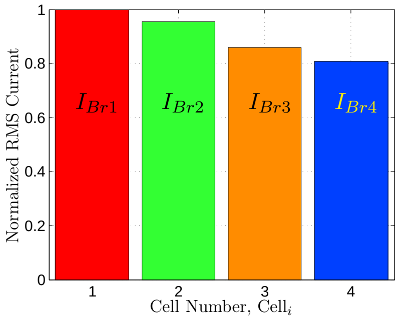

(c) *GOC-UF*: rms currents.

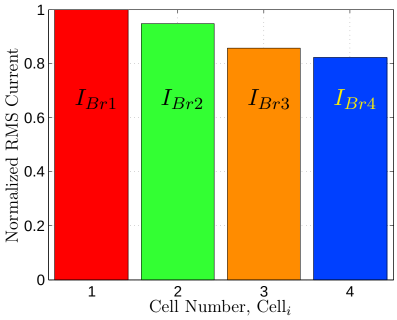

(d) *GOC-RF*: rms currents.

Figure 5.5: Effect of RF on thermal balancing performance of GOC: *GOC under UF*: first column; *GOC under RF*: second column. The RF gives no extra benefit to GOC for thermal balancing of short battery strings.

5.4 Summary and Conclusions

This chapter investigated the potential benefit of optimal load sharing among cells of the modular battery for simultaneous thermal and SOC balancing. The load sharing problem is formulated as a constrained convex optimization problem. The problem is solved offline to get globally optimal control (GOC) actions (duty cycles) for each cell based on the assumption of perfect information about the battery state and the future load over whole drive cycle. The simulation results show that, despite significant parametric variations among battery cells, GOC under UF optimally uses the extra DoF of the modular battery to significantly reduce balancing errors compared to uniform usage (UDO) of cells. In a nutshell, the controller achieves SOC and thermal balancing by optimally distributing the average and rms currents among the cells according to their parameters and positions in the string. It is also shown that RF has no significance for the controller in short battery strings. However, for long battery strings, the RF may facilitate the controller to generate even better load distribution for improving its thermal balancing performance.

Chapter 6

Model Predictive Control of Modular Battery

In almost all practical applications, the full drive cycle is hardly known a priori. Therefore, the problem (P-I) given on page 59 cannot be solved. Since it may still be possible to achieve load predictions over short horizon, the model predictive control (MPC) framework [90] is a natural choice to solve battery load management problem. This chapter proposes a novel control algorithm based on linear quadratic (LQ) MPC for both UPC and BPC modes. The main purpose is to achieve the balancing objectives by using load forecast over a very short prediction horizon ($N \ll N_d$). In addition, the use of LQ formulation is convenient for studying the balancing control structure. The control scheme is thoroughly evaluated through simulations under different driving behaviors. The structural, functional, and robustness properties of the controller are also analyzed. Moreover, the merits and demerits of both UPC and BPC modes are thoroughly investigated in terms of their balancing performance as well as energy efficiency.

6.1 Main Idea: Control Separation

The LQ MPC scheme is developed with the following aims.

- The load voltage regulation is prioritized and thermal and SOC balancing are achieved as secondary objectives.
- To secure feasibility, we aim to achieve balancing objectives without imposing any hard state constraints.
- The voltage constraint in problem (P-I) poses an issue for transforming it to standard LQ form. This issue is addressed in a special way by separating voltage and balancing control tasks as described below.

Keeping in view all the above aims, we propose to decompose the control problem into two subproblems:

1. *Voltage Controller* $[u_v(k)]$*:* It is a feedforward controller, which uses information only about load demand $v_{Ld}(k)$ and $i_L(k)$ given at each time instant, to generate $v_{La}(k) = v_{Ld}(k)$. The control signal $u_v(k)$ is computed analytically (*minimum norm solution*), see section 6.2.2.

2. *Balancing Controller* $[u_b(k)]$*:* It is a feedback controller that uses information about battery state $x(k)$, load current $i_L(k)$, and voltage control $u_v(k)$, to achieve thermal and SOC balancing. We propose to choose the optimal control decision $u_b(k)$ such that it is always *orthogonal* to $u_v(k)$. This guarantees the voltage constraint satisfaction while giving the possibility of simultaneous balancing. The balancing control $u_b(k)$ is computed in receding horizon fashion based on *control-constrained LQ* problem (LQ MPC problem), see section 6.2.3.

This novel approach of separating balancing controller from voltage controller offers multiple advantages. Firstly, this method facilitates the formulation of the electro-thermal control problem on standard LQ MPC form. Secondly, we can pre-compute and store in memory voltage control decisions for a pre-selected grid of demanded load currents and voltages. Thirdly, it gives us more insight into structural and functional properties of the controller. All the important ingredients of the proposed control scheme are presented below in detail.

6.2 MPC Problem Formulation

6.2.1 Orthogonal Control Decomposition

Let us consider the voltage constraint $(D_v(k)u(k) = v_{Ld}(k))$ in the optimization problem (P-I). We have only one output equality constraint to satisfy using $2n$ control variables. Hence, there are multiple solutions and the nullspace of D_v provides $2n - 1$ degrees-of-freedom in generating v_L. This extra freedom can be used for the balancing objectives.

The main idea is to decompose the control signal into two orthogonal components, one for voltage control and the other for balancing control. Using the decomposition theorem of linear algebra [98, Thm 3.14], we propose the following unique decomposition of *total control vector* $u \in \mathcal{U} \subseteq \mathbb{R}^{2n}$

$$\begin{aligned} &u(k) = u_v(k) + u_b(k), \\ &u_v(k) \in \mathcal{N}(D_v(k))^{\perp}, \quad u_b(k) \in \mathcal{N}(D_v(k)), \end{aligned} \tag{6.1}$$

where $\mathcal{N}(D_v(k))$ is the time-varying nullspace of $D_v(k)$ and $\mathcal{N}(D_v(k))^{\perp}$ is its orthogonal complement. The nullspace is a hyperplane in $\mathbb{R}^{2n}$ given by

$$\mathcal{N}(D_v) = \{u(k)|D_v(k)u(k) = 0\} = \mathcal{R}(V_{\mathrm{n}}) \subseteq \mathbb{R}^{2n}, \tag{6.2}$$

where $\mathcal{R}(V_{\mathrm{n}})$ is the range-space of null-space basis matrix

$$V_{\mathrm{n}}(k) = \begin{bmatrix} v_{\mathrm{n},1}(k) & \cdots & v_{\mathrm{n},2n-1}(k) \end{bmatrix} \in \mathbb{R}^{2n \times 2n-1},$$

which contains parameterized orthonormal basis vectors $v_{\mathrm{n},i}(k) \in \mathbb{R}^{2n}$ of null-space where the subscript 'n' stands for nullspace. The basis $V_{\mathrm{n}}(k)$ of nullspace is not unique. A particular choice, obtained using MATLAB® Symbolic Toolbox, is given by

$$V_{\mathrm{n}}(k) = \begin{bmatrix} V_{\mathrm{n}}'(k) \\ I_{2n-1} \end{bmatrix}, \tag{6.3}$$

where $V_{\mathrm{n}}' = \begin{bmatrix} -\frac{D_v^+(2:n)}{d_{v1}^+} & \frac{D_v^-}{d_{v1}^+} \end{bmatrix} \in \mathbb{R}^{1\times(2n-1)}$, D_v^+ and D_v^- are defined in (4.19a) and (4.19b), and $D_v^+(2:n)$ (indexed using Matlab notation) is a row vector with last $n-1$ elements of D_v^+. The orthogonal complement of nullspace is given by

$$\mathcal{N}(D_v)^{\perp} = \mathcal{R}(D_v^{\mathrm{T}}) = \{u(k)|u(k) = \alpha_v(k)D_v(k)^{\mathrm{T}}\}, \tag{6.4}$$

where α_v is a scalar parameter. Now we are ready to design u_v and u_b constrained inside time-varying orthogonal subspaces $\mathcal{R}(D_v^{\mathrm{T}})$ and $\mathcal{N}(D_v)$ respectively. The formulation of voltage and balancing control problems for BPC mode is given below, and UPC is treated as a special case of BPC.

6.2.2 Voltage Controller: Minimum Norm Problem

A unique solution $u_v \in \mathcal{N}(D_v)^{\perp}$ is given by the least norm problem[1] i.e.,

$$\begin{aligned} \text{minimize} \quad & \|u_v(k)\|^2 \\ \text{subject to} \quad & D_v(k)u_v(k) = v_{Ld}(k), \\ & u_v(k) \in \mathcal{U}. \end{aligned} \tag{P-II}$$

This problem has an analytical solution for load current demand $i_L(k) \in [i_{L,\min}, i_{L,\max}]$ and load voltage demand $v_{Ld} \in [0, v_{Ld,\max}]$ with appropriate

[1] It is well-known from linear algebra [98, Theorem 6.3] that any vector linear equation $Ax = b$ with $AA^{\dagger}b = b$ (i.e. A is right invertible) has a general solution of the form $x = A^{\dagger}b + (I - A^{\dagger}A)y$ where $A^{\dagger}$ is the right pseudo-inverse, y is an arbitrary vector, and $I - A^{\dagger}A$ is the orthogonal projection on the nullspace $\mathcal{N}(A)$. It is also known that the particular solution $x = A^{\dagger}b$ is the solution that has minimum Euclidean norm $x^{\mathrm{T}}x = \|x\|_2^2$. This motivates the formulation of the problem (P-II).

limits $i_{L,\min}, i_{L,\max}$, and $v_{Ld\max} < v_{L,\max}(k)$. To derive this analytical solution, let us represent the equality constraint in (P-II) by

$$v_{Ld} = D_v(k)u_v(k) = D_v^+(k)u_v^+(k) - D_v^-(k)u_v^-(k) \tag{6.5}$$

where $D_v^+(k) \geq 0$ and $D_v^-(k) \geq 0$ are defined in (4.19a) and (4.19b) respectively. Since increasing u_v^- always decreases the terminal voltage v_{La} for any given u_v^+, it is not optimal to use u_v^- to generate voltage v_{La} as it increases the length of vector u_v. Therefore, the optimizer must set

$$u_v^- = 0, \tag{6.6}$$

to minimize the norm[2] of u_v. Therefore, the problem (P-II) is equivalent to

$$\begin{array}{ll} \text{minimize} & \|u_v^+(k)\|^2 \\ \text{subject to} & D_v^+(k)u_v^+(k) = v_{Ld}(k), \\ & u_v^+(k) \in \mathcal{U}^+, \end{array} \tag{P-III}$$

which is simpler than (P-II) and has an analytical solution given by

$$u_v^+(k) = \left(D_v^+(k)\right)^\dagger v_{Ld}(k), \tag{6.7}$$

where $(D_v^+)^\dagger = D_v^{+\mathrm{T}}\left(D_v^+ D_v^{+\mathrm{T}}\right)^{-1}$ is a right pseudo-inverse of D_v^+. The solution is guaranteed to be inside $\mathcal{U}^+$ under the following conditions. If the current demand $i_L(k)$ stays within absolute maximum current rating of a cell then $D_v^+(k)$ is always positive, which implies that $(D_v^+(k))^\dagger$ is also positive. Therefore, the analytical solution (6.7) is positive (i.e. $u_v^+(k) \geq 0_n$) for $v_{Ld} \geq 0$ and $i_L(k) \in [i_{L,\min}, i_{L,\max}]$. In addition, the solution (6.7) is less than unity (i.e. $u_v^+(k) < 1_n$) if the voltage demand $v_{Ld} \in [0, v_{Ld,\max}]$ with

$$v_{Ld,\max} < v_{L,\max}(k), \quad \forall k \tag{6.8}$$

where $v_{L,\max}(k)$, defined in (4.26), is the maximum voltage capacity of the modular battery. Hence, $u_v^+ \in \mathcal{U}^+$ is guaranteed under above stated conditions. The complete solution is given by

$$u_v(k) = \begin{bmatrix} u_v^+(k) \\ u_v^-(k) \end{bmatrix} = \begin{bmatrix} (D_v^+(k))^\dagger \\ 0_n \end{bmatrix} v_{Ld}(k) \in \mathcal{N}(D_v)^\perp. \tag{6.9}$$

Note that u_v is a feedforward control, which is computed based on the load demand v_{Ld} and i_L at each time instant.

[2]This claim, shown here based on a simple argument, can also be proved formally using KKT conditions from mathematical optimization theory.

6.2.3 Balancing Controller: LQ MPC Problem

After computing the voltage control decision $u_v(k)$, the balancing control $u_b(k) \in \mathcal{N}(D_v)$ can be chosen using MPC scheme to achieve thermal and SOC balancing objectives. Before presenting this scheme, let us first represent the balancing control as follows

$$u_b(k) = \sum_{i=1}^{2n-1} \rho_{bi}(k) v_{\mathrm{n},i}(k) = V_{\mathrm{n}}(k)\rho_b(k) \in \mathcal{U}_b, \tag{6.10}$$

where $V_{\mathrm{n}}(k)$ is given by (6.3) and $\rho_b(k) \in \mathbb{R}^{2n-1}$ are coefficients of null-space basis vectors, and $\mathcal{U}_b(k)$ defined by (6.11) below is a balancing control constraint set. Note that using ρ_b as a control input reduces optimal decision search from $\mathbb{R}^{2n}$ to $\mathbb{R}^{2n-1}$. This new control variable is equal to last $2n-1$ elements of u_b for the particular choice of V_{n} given by (6.3).

Balancing Control Constraint Polytope

The null-space coefficients $\rho_b(k)$ must be chosen such that the total control $u(k) \in \mathcal{U}$. This means we can only choose balancing control from the following so-called truncated null-space $\mathcal{U}_b \subseteq \mathcal{N}(D_v)$

$$\mathcal{U}_b(k) = \{u_b(k) = V_{\mathrm{n}}(k)\rho_b(k) \,|\, (u_v(k) + u_b(k)) \in \mathcal{U}\}. \tag{6.11}$$

In simple words, choosing $u_b \in \mathcal{U}_b$ guarantees $u \in \mathcal{U}$ at each time instant without violating voltage constraint.

Constrained LQ MPC Standard Form

The control coefficients $\rho_b(k)$ are computed by solving a constrained LQ problem in a receding horizon fashion. Before presenting the problem, let us substitute $u(k)$ with $u_b(k) = V_{\mathrm{n}}(k)\rho_b(k)$ in (4.25a) and (5.8), to get the system dynamics and the objective function on the following standard forms in terms of $x(k)$ and $\rho_b(k)$

$$x(k+\ell+1) = A_d x(k+\ell) + \bar{B}_d(k+\ell)\rho_b(k+\ell), \tag{6.12}$$

$$J = \sum_{\ell=0}^{N-1} \Big[\|x(k+\ell)\|^2_{\bar{Q}_x} + \|\rho_b(k+\ell)\|^2_{R_{\rho_b}} \Big] + \|x(k+N)\|^2_{\bar{P}_x}, \tag{6.13}$$

where ℓ is the MPC prediction phase time index, $\bar{B}_d(\cdot) = B_d(\cdot)V_{\mathrm{n}}(\cdot)$, and

$$R_{\rho_b}(k+\ell) = \gamma_4 V_{\mathrm{n}}^{\mathrm{T}}(i_L(k+\ell)) R_{u_b} V_{\mathrm{n}}(i_L(k+\ell)), \tag{6.14}$$

is a time-varying penalty for ρ_b. The matrix $R_{u_b} = \text{blkdiag}(R_{u_b^+}, R_{u_b^-})$ is a penalty weight for u_b where $R_{u_b^+}$ and $R_{u_b^-}$ are penalties on u_b^+ and u_b^- (positive and negative balancing controls) respectively. We use $R_{u_b^-} \gg R_{u_b^+}$ to reduce subsequent extra losses due to negative cell actuation. Now using (6.12) and (6.13), the *balancing control problem* can be easily formulated on the following standard *control-constrained LQ* form,

$$
\begin{aligned}
&\text{minimize} \quad J(x(k), \rho_b(k : k + N - 1)) \\
&\text{subject to} \\
&x(k + \ell + 1) = A_d x(k + \ell) + \bar{B}_d(k + \ell)\rho_b(k + \ell), \\
&u_b(k + \ell) = V_{\text{n}}(i_L(k + \ell))\rho_b(k + \ell) \in \mathcal{U}_b(k + \ell), \\
&\forall \ell = \{0, \cdots, N - 1\},
\end{aligned}
\tag{P-IV}
$$

with optimization variables $x(k + \ell)$ and $\rho_b(k + \ell)$. This problem is solved in the MPC framework to find the balancing control $u_b(k)$ at each time step $k \in \{0, \cdots, N_d - 1\}$. Here N_d is the driving horizon, $N \ll N_d$ is the prediction horizon, and $\mathcal{U}_b$, defined in (6.11), is the time-varying balancing control constraint set. The voltage control $u_v(k + \ell)$ needed for solving the problem (P-IV) is computed using analytical solution (6.9). Note that the full state and the load current are assumed to be perfectly available at current time step k. Therefore, the information needed to solve the problem is completely accessible if 1-step ahead prediction ($N = 1$) is used. The future load demand $i_L(k + \ell)$ over a short horizon ($N > 1$) is also assumed to be perfectly known in this study.

6.2.4 Summary of MPC Algorithm

The proposed control method for a given demand (i_L, v_{Ld}) and state $x(k)$ is summarized as Algorithm 2, where the UPC mode becomes a special case of BPC by presetting $u^- = 0$ in this algorithm. The complete control block diagram is shown in Figure 6.1.

Algorithm 2 Constrained LQ MPC

1: **Data**: Battery state $x(k)$ and load demand (v_{Ld}, i_L)
2: **for** $k = 1$ to N_d **do**
3: Compute $u_v(k)$ using (6.9)
4: Compute $\rho_b(k)$ by solving (P-IV)
5: Compute $u_b(k)$ using (6.10)
6: Compute $u(k) = u_v(k) + u_b(k)$
7: Apply $u(k)$ to the modular battery system
8: **end for**

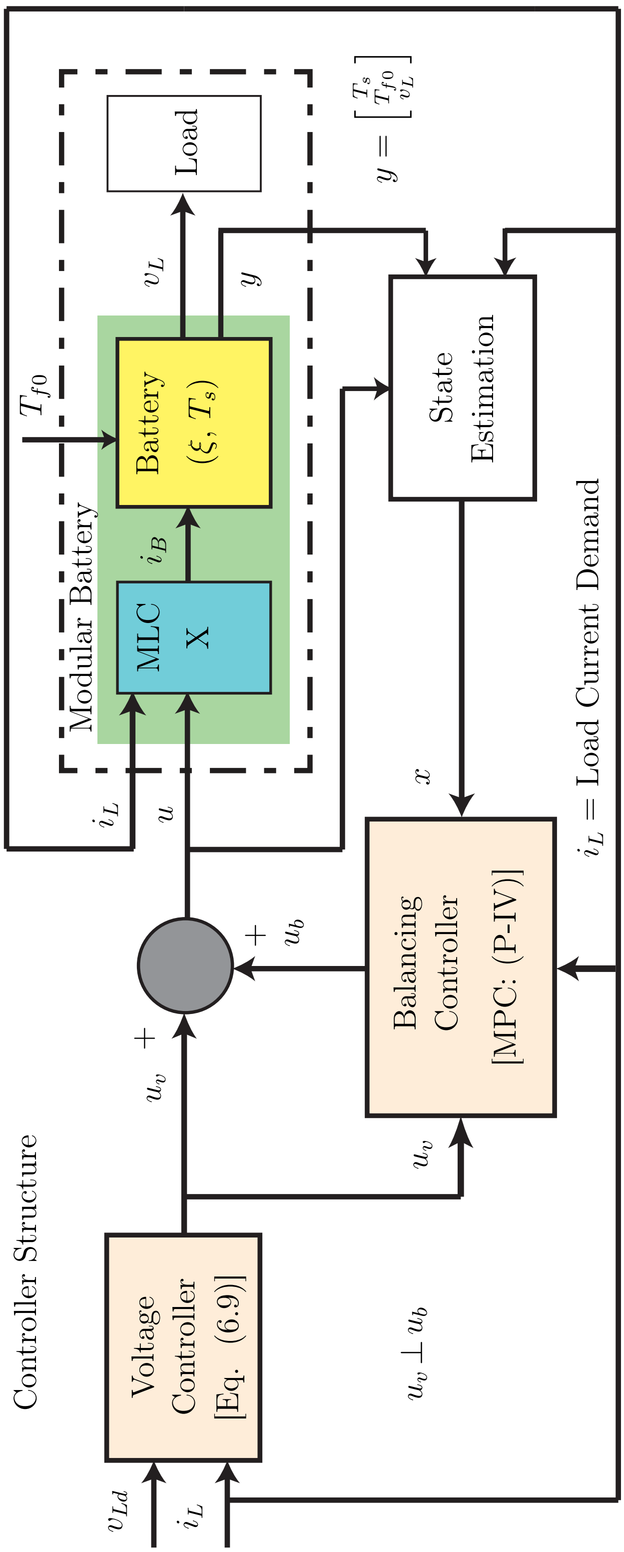

Figure 6.1: Block diagram of closed-loop control system of MLC-based modular battery powering a variable load.

6.3 Controller Analysis

6.3.1 Control Structure

The closed-loop control system for battery load management, using voltage controller (6.9) and balancing controller (P-IV), is shown in Figure 6.1. The balancing control law in general is a piecewise-affine feedback in x. However, when constraints are inactive, it has a simple linear time-varying feedback structure given by

$$u_b^u(k) = K_{u_b}^e(i_L(k))\xi(k) + K_{u_b}^\vartheta(i_L(k))\vartheta(k), \tag{6.15}$$

where $K_{u_b}^e$ is a SOC control gain matrix and $K_{u_b}^\vartheta = \begin{bmatrix} K_{u_b}^t & K_{u_b}^f \end{bmatrix}$ is a thermal control gain matrix where $K_{u_b}^t$ is a gain matrix for temperature control and $K_{u_b}^f$ is a gain vector for compensation of inlet fluid temperature. The gain matrices $K_{u_b}^e$ and $K_{u_b}^\vartheta$ have a special structure, which is investigated in detail in Chapter 8.

6.3.2 Control Interpretation

Control Corrections

The total control u and the voltage control u_v are both positively constrained. However, the balancing control u_b may attain both positive and negative values. In this context, we can interpret u_b as a *control correction term* with a possibility of both positive and negative corrections. The voltage controller first decides the duty of each cell to exactly satisfy the voltage demand without caring about balancing. The balancing controller then corrects (either increase or decrease) the duty of each cell in accordance with its balancing errors e_{ξ_i} and $e_{T_{si}}$ without disturbing the voltage.

Remark 6.1. *Note that the balancing control constraint set $\mathcal{U}_b(k)$, defined in (6.11), may be asymmetric about origin depending on the value of u_v, which depends on the ratio of battery power demand and its power capacity. Therefore, having the same range of positive and negative corrections, which is desirable for better balancing performance, may or may not be possible.*

Balancing Power Flow

The net power flow (so-called balancing power) through modular battery under u_b is zero at each time instant i.e.,

$$P_{Lb}(k) = i_L(k)v_{Lb}(k) = i_L(k)D_v(k)u_b(k) = 0, \tag{6.16}$$

where the third equality is obtained using the fact that the battery terminal voltage under u_b is zero i.e., $v_{Lb} = D_v \cdot u_b = 0$ [cf. (6.2)]. Since each dc/dc converter is assumed as a lossless switch network, the net balancing power output of all cells is also zero i.e.

$$P_{Lb}(k) = P_{Bb}(k) = \sum_{i=1}^{n} P_{Bb,i}(k) = 0, \tag{6.17}$$

where $P_{Bb,i} = P_{Lb,i} = d_{vi}^{+} i_{Bb,i}^{+} - d_{vi}^{-} i_{Bb,i}^{-}$ is the balancing power of each cell. Now defining $i_{Bb,i}^{+} = i_L u_{bi}^{+}$, $i_{Bb,i}^{-} = i_L u_{bi}^{-}$, and substituting d_{vi}^{+} and d_{vi}^{-} with (4.6), we get

$$P_{Bb}(k) = P_{Bb,g}(k) - P_{Bb,\ell}(k) \ = 0 \tag{6.18}$$

where $P_{Bb,g} = i_L \sum_{i=1}^{n} v_{oci} u_{bgi}$ is the total internal balancing power generated by total OCV source and $P_{Bb,\ell}(k) = i_L^2 \sum_{i=1}^{n} R_{ei} u_{b\ell i}$ is the total internal battery balancing power loss. Here

$$u_{bgi} = u_{bi}^{+} - u_{bi}^{-}, \quad u_{b\ell i} = u_{bi}^{+} + u_{bi}^{-}, \tag{6.19}$$

are so-called SOC and temperature balancing controls. The equation (6.18) shows that the total balancing power is zero, but $P_{Bb,g}$ and $P_{Bb,\ell}$ cannot be zero individually for nonzero u_b. Note that, depending on the sign of u_{bi}^{+}, the balancing controller can *virtually* generate both positive (generate heat) and negative losses (consume heat) in each Cell$_i$ to achieve balancing.

Average and RMS Current Corrections

The control decomposition leads to the following virtual decomposition of the average and rms cell currents,

$$I_{Bai} = f_a(i_L, u_{gi}) = I_{Bva,i} + I_{Bba,i}, \tag{6.20a}$$

$$I_{Bri}^2 = f_r(i_L, u_{\ell i}) = I_{Bvr,i}^2 + I_{Bbr,i}^2, \tag{6.20b}$$

where functions

$$f_a(i_L, u_{gi}) = \frac{1}{N_d} \sum_{k=1}^{N_d} h \cdot i_L(k) u_{gi}(k), \tag{6.21a}$$

$$f_r(i_L, u_{\ell i}) = \frac{1}{N_d} \sum_{k=1}^{N_d} h \cdot i_L^2(k) u_{\ell i}(k). \tag{6.21b}$$

Here $I_{Bva,i} = f_a(i_L, u_{vi}^{+})$ and $I_{Bvr,i}^2 = f_r(i_L, u_{vi}^{+})$ are average and rms currents under u_{vi} whereas $I_{Bba,i} = f_a(i_L, u_{bgi})$ and $I_{Bbr,i}^2 = f_r(i_L, u_{b\ell i})$ are *virtual* average and rms *current corrections* under u_{bi} (note that $I_{Bbr,i}$ is not a truly rms quantity as it can attain negative value for $u_{bi} < 0$). These variables are used to study the functional properties of the complete controller (u) as well as its each component (u_v and u_b) in Section 6.5.2.

Battery Emulation

An alternative interpretation of the balancing controller is that it forms a *time-varying virtual cell* (balancing cell) in series with *actual cell* (voltage generating cell). The time-varying electrical parameters (virtual OCV, virtual capacity, and virtual resistance) of each virtual cell are given by

$$v_{ocb,i} = v_{oci} u_{bgi}, \quad C_{eb,i} = \frac{C_{ei}}{u_{bgi}}, \quad R_{eb,i} = R_{ei} u_{b\ell i},$$

where u_{bgi} and $u_{b\ell i}$ are defined in (6.19). The above relationships can be easily verified by plugging in $u = u_v + u_b$ into the electro-thermal dynamics (4.21a) and (4.21b) of a cell. Since v_{oci}, C_{ei}, and R_{ei} are always positive, $u_{bi}^- \geq 0$, and u_{bi}^+ can attain both positive and negative values, the virtual cell parameters can also attain both positive and negative values. In other words, the balancing controller forms a virtual *positive/negative cell*, which tries to compensate the actual cell by canceling out the imbalance in capacity, resistance and voltage of the actual cell. The electrical parameters of a *compensated cell* are given by

$$v_{oci}^c = v_{oci} \left(u_{vi}^+ + u_{bgi} \right), \quad C_{ei}^c = \frac{C_{ei}}{\left(u_{vi}^+ + u_{bgi} \right)}, \quad R_{ei}^c = R_{ei} \left(u_{vi}^+ + u_{b\ell i} \right).$$

6.3.3 Sensitivity Analysis

The control design, presented in section 6.2, considers the affect of electrical actuation on temperature of cells. However, the effect of temperature on the electrical parameters of cells is neglected i.e. parameters are constant. In this section, we analyze the impact of this approximation.

An experimentally validated model for LFP cell is available in the literature, see [35–37]. According to these studies, the cell capacity and OCV have typically no short-term temperature dependence. However, the cell resistance (consequently the terminal voltage) varies as a function of temperature as shown in Figure 6.2. We identified this curve through piecewise affine (PWA) approximation between consecutive data points obtained from the experimentally validated model. As we can see, the cell resistance varies slowly as a function of temperature in normal operating range $[25, 40]$°C. Therefore, we can design the controller assuming cell resistance to be constant for small temperature variation. The balancing controller uses state feedback and its objective is not to achieve zero steady-state errors. Therefore, it is inherently robust to small resistance variation as shown through simulations in section 6.5.5. The variation in resistances over large temperature range can be compensated using gain-scheduling at much slower rate.

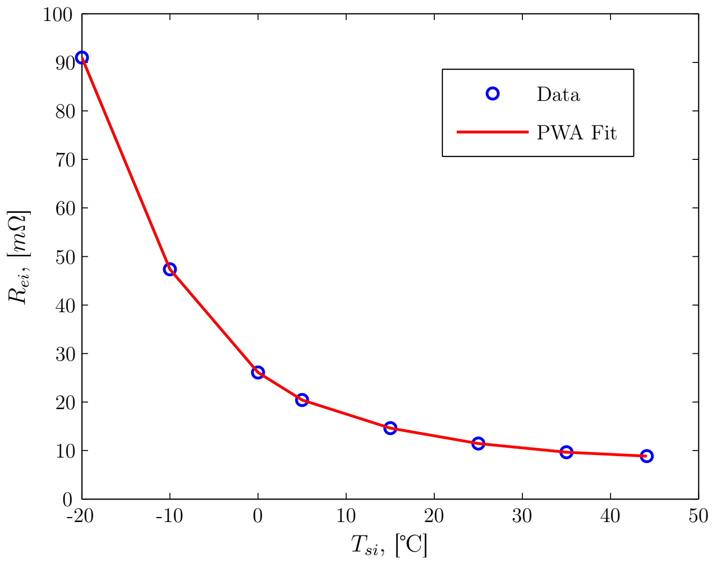

Figure 6.2: Cell resistance variation as a function of temperature.

However, the voltage controller uses only feedforward information to achieve voltage tracking. Therefore, we analyze the sensitivity of terminal voltage v_L to small resistance variation around its nominal value as follows. Let us first rewrite

$$v_{La} = D_v u = v_{oc}^{\mathrm{T}} u_g - i_L R_e^{\mathrm{T}} u_\ell, \tag{6.23}$$

where $u_g = [u_{gi}] \in \mathbb{R}^n$ (see (4.11) for u_{gi}), $u_\ell = [u_{\ell i}] \in \mathbb{R}^n$ (see (4.12) for $u_{\ell i}$), $v_{oc} = [v_{oci}] \in \mathbb{R}^n$, and $R_e = [R_{ei}] \in \mathbb{R}^n$. Defining $R_{eB} = R_e^{\mathrm{T}} u_\ell \in \mathbb{R}_+$ as total instantaneous resistance of modular battery, we get

$$v_L = v_{oc}^{\mathrm{T}} u - i_L R_{eB} \quad \Rightarrow \quad \partial v_L = -i_L \partial R_{eB}.$$

For a meaningful relation, let us define $\partial R_{eB} = p_R R_{eB}^\star$ and $\partial v_L = p_v v_L^\star$, where $R_{eB}^\star$ and $v_L^\star = v_{Ld}$ are nominal battery resistance and voltage, and p_R and p_v are relative/percentage variations in battery resistance and voltage. Now we can write

$$p_v = -\left(\frac{i_L R_{eB}^\star}{v_{Ld}}\right) p_R = -\left(\frac{V_{B\ell}^\star}{v_{Ld}}\right) p_R,$$

where $V_{B\ell}^\star = i_L R_{eB}^\star$ is the nominal battery voltage loss. Now using $(1-\eta_B) \approx V_{B\ell}^\star / v_{Ld}$ as a sensitivity function, we get

$$p_v \approx -\left(1 - \eta_B\right) p_R, \tag{6.24}$$

where η_B is the battery efficiency. Since $\eta_B \geq 0.9$ normally, we have $p_v \approx -0.1 p_R$. This simple analysis predicts very small error in v_L for small variation in R_{eB}. We verify this through simulations in section 6.5.5.

6.4 Simulation Results: UPC versus BPC

The MPC Algorithm 2 is tested through simulations for both UPC and BPC modes. This control Algorithm is based on analytical solution (6.9) of problem (P-II) and numerical solution of problem (P-IV). To solve problem (P-IV), we used SeDuMi solver in `CVX` [95]. The controller in both UPC and BPC modes has been tuned using first Bryson's rule [94, pg.537] and then iterative trial and error method to achieve satisfactory balancing performance ($\|e_\xi\|_\infty \leq 2.5\%$, $\|e_{T_s}\|_\infty \leq 1$°C) within reasonable time with short prediction horizon N for various drive cycles. For all tested drive cycles, $N = 1$ gives satisfactory controller performance. Longer prediction horizons ($N = 5$ to 60) improves SOC balancing performance especially in cases of aggressive driving. In this section, the performance of UPC and BPC is thoroughly compared only for the most realistic case $N = 1$ (i.e. information about future load demand is not used). The detailed analysis of UPC mode is presented separately in the next section. The simulation setup and results are discussed below.

6.4.1 Simulation Setup

Battery Configuration and Load Profile

The battery setup is the same as described in section 5.2 except the drive cycles. Here, for thorough performance comparison between UPC and BPC, we consider two trips of US06 and constant motorway driving cycles, where each trip is followed by a constant charging at $4c$ to bring the battery to its initial condition. These two drive cycles are representative of aggressive driving behavior and may be challenging for achieving simultaneous thermal and SOC balancing using UPC. In particular, the constant high speed motorway driving is considered for thorough evaluation of balancing performance under most unfavorable condition i.e. *little load current variation* during driving. The demanded battery load current i_L (in c-rate) and its histogram for both drive cycles are shown in Figure 6.3. The demanded battery load voltage v_{Ld} is assumed as a constant dc-link voltage of a three-phase two-level inverter. It is chosen as $9.25\,V$ to ensure condition (6.8), at each time instant of both drive cycles, for the 4 cell modular battery.

Battery Performance Variables for Comparison

In addition to $\|e_\xi(k)\|_\infty$ and $\|e_{T_s}(k)\|_\infty$, which measure the balancing performance as defined in section 5.2, we introduce some new variables enlisted in Table 6.1 to compare battery performance under UDO, UPC, and BPC

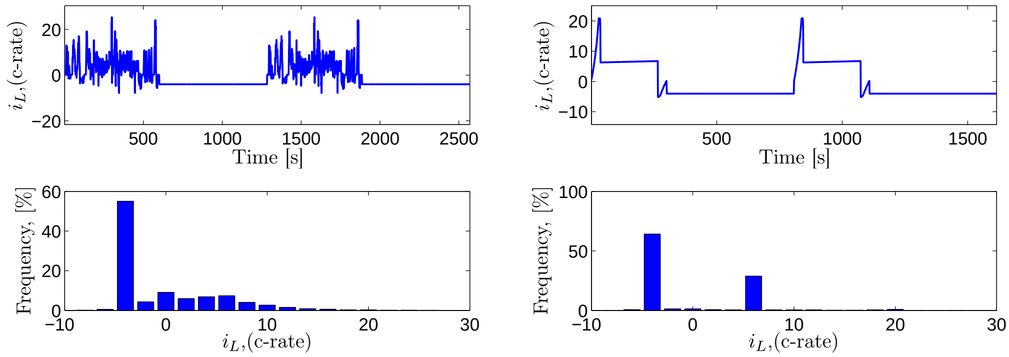

(a) Current for *US06*.

(b) Current for *constant 80mph*.

Figure 6.3: Simulated load current and the histogram for two trips of US06 and constant 80 mph drive cycle along with $4\,c$ charging after each trip.

modes. We also compare these modes in terms of effective battery capacity C_{B} (given by (2.9) for UDO and (2.14) for UPC and BPC), SOC ξ_{B} (given by (2.10) for UDO and (2.14) for UPC and BPC), energy losses $E_{Bl,\mathrm{tot}}$, and so-called local and mean efficiencies given by

$$\eta_B(k) = \begin{cases} \dfrac{P_B(k)}{P_{Bg}(k)}, & i_L(k) > 0 \\ \dfrac{P_{Bg}(k)}{P_B(k)}, & i_L(k) < 0 \end{cases} \tag{6.25}$$

$$\bar{\eta}_B = m_{\eta_B} \tag{6.26}$$

where variables P_B and P_{Bg} are defined in Table 6.1 and m_{η_B} denotes mean of $\{\eta_B(k)\}_{k=1}^{N_d}$. Table 6.1 also enlists some other variables for performance comparison.

6.4.2 Performance Comparison: US06 Driving

The balancing performance of UPC and BPC modes of the modular battery has been thoroughly evaluated and compared in simulations. The simulation results for two driving trips of US06 are shown in Figure 6.4. The plots are arranged in a 3×4 matrix of subfigures where rows 2 and 3 correspond to UPC and BPC respectively and each column corresponds to one of four battery performance variables: $v_{La}(k), \xi(k), T_s(k)$, and $\{\|e_\xi(k)\|_\infty, \|e_{T_s}(k)\|_\infty\}$. The performance under UDO (uniform duty operation of a conventional battery, see Figure 1.1) is shown in row 1 for reference purpose. These plots clearly show that both UPC and BPC significantly reduce SOC deviation among cells relative to the initial condition. Initially, the SOC balancing error monotonically decreases almost all the time under both control modes

Table 6.1: Definition of performance variables

Battery Variables	**Description**
$m_{\\|e_\xi\\|_\infty}$	Mean SOC deviation *over drive cycle*
$\sigma_{\\|e_\xi\\|_\infty}$	Std. Dev. of SOC deviation —"—
$m_{\\|e_{T_s}\\|_\infty}$	Mean temp. deviation —"—
$\sigma_{\\|e_{T_s}\\|_\infty}$	Std. Dev. of temp. deviation —"—
$m_{T_{s,\text{high}}}$	Mean of highest cell temp. —"—
$\sigma_{T_{s,\text{high}}}$	Std. Dev. of highest cell temp. —"—
$T_{s,\text{peak}} = \max\{T_s(k)\}_{k=1}^{N_d}$	Peak cell temp. —"—
$m_{T_B} = \dfrac{1}{N_d}\sum_{k=1}^{N_d} \bar{T}_s(k)$	Mean battery temp. —"—
$E_{Bl,\text{tot}} = \sum_{k=1}^{N_d} h \cdot P_{Bl}(k)$	Energy lost —"—
$\bar{\eta}_B = \frac{1}{N_d}\sum_{k=1}^{N_d} \eta_B(k)$	Mean battery efficiency —"—
C_B (defined in (2.9) and (2.14))	Charge capacity of modular battery
T_b^e ($\\|e_\xi(k)\\|_\infty \leq 2.5\%$, $\forall k \geq T_b^e$)	SOC balancing time (error settling time)
T_b^t ($\\|e_{T_s}(k)\\|_\infty \leq 1℃$, $\forall k \geq T_b^t$)	Thermal balancing time (—"—)
$P_{Bg}(k) = \sum_{i=1}^{n} v_{oci} \cdot i_{Bai}$	Instant. internal power generated
$P_{Bl}(k) = \sum_{i=1}^{n} R_{ei} \cdot i_{Bri}^2$	Instant. power lost
$P_B(k) = P_{Bg}(k) - P_{Bl}(k)$	Terminal power delivered/absorbed
$\bar{T}_s(k) = \dfrac{1}{n} 1_n^{\mathrm{T}} T_s(k)$	Mean of instant. cell temperatures
$T_{s,\text{high}}(k) = \max\{T_s(k)\}$	Highest instant. cell temperature

as shown in Figures 6.4(h) and 6.4(l). The BPC achieves $\|e_\xi(k)\|_\infty \leq 2.5\%$ before UPC. However, after decay of the initial error, both control modes are able to keep tight SOC equalization during both charging and discharging. In addition, the temperature deviation under two control modes is significantly lower than that under UDO during whole driving despite significant deviation among cell resistances and intensive loading. It remains within 1°C after decay of initial SOC imbalance. This balancing performance is accomplished while simultaneously achieving exact voltage regulation ($v_{La} = v_{Ld}$) as shown in the first column of the figure.

The performance statistics are summarized in Table 6.2. The peak cell temperature $T_{s,\text{peak}}$ and mean of highest cell temperature $m_{T_{s,\text{high}}}$ during whole driving under BPC are considerably less than that under UDO. Therefore, BPC-based modular battery may have longer lifetime than the conventional battery in which unequal cells are equally loaded. The BPC also outperforms UPC in terms of the balancing speed by significant margin. However, it is only marginally better than UPC in terms of mean and standard deviation of balancing errors. In addition, the improvement in the balancing speed and performance variance comes at the cost of some extra energy losses, slightly reduced efficiency (0.22% less), and small increase in battery temperature compared to UPC. Since capacity fading is exponential in cell temperature [see the cycle-life model (2.2)], even a small temperature increase over long term under BPC may affect the battery lifetime. Moreover, the BPC-based modular battery requires 2 extra switches inside each module. Therefore, the UPC-based modular battery is a more cost and energy efficient solution without any significant compromise on balancing performance for US06 type driving.

Table 6.2: Performance comparison under US06 driving

Variables	**UDO**	**UPC**	**BPC**
$m_{\|e_\xi\|_\infty}$	6.2%	0.37%	0.24%
$\sigma_{\|e_\xi\|_\infty}$	1.0%	0.16%	0.05%
$m_{\|e_{T_s}\|_\infty}$	1.00°C	0.52°C	0.36°C
$\sigma_{\|e_{T_s}\|_\infty}$	0.33°C	0.06°C	0.04°C
$m_{T_{s,\text{high}}}$	30.76°C	30.17°C	30.35°C
$\sigma_{T_{s,\text{high}}}$	2.02°C	1.70°C	1.76°C
$T_{s,\text{peak}}$	34.9°C	33.6°C	33.8°C
m_{T_B}	29.82°C	29.77°C	30.06°C
$E_{Bl,\text{tot}}$	4.59 Wh	4.53 Wh	4.81 Wh
$\bar{\eta}_B$	95.70%	95.74%	95.48%
C_B	1.91 Ah	2.16 Ah	2.16 Ah
T_b^e	–	152 s	108 s
T_b^t	–	418 s	220 s

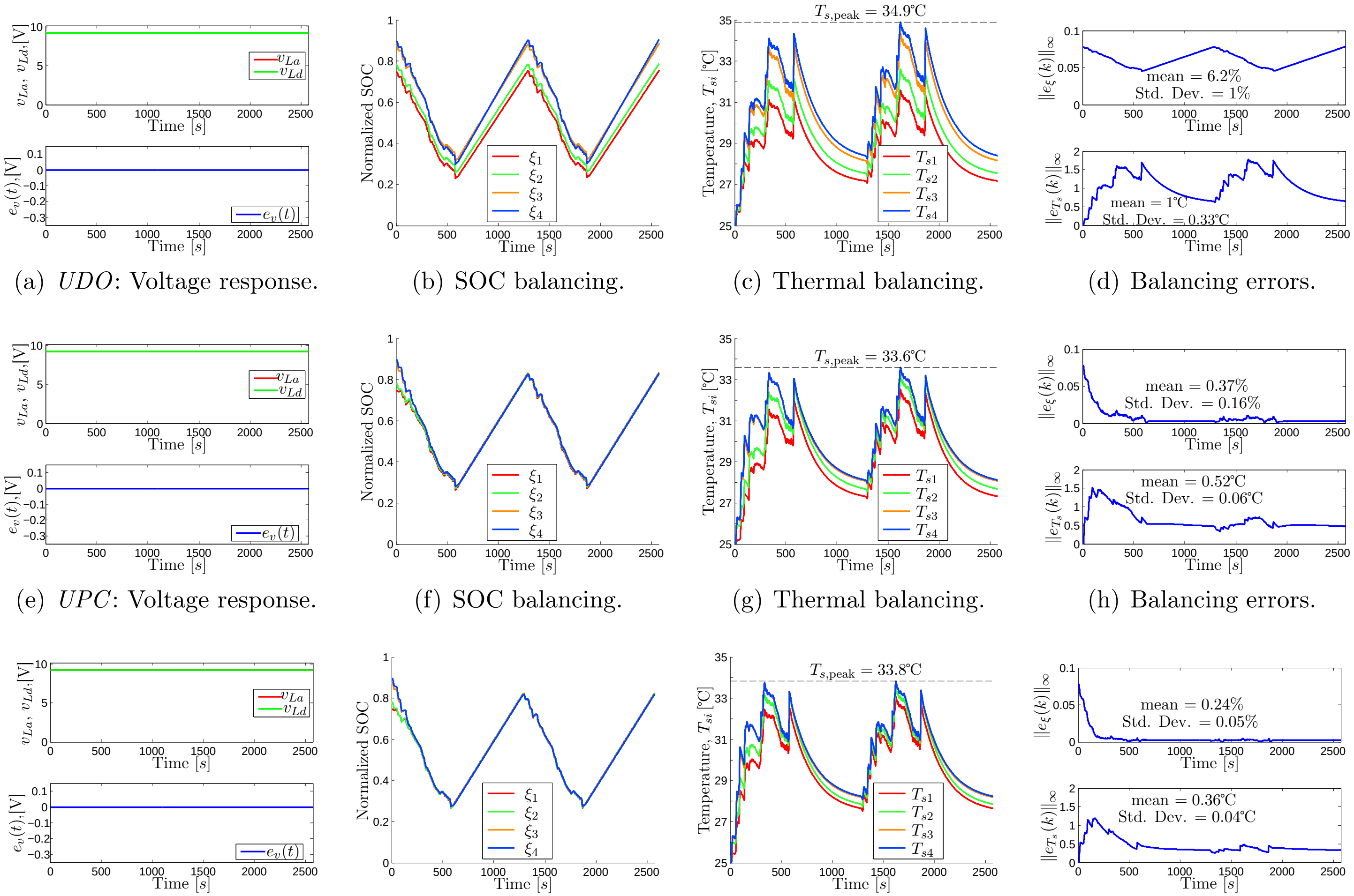

(a) *UDO*: Voltage response. (b) SOC balancing. (c) Thermal balancing. (d) Balancing errors.

(e) *UPC*: Voltage response. (f) SOC balancing. (g) Thermal balancing. (h) Balancing errors.

(i) *BPC*: Voltage response. (j) SOC balancing. (k) Thermal balancing. (l) Balancing errors.

Figure 6.4: Performance comparison under *US06 drive cycle*: *Uniform Duty Operation (UDO)*: first row; *Unipolar Control mode (UPC)*: second row; and *Bipolar Control mode (BPC)*: third row.

6.4.3 Bipolar Control Behavior

The control actuations under UPC and BPC are shown in Figure 6.5. The plots are arranged in a 2×2 matrix of subfigures where the first and second columns correspond to control variables under UPC and BPC respectively. The positive and negative control actions (u_i^+ and u_i^-) are displayed in first and second rows respectively. Figure 6.5(d) shows that negative control is only slightly engaged by BPC mode to compensate for capacity imbalance. In particular, cells 1 and 2 get some level of negative actuation due to their lower initial dischargeable capacities. The cells 3 and 4 are not negatively actuated as it is not optimal due to their higher resistances. Note that the negative actuation of cells 1 and 2 during driving also reduces after decay of initial SOC imbalance.

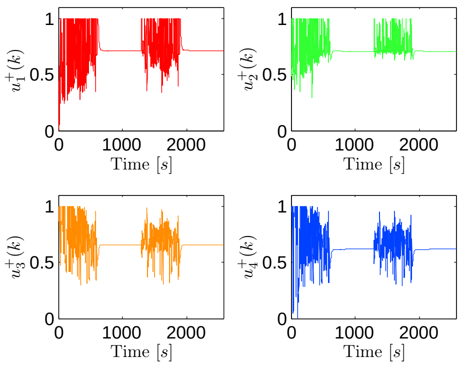

(a) *UPC:* Positive cell actuations.

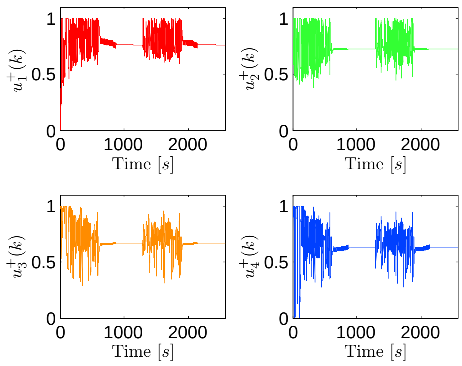

(b) *BPC:* Positive cell actuations.

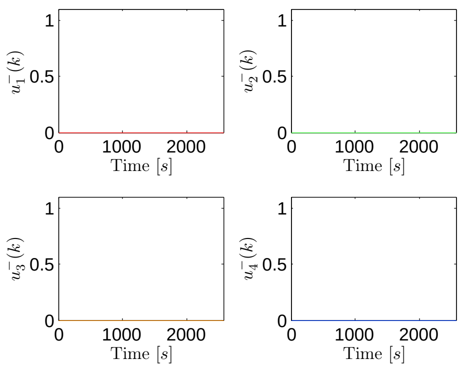

(c) *UPC:* Negative cell actuations.

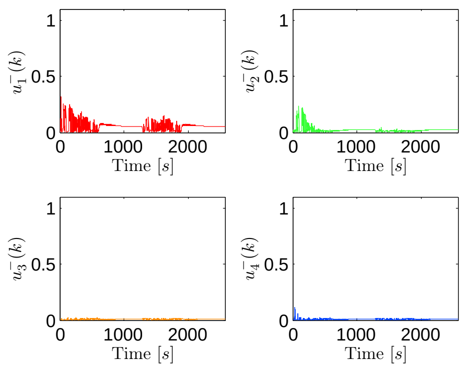

(d) *BPC:* Negative cell actuations.

Figure 6.5: Control behavior comparison under UPC and BPC modes. The figure displays both positive actuation (discharging) and negative actuation (charging) of cells. Figure 6.5(d) shows that negative control is only engaged slightly by BPC to compensate for capacity imbalance.

6.4.4 Performance Comparison: Motorway Driving

The simulation results are shown in Figure 6.6. It is clear from Figure 6.6(d) that for constant high load current, the UPC mode struggles to achieve simultaneous thermal and SOC balancing *during first trip*. It is mainly due to *one-to-one coupling* between average and rms cell currents under constant loads for UPC [see Remark 4.1 and Fig. 4.2(c)]. However, during charging after first driving trip, the UPC is able to improve balancing performance. The reversal of current direction plays a main role in this because cells with higher dischargeable (lower chargeable) capacity and higher resistance can now be used less during charging. Moreover, the decrease in current magnitude during charging is also favorable for SOC balancing due to reduced thermal intensity. Nevertheless, the cells (fairly balanced in SOC by the end of charging phase) start deviating again slightly during next driving trip. On the other hand, the BPC shows good thermal and SOC balancing performance independent of current reversal as shown in third row. It is mainly due to relatively *loose coupling* between average and rms cell currents for BPC mode under constant loads [see Remark 4.1 and Fig. 4.2(f)].

The performance statistics are given in Table 6.3. The BPC balancing performance is quite consistent in terms of mean and standard deviation of balancing errors, but the UPC performance has degraded in this regard relative to that under US06 (compare first four entries of tables 6.2 and 6.3). However, the better balancing performance under BPC comes at the cost of two extra switches per module and some extra energy losses (efficiency reduced by 0.40%), which over long term may reduce battery life-time. Moreover, the BPC gives significant benefit in SOC balancing particularly during first driving trip, but this benefit is only marginal after start of external charging phase. In addition, the UPC performs significantly better than UDO in terms of all statistics. Therefore, the UPC-based modular battery is still an acceptable solution.

Table 6.3: Performance comparison under motorway driving

Variables	**UDO**	**UPC**	**BPC**
$m_{\Vert e_\xi \Vert_\infty}$	6.61%	0.52%	0.27%
$\sigma_{\Vert e_\xi \Vert_\infty}$	0.74%	0.28%	0.06%
$m_{\Vert e_{T_s} \Vert_\infty}$	1.11℃	0.69℃	0.40℃
$\sigma_{\Vert e_{T_s} \Vert_\infty}$	0.38℃	0.15℃	0.07℃
$m_{T_{s,\text{high}}}$	31.00℃	30.64℃	30.88℃
$\sigma_{T_{s,\text{high}}}$	2.02℃	1.92℃	2.00℃
$T_{s,\text{peak}}$	34.28℃	33.38℃	33.61℃
m_{T_B}	30.00℃	29.97℃	30.46℃
$E_{Bl,\text{tot}}$	3.10 Wh	3.07 Wh	3.36 Wh
$\bar{\eta}_B$	95.10%	95.13%	94.75%
C_B	1.91 Ah	2.16 Ah	2.16 Ah
T_b^e	–	76 s	72 s
T_b^t	–	356 s	270 s

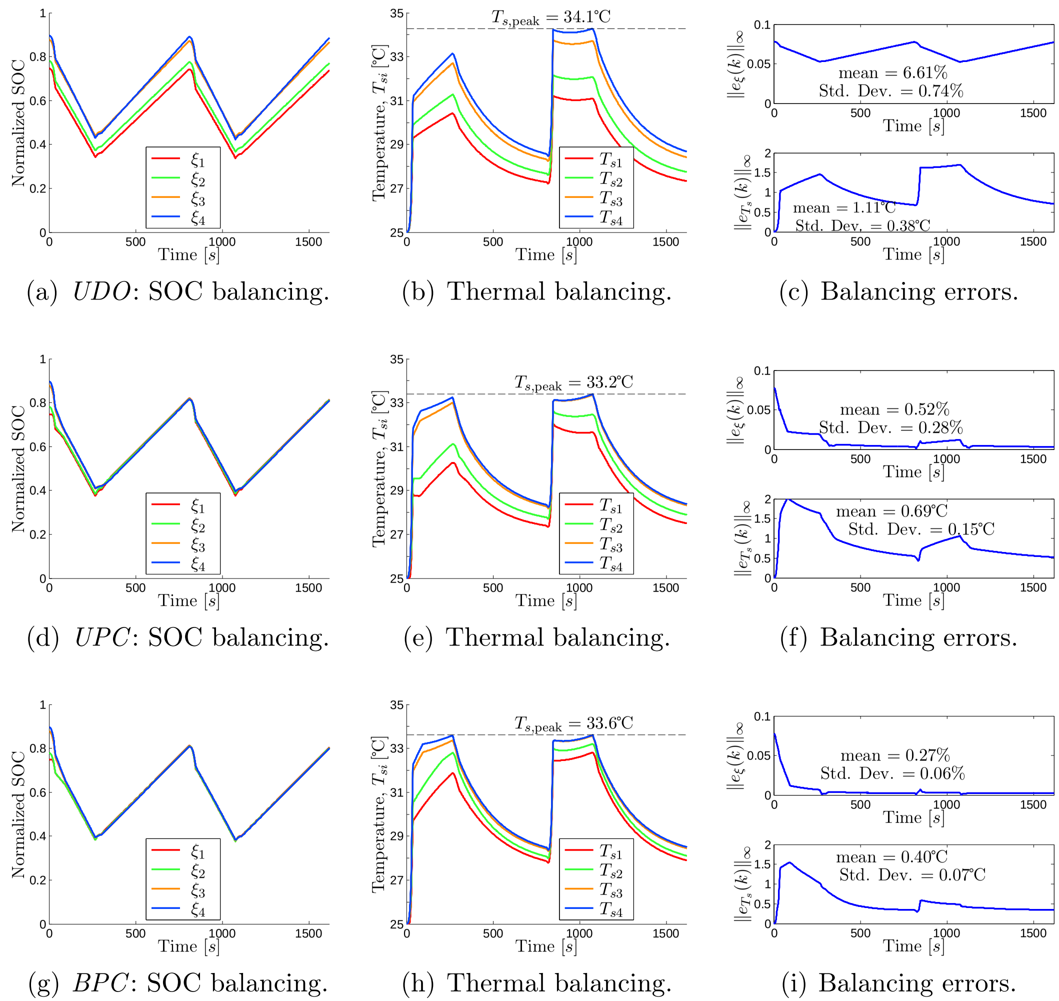

(a) *UDO*: SOC balancing. (b) Thermal balancing. (c) Balancing errors.

(d) *UPC*: SOC balancing. (e) Thermal balancing. (f) Balancing errors.

(g) *BPC*: SOC balancing. (h) Thermal balancing. (i) Balancing errors.

Figure 6.6: Performance comparison under *Constant Speed Motorway drive cycle*: *Uniform Duty Operation (UDO)*: first row; *Unipolar Control mode (UPC)*: second row; and *Bipolar Control mode (BPC)*: third row.

6.4.5 Summary

In this section, the performance comparison between UPC and BPC modes of the modular battery has been shown for US06 and constant 80 mph motorway driving cycles, as these are challenging for balancing. The results show that BPC gives more consistent balancing performance than UPC. It is self-reliant as its performance is independent of exogenous factors like variation in *magnitude* and *direction* of load current. This becomes possible due to the feasibility of negative cell actuations, which results in loose coupling between average and rms values of cell current. Therefore, we get extra freedom in controlling temperature and SOC. On the other hand, the UPC struggles without variation in current magnitude, resulting in slightly higher variance in performance than that under BPC. It struggles particularly under constantly high load current. However, if we look at full charge/discharge cycle, then there is only a marginal difference in performance. This is due to reversal of current direction during charging phase, which facilitates the balancing task for UPC.

The better balancing performance of BPC comes at the cost of slightly reduced battery efficiency due to extra losses during negative actuation of cells, which increases battery temperature. Although the temperature rise is small, it is better to avoid it because cell ageing is exponential in temperature. The BPC mode also needs $2n$ (n = no. of modules) extra switches, which implies higher cost and semiconductor losses. In addition, the balancing performance of UPC does not degrade drastically if external charging can be provided after each short driving trip, which is possible at least for EV and PHEV applications. Therefore, looking over multiple charge/discharge cycles in such applications, the UPC mode is a more cost-effective solution without any significant compromise on balancing performance. The BPC, on the other hand, may show some merit particularly in applications, which require high load current pulses of long duration and have no dedicated external charging as in HEVs.

6.5 UPC Mode: Detailed Analysis

In this section, the UPC mode is studied in more detail to analyze the control performance under different driving styles, control behavior, control robustness, and the effect of prediction horizon. This analysis is particularly done for three drive cycles (presented in section 5.2.3) without assuming any dedicated external charging phase except regenerations. The simulation setup is the same as described in section 5.2. The controller has been tuned to achieve $\|e_\xi\|_\infty \leq 2.5\%$ within reasonable time while keeping $\|e_{T_s}\|_\infty \leq 1$℃ all the time for all three drive cycles using prediction horizon $N = 1 - 60$.

6.5.1 One-Step MPC: Impact of Driving on Balancing

The balancing performance of the aged modular battery using ideal 1-step MPC (no parametric uncertainty) has been thoroughly investigated. The simulation results are shown in Figure 6.7 for all three drive cycles. These plots are arranged in a 3×4 matrix of subfigures where each row corresponds to one of three drive cycles (SCM17kmA6, ARTEMIS Rural, and US06) and each column corresponds to one of four battery performance variables: $v_{La}(k), \xi(k), T_s(k)$, and $\{\|e_\xi(k)\|_\infty, \|e_{T_s}(k)\|_\infty\}$. These plots clearly show that with passage of time, SOC deviation among cells is significantly reduced relative to the initial level of deviations. Similarly, temperature deviation stays within specified limits during whole driving. The controller particularly exhibits good thermal and SOC balancing performance for both SCM17kmA6 and ARTEMIS driving cycles as shown in first two rows. This is because the load current distribution of these two drive cycles is dominated by low to medium c-rates as shown in figures 5.2(a) and 5.2(b).

The performance under US06 is not as good as for the other drive cycles. The SOC deviation, as shown in Figure 6.7(l), is nondecreasing during various intervals. It is primarily due to frequent aggressive acceleration, braking, and long phases of high speed driving during this cycle, which results in the load distribution dominated by high c-rates [see Figure 5.2(c)]. During such intensive loading, the controller prioritizes thermal balancing to secure high resistance cells from thermal runaway. Therefore, the controller particularly struggles with SOC balancing during each intensive driving phase. However, the overall performance is still satisfactory as the maximum SOC balancing error has reduced from initial level of 7.8% to the level of 2.5% at final time and the maximum temperature deviation has remained within 1 ℃ over whole driving cycle. Also, compare this performance with the benchmark performance under GOC shown in Figure 5.3. There is no significant difference in thermal balancing performance, although the SOC balancing performance is improved using full future load information ($N = N_d$).

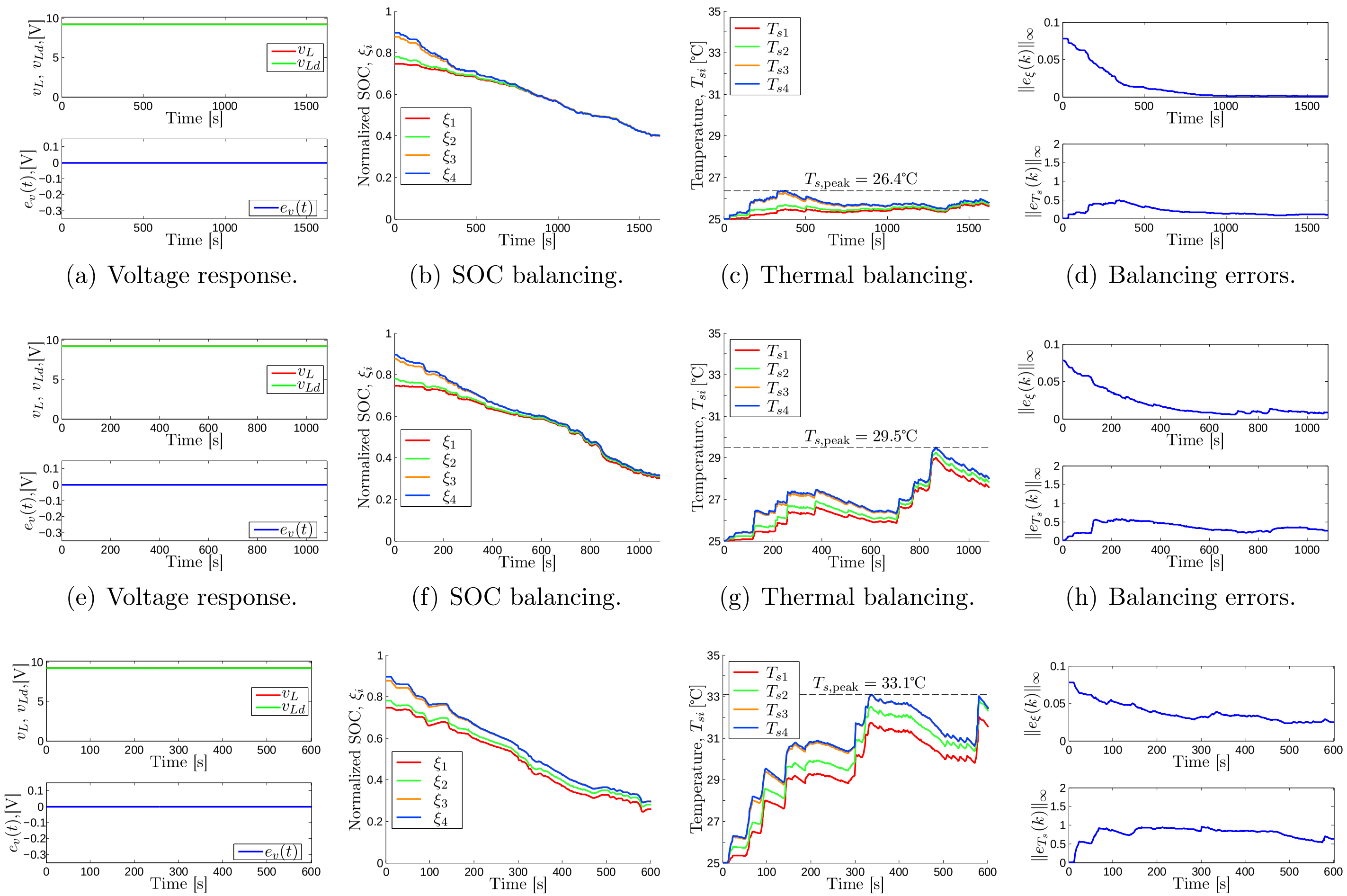

(a) Voltage response. (b) SOC balancing. (c) Thermal balancing. (d) Balancing errors.

(e) Voltage response. (f) SOC balancing. (g) Thermal balancing. (h) Balancing errors.

(i) Voltage response. (j) SOC balancing. (k) Thermal balancing. (l) Balancing errors.

Figure 6.7: Simulation results for 1-step MPC control performance under three drive cycles is shown: *SCM17kmA6*: first row; *ARTEMIS Rural*: second row; and *US06*: third row.

6.5.2 Control Behavior and Analysis

To understand how the controller achieves the balancing, the various functional aspects of balancing controller are discussed below in detail.

Balancing Controller: Charge and Heat Shuffler

Figure 6.8 shows bar plots of average and rms currents, defined in (6.20a) and (6.20b), of each cell computed separately under voltage control, balancing control, and total control trajectories over whole drive cycle[3]. The figure is a 2×3 matrix of subfigures where the first and second rows correspond to average and rms currents respectively. Three columns corresponds to currents under u_v, u_b, and u respectively. The results are presented here for ARTEMIS only as one case-study is sufficient for current purpose.

The voltage controller decides almost equal average current (or power) for each cell as shown in Figure 6.8(a). This is of course not optimal as cells have different dischargeable capacities as shown in Figure 5.1(a). Therefore, the balancing controller performs corrective action in average currents as shown in Figure 6.8(b). In a nutshell, the controller achieves SOC balance by taking out electric charge from cells with higher dischargeable capacities (Cell_3 and Cell_4) and delivering it to cells with lower dischargeable capacities (Cell_1 and Cell_2). Note that after *shuffling of charges*, the average current distribution now resembles the dischargeable capacity distribution [compare Figure 6.8(c) with 5.1(a)].

Similarly, the voltage controller decides almost equal level of rms current for all cells as shown in Figure 6.8(d). This is again not optimal as cells have different resistances as shown in Figure 5.1(b). The balancing controller in this case performs corrective action in rms current as shown in Figure 6.8(e). In a nutshell, the controller achieves thermal balancing by (virtually) taking out heat from cells with higher resistances (Cell_3 and Cell_4) and delivering it to cells with lower resistances (Cell_1 and Cell_2). Note that after *shuffling of losses*, the rms current distribution resembles the mirror image of resistance distribution [compare Fig. 6.8(f) with 5.1(b)].

In the light of above discussion, it is now quite obvious that the *balancing controller emulates a charge and heat shuffler/corrector*. It slightly shuffles/corrects cell charges and power losses to achieve SOC and thermal balancing objectives simultaneously. It is also noteworthy that balancing is achieved with *small corrections* indeed ($< \pm 10\%$ of maximum average and rms currents, [see figures 6.8(b) and 6.8(e)]), where the corrections in rms currents are opposite to those in average currents.

[3]Note that the currents under u_{vi} may exist in reality if the balancing function is tuned off, but currents under u_{bi} are only virtual

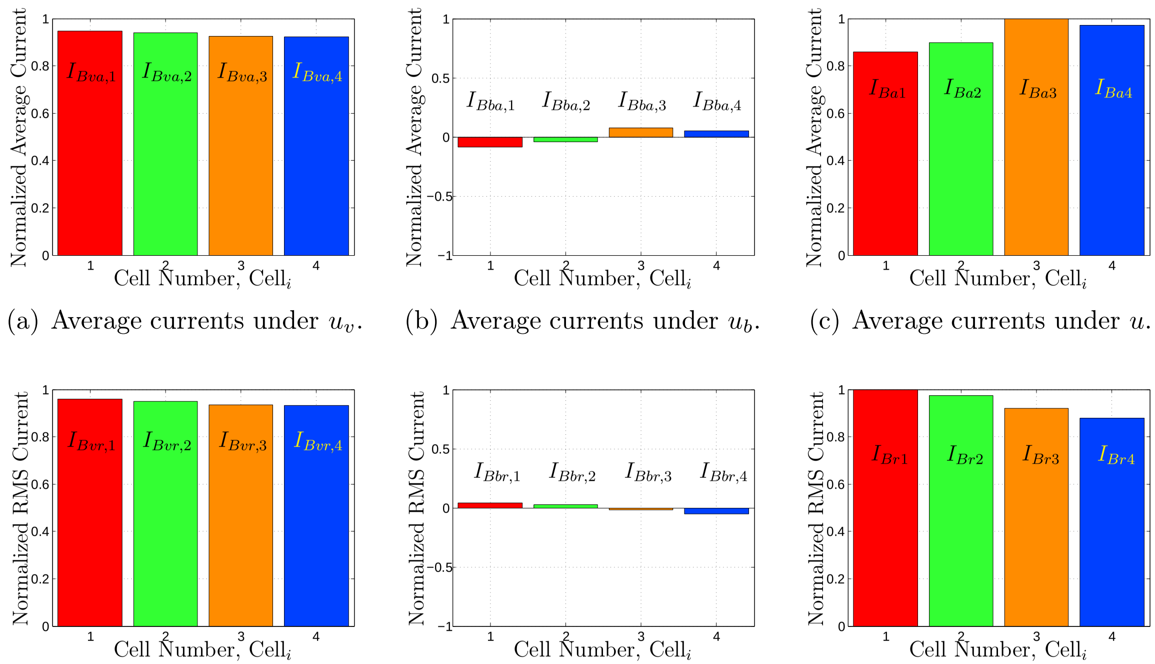

(a) Average currents under u_v.
(b) Average currents under u_b.
(c) Average currents under u.
(d) RMS currents under u_v.
(e) RMS currents under u_b.
(f) RMS currents under u.

Figure 6.8: Cell average and rms current behavior for *ARTEMIS* drive cycle under u_v, u_b, and u. Note corrective action taken by balancing controller u_b. The balancing controller slightly shuffles/corrects ($< \pm 10\%$) cell charges and heat to achieve thermal and SOC balancing simultaneously.

Balancing Controller: Virtual Power Redistributor

To understand the controller's instantaneous behavior, we study the histograms of the instantaneous terminal powers of each cell as shown in Figure 6.9. We can classify the load into various types depending on its frequency of occurrence and power level. Therefore, we can roughly say that each *power bin* in these histograms corresponds to a certain type of load. The key to achieve simultaneous thermal and SOC balancing is to optimally decide the duty of each cell in each power bin. The voltage controller unjustly decides almost identical power distribution among cells in each power bin as shown in Figure 6.9(a). The balancing controller acts as a *virtual power redistributor* to reshape the histogram of each cell as shown in Figure 6.9(b). It performs corrective actions by slightly redistributing the load on each cell according to its resistance and dischargeable capacity. For example, the balancing controller takes the following corrective actions for various types of loads:

- It shifts *infrequent high-power driving loads* (54, 72, and 90 watt power bins) to cells 1 and 2, which have lower resistances. This type of short duration high power loads result in higher rms but small average currents. Therefore, this control action saves cells 3 and 4, which have higher resistances, from faster heating and temperature deviation while securing cells 1 and 2 from faster discharge.

- It shifts more *frequent intermediate-power driving load* (18 and 36 watt bins) to cells 3 and 4, which have higher dischargeable capacities. This type of relatively long duration intermediate loads result in higher average current without significant increase in heating value of current. This particular control action saves cells 1 and 2 from faster discharging and SOC deviation while keeping temperature deviation of cells 3 and 4 within limits.

- It shifts highly *frequent low-power mixed load* (power range around zero watt) to cells 1 and 2 because this type of load contains a lot of regenerative energy, which helps cells 1 and 2 to correct their charge levels.

- It distributes the *infrequent mild-power regenerations* among all cells as per their dischargeable capacities.

- It uses cells 1 and 2 during highly *infrequent high-power regenerations.* This action saves cells 3 and 4 from extra heating and also helps in balancing SOC among cells.

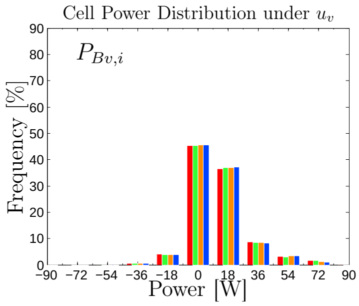

(a) Each cell power under u_v.

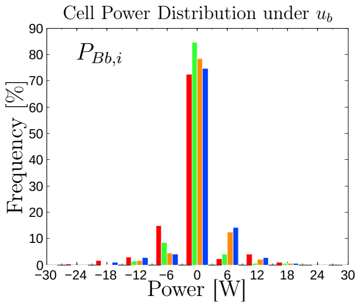

(b) Each cell power under u_b.

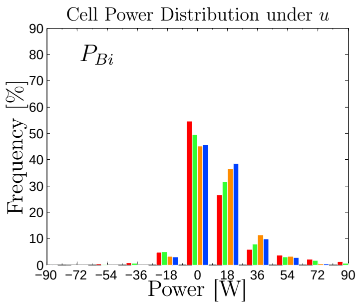

(c) Each cell power under u.

Figure 6.9: Histograms of instantaneous powers of cells for *ARTEMIS* drive cycle under u_v, u_b, and u, where each group of four bars correspond to four cells. Note that the balancing controller acts as *virtual power redistributor* to reshape the histogram of each cell in each power bin.

This set of control actions in different power bins results in different load sharing patterns for different classes of load. These nonuniform load sharing patterns enable the simultaneous thermal and SOC balancing. We can roughly say that cells 1 and 2 are used more during high-power loads and regeneration phases, whereas cells 3 and 4 are used more in low to medium driving power ranges.

Remark 6.2. *From the above discussion, it is easy to conclude that the load variations play a big role in achieving simultaneous thermal and SOC balancing under unipolar battery control mode. The difference in average and rms current distributions [compare figures 6.8(c) and 6.8(f)] is only possible due to variations in the load profile. The load variations (i.e., blend of low and high c-rates) allow somewhat independent adjustment of average and rms currents, which is a key for simultaneous SOC and thermal balancing. If the load current is continuously high (only one load type or power bin) then the simultaneous balancing is not possible because the controller can only perform one type of corrective actions in such a power bin i.e., it prioritizes thermal balancing without caring much about SOC balancing.*

6.5.3 Effect of High Initial Imbalance

The control performance for a highly unbalanced battery is shown in Figure 6.10. The simulation settings are same as before except the initial SOC imbalance, which is now 15% as shown in the figure. The large initial SOC imbalance leads to relatively large difference in initial dischargeable capacities. Despite this challenging situation, the controller is able to eventually drive SOC into the target set $\mathcal{X}_{Eg}$ ($\|e_\xi\|_\infty \leq 2.5\%$) as shown in upper subplot while keeping all temperature deviations within $\mathcal{X}_{Tg}$ ($\|e_{T_s}\|_\infty \leq 1$°C) during whole driving cycle as shown in lower subplot.

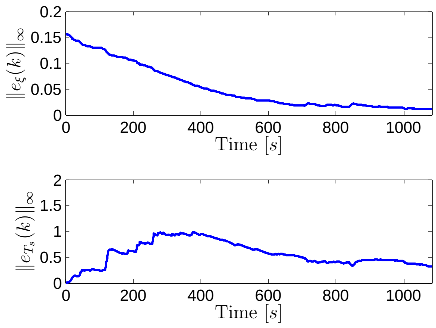

Figure 6.10: Highly Unbalanced Initial Condition: Thermal and SOC balancing performance of 1-step MPC for ARTEMIS Rural drive cycle.

6.5.4 Effect of Prediction Horizon

Now we compare the performance of 60-step and 1-step MPCs particularly for US06 as it is relatively hard to handle using 1-step MPC. The results are shown in Figure 6.11.

The SOC balancing speed has increased as shown in upper subplot of Figure 6.11. Due to faster response, there is now 1% final SOC imbalance (1.5% less compared to that with 1-step MPC). This improvement appears because the controller can now do better planning due to large accessible information about future energy flows into/out of battery pack. Depending on the direction of energy flows, cells can be both charged (increase SOC) and discharged (decrease SOC). If we know at current time that there will be a certain level of regenerative energy in near future then we can afford to discharge a certain cell more momentarily and charge it again during regeneration. Therefore, instead of instantaneous short-sighted actions, it may be beneficial to look ahead in future for upcoming regeneration phases to provide relatively better cell duty schedule for SOC balancing. This long-term planning is particularly useful for aggressive driving cycles like US06.

The thermal balancing under 60-step MPC, shown in lower subplot of Figure 6.11, has improved only slightly in terms of *mean temperature deviation* $\left(\frac{1}{N_d}\sum_{k=1}^{N_d}\|e_{T_s}(k)\|_\infty\right)$ over full drive cycle (0.71°C versus 0.77°C under 1-step MPC). The first reason is that temperature rises quickly only during intensive load demand (aggressive acceleration/braking). During these short high power pulses, the controller must take corrective action instantaneously to keep temperature deviation small. The second reason is that the energy recuperation is not beneficial for thermal balancing because cells always dissipate (never consume) heat regardless of current direction. Therefore, the long-term planning is not that crucial *directly* for thermal balancing. However, note that the faster decay of initial SOC imbalance under 60-step MPC may enable the controller to prioritize thermal balancing sooner than that under 1-step MPC. Therefore, the longer prediction horizon may also *indirectly* benefit thermal balancing, see second half of the driving in Figure 6.11.

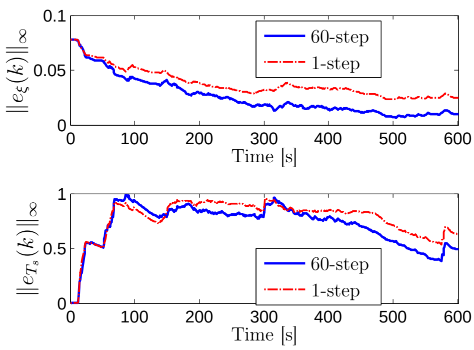

Figure 6.11: Longer Prediction Horizon: Balancing performance comparison between 60-step MPC and 1-step MPC for *US06* drive cycle.

6.5.5 Control Robustness under Model Mismatch

Now let us consider an uncertain battery model to investigate the control robustness. For this purpose, we simulate a nominal 1-step MPC (assumes only nominal cell model with constant parameters and perfectly known battery state) with the true battery that has parametric imbalance among its cells (up to 46% in cell resistance and 15% in capacity) as shown in Figure 5.1. In addition, each cell resistance also varies with temperature as shown in Figure 6.2. The simulation results for ARTEMIS drive cycle are shown in Figure 6.12. The terminal voltage error as shown in Figure 6.12(a) is very small ($<$ 3.2%) as predicted by sensitivity relation (6.24). This error can be further reduced using gain-scheduling, which would then require estimation of cell resistance. The balancing performance, shown in Figure 6.12(b), has no noticeable difference from the ideal case shown in Figure 6.7(h) (plotted here again in red) despite the large parametric uncertainty. This suggests that the controller is robust to parametric uncertainty and small resistance variation in typical operating temperature range [25, 40] °C, which is normally maintained by active cooling of batteries in xEVs. To exactly characterize the robustness property, in terms of range of parametric uncertainty and resistance variation with temperature, requires further investigation, which is beyond the scope of this study.

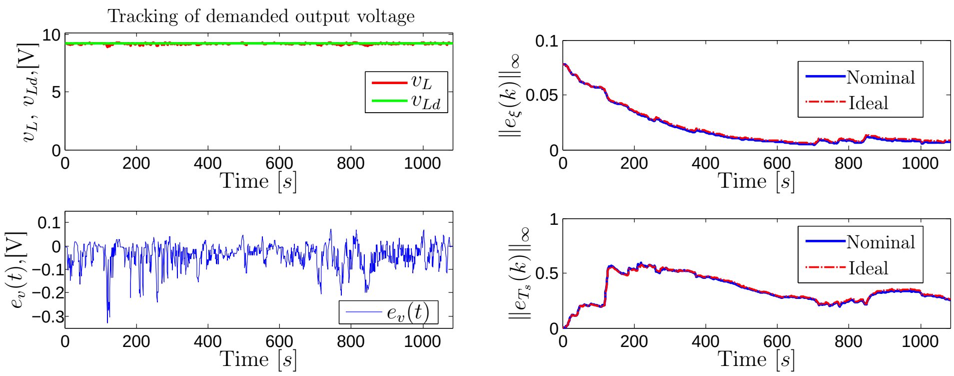

(a) Voltage response and error.

(b) Evolution of balancing errors.

Figure 6.12: Robust control performance under parametric uncertainty and resistance variation with temperature.

6.5.6 Summary

In this section, the various aspects of the proposed MPC algorithm for UPC mode of a modular battery are thoroughly evaluated. In particular, the 1-step MPC has been carefully tested to assess the balancing potential for most realistic cases where no future load information is accessible. The results have been presented for three drive cycles (real-world SCM17kmA6, ARTEMIS Rural, and US06) to analyze control performance under various driving behaviors. The results showed that it is sufficient to use 1-step MPC to achieve promising thermal and SOC balancing performance for benign to normal driving with short driving pulses (as in SCM17kmA6 and ARTEMIS Rural drive cycles). The 1-step MPC also showed good thermal balancing performance under aggressive highway driving (i.e. long driving pulses with high acceleration and speed as in US06). The SOC balancing is not as good as that under benign/normal driving, but is still acceptable. It can be further improved, if needed, by using longer prediction horizon. In short, the balancing performance highly depends on the level of load variations. Any drive cycle with long high power intervals is challenging for simultaneous thermal and SOC balancing. We have also analyzed the control behavior, which reveals the set of control actions to achieve different load sharing pattern in different load ranges. In addition, we have also analyzed the sensitivity and robustness of nominal controller to modeling uncertainty and variation of cell resistances with temperature. These variations have no noticeable effect on balancing performance and also generate negligible voltage errors.

6.6 Chapter Summary and Conclusions

The main purpose of this chapter was to devise a predictive control scheme for terminal voltage control and simultaneous thermal and SOC balancing of batteries using minimum future load information. This problem boils down to load management i.e. deciding the power flow into/out of each cell according to its state. For this, we have proposed an LQ MPC algorithm to control the modular battery in both UPC and BPC modes. The control scheme has been developed using a novel idea of orthogonal decomposition of controller into two components, one for voltage control and the other for balancing control. The voltage controller strictly satisfies the voltage demand, but distributes the power almost equally among all modules. The balancing controller achieves balancing by correcting the power distribution without disturbing the voltage. The proposed MPC scheme in both UPC and BPC modes is thoroughly evaluated under various driving behaviors. The results showed that it is sufficient to use 1-step MPC in the UPC mode to achieve promising thermal and SOC balancing performance for most common urban and rural driving situations in xEVs. The UPC struggles to some extent if battery load current is continuously staying high, but the performance is recovered if we look over multiple charge/discharge cycles.

The control performance shown by 1-step *unipolar MPC* (i.e. MPC in UPC mode) is quite encouraging for real-time control implementation. However, the experimental validation is still required for large battery packs. In addition, an appropriate module size and the extra losses due to additional electronic components (power switches and gate drivers for each module) require thorough investigation to assess the overall benefit of the modular battery. Nevertheless, the proposed MPC scheme has given us deeper insight into structural and functional properties of the simultaneous thermal and SOC balancer, which is useful for its simple rule-based implementation in the following chapters.

Chapter 7

Control Simplification 1: MPC with Projections

In the previous chapter, we concluded that it is sufficient to operate the modular battery in the UPC mode using 1-step MPC to achieve satisfactory balancing performance. This one step prediction allows simple implementation of the balancing controller, which is studied in this chapter. The aim is to compute the balancing control $u_b(k) \in \mathcal{U}_b(k)$ using a simpler approach instead of solving control constrained LQ problem at each step of MPC. We propose to compute the *balancing control policy* in receding horizon fashion based on *unconstrained LQ* problem whereas control constraint, if violated, is handled separately via projection of unconstrained control actions on control constraint set. In the following, we formulate and solve the alternative balancing control problem in detail.

7.1 Main Idea: Two-Stage Balancing Controller

We propose to solve the balancing problem (P-IV) given on page 74 in the UPC mode (only u^+ is computed i.e., $u^- = 0$)[1] for $N = 1$ in *two stages*:

1. *Unconstrained LQ Control Problem:* Firstly, we solve the unconstrained LQ problem to find balancing control policy $u_b^u = K_{u_b} x$. This policy is generated indirectly through ρ_b^u i.e. we first solve the LQ problem in terms of ρ_b^u and then, using (6.10), we get u_b^u.

2. *Constrained Control via Projection:* Secondly, we compute constrained control action by projecting $u_b^u(k)$ on the constraint set $\mathcal{U}_b(k)$.

In the following, we discuss these two stages in detail.

[1] Since the control design here is presented only for the UPC mode, we drop the superscript '+' from all control variables now onwards for notational convenience.

Balancing Control Constraint:

Since control constraint is handled separately through projections in this chapter, let us have a closer look at the balancing control polytope defined in (6.11) for better understanding of its geometrical properties. First of all, using (4.27) and (6.2) in (6.11), we redefine the time-varying balancing control constraint polytope as follows

$$\mathcal{U}_b(k) = \{u_b(k) \,|\, H_{u_b} u_b(k) \leq b_{u_b}(k),\; D_v(k)u_b(k) = 0\} \subseteq \mathcal{N}(D_v), \tag{7.1}$$

where

$$H_{u_b} = H_u, \quad b_{u_b}(k) = h_u - H_u u_v(k). \tag{7.2}$$

Note that $\mathcal{U}_b(k)$ is a polytope whose boundaries vary with the value of u_v, which itself depends on the load demand (i_L, v_{Ld}) as well as cell resistances and OCVs. This polytope cannot be empty if u_v is in the interior of the set $\mathcal{U}$. This is guaranteed if v_{Ld} satisfies the condition (6.8). For example, for a 4-cell battery with $v_L = 9.25\,V$, Fig. 7.1 shows projection of $\mathcal{U}_b(i_L(k))$ on u_{b1}–u_{b2} plane for gridded $i_L \in \{-10c : 5c : 10c\}$. From (7.1), we can also define the following constraint polytope of null-space coefficients ρ_b

$$\mathcal{P}_b(k) = \{\rho_b(k) \,|\, H_{\rho_b}(k)\rho_b(k) \leq b_{\rho_b}(k)\} \subseteq \mathbb{R}^{2n-1}, \tag{7.3}$$

where

$$H_{\rho_b}(k) = H_{u_b} V_{\mathrm{n}}(k), \quad b_{\rho_b}(k) = b_{u_b}(k), \tag{7.4}$$

and $V_{\mathrm{n}}(k)$ is defined in (6.3).

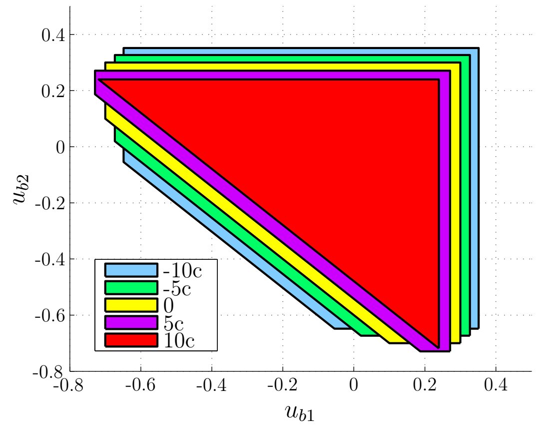

Figure 7.1: Projection of set $\mathcal{U}_b(k) \subseteq \mathbb{R}^4$ on $\mathbb{R}^2$ (u_{b1}–u_{b2} plane). Figure shows set variation as a function of i_L for a fixed voltage demand $v_{Ld} = 9.25\,V$.

Balancing Objective Function:

Using $N = 1$ in (6.13), the standard one-step quadratic objective function is given by

$$J(x(k), \rho_b(k)) = \Big[\|x(k+1)\|^2_{\bar{P}_x} + \|\rho_b(k)\|^2_{R_{\rho_b}}\Big], \tag{7.5}$$

where the terminal state penalty $\bar{P}_x$ and control penalty weighting matrices are given by (5.10) and (6.14) respectively.

7.1.1 Control Policy based on Unconstrained LQ

The optimal coefficient vector $\rho_b(k)$ for the balancing control $u_b(k)$ is computed at each time step $k \in \{0, \cdots, N_d\}$ by solving the following standard unconstrained LQ problem in a receding horizon fashion,

$$\begin{array}{rl} \text{minimize} & J(x(k), \rho_b(k)) \\ \text{subject to} & x(k+1) = A_d x(k) + \bar{B}_d(k)\rho_b(k), \end{array} \tag{P-V}$$

with optimization variables $x(k+1)$ and $\rho_b(k)$ for a given initial state $x(k)$ where N_d is the driving horizon. The problem (P-IV) is a one-step unconstrained LQ control problem. The *unconstrained optimal control policy* is given by

$$\rho_b^u(k) = K_{\rho_b}(k)x(k), \tag{7.6}$$

$$u_b^u(k) = K_{u_b}(k)x(k), \tag{7.7}$$

where the control gains $K_{\rho_b}(k)$ and $K_{u_b}(k)$ are simply given by a single recursion of the standard time-varying Riccati equation i.e.,

$$K_{\rho_b}(k) = -[R_{\rho_b}(k) + \bar{B}_d^{\mathrm{T}}(k)\bar{P}_x\bar{B}_d(k)]^{-1}\bar{B}_d^{\mathrm{T}}(k)\bar{P}_x A_d, \tag{7.8}$$

$$K_{u_b}(k) = V_{\mathrm{n}}(k)K_{\rho_b}(k), \tag{7.9}$$

where $\bar{P}_x$ is a fixed terminal penalty given by (5.10). The total unconstrained control policy is given by

$$u^u(k) = u_v(k) + u_b^u(k), \tag{7.10}$$

Note that the control policy u_b^u uses feedback about battery state x as well as feedforward knowledge about i_L and voltage control u_v, to achieve the balancing objectives.

7.1.2 Control Constraint via Euclidean Projection

The total control actions $u^u(k)$ based on unconstrained control policy (7.10) can violate the constraint $\mathcal{U}$ especially in cases where we have large thermal and SOC deviations and high load demands. The control $u(k) \in \mathcal{U}$ respecting the voltage constraint is guaranteed if $u_b(k) \in \mathcal{U}_b(k)$. Therefore, we propose to project $u_b^u(k)$ on the polytope $\mathcal{U}_b(k)$ whenever $u^u(k) \notin \mathcal{U}$. The projection $P_{\mathcal{U}_b}(u_b^u(k))$ is computed by solving the following QP problem,

$$\begin{array}{ll} \text{minimize} & \|u_b(k) - u_b^u(k)\|^2 \\ \text{subject to} & u_b(k) \in \mathcal{U}_b(k) \end{array} \tag{P-VI}$$

with optimization variable u_b where the set $\mathcal{U}_b(k)$ is defined in (7.1).

Remark 7.1. *Note that simply saturating the total unconstrained control signal u^u cannot work as it does not respect the voltage constraint. The proposed method of handling constraint via projection of u_b^u on $\mathcal{U}_b(k)$ can be considered as a special way of implementing saturation, which clips u^u without violating the voltage constraint.*

7.1.3 Summary of Projected LQ MPC Algorithm

The proposed control scheme (so-called *projected LQ MPC* or pLQ MPC) is summarized as Algorithm 3. This algorithm is based on simple analytical solutions except for the QP problem (P-VI), which can be efficiently solved in real-time on embedded hardware using library-free ANSI-C code generated, for example, by FORCES [99], which is a numerical optimization code generation framework for convex multistage problems. The control block diagram is shown in Figure 7.2 where Figure 7.2(b) shows the internal structure of the balancing controller.

Algorithm 3 Projected LQ MPC

```
Data: Load demand (v_Ld(k), i_L(k))
for k = 1 to N_d do
    Compute u_v(k), u_b^u(k), and u^u(k) using (6.9), (7.7), and (7.10)
    if u^u(k) ∉ 𝒰 then
        Compute u_b(k) = P_{𝒰_b}(u_b^u(k)) using (P-VI)
    else
        u_b(k) = u_b^u(k)
    end if
    Compute u(k) = u_v(k) + u_b(k)
    Apply u(k) to the modular battery system
end for
```

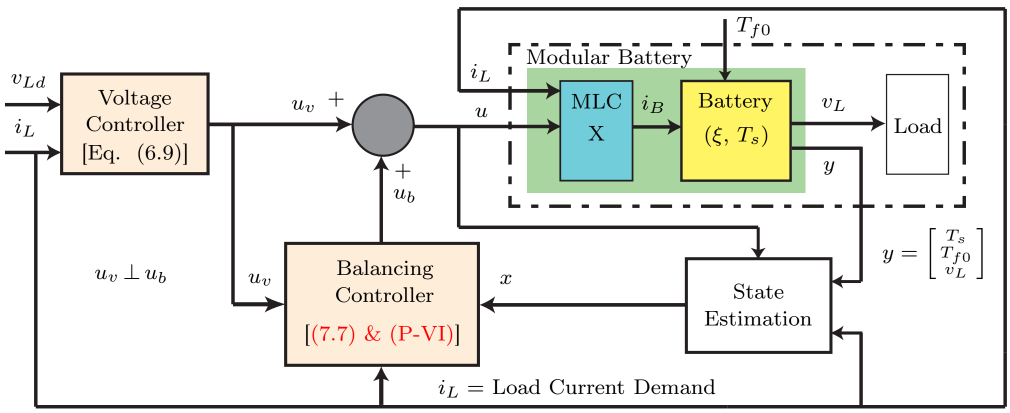

(a) Block diagram of battery control system.

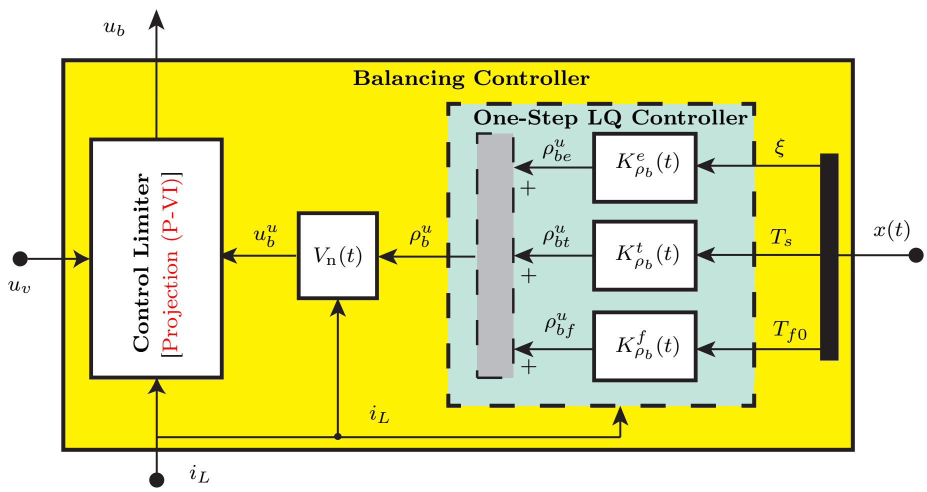

(b) Structure of two-stage balancing controller.

Figure 7.2: Block diagram of closed-loop control system of the modular battery with two-stage simple balancing controller.

7.2 Simulation Results and Discussion

The control performance and behavior of Algorithm 3 has been thoroughly investigated. The performance is also compared with 1-step constrained LQ MPC control Algorithm 2 proposed in Chapter 6 (see page 74). The simulation results are presented for ARTEMIS RURAL drive cycle using the same simulation setup as described in section 5.2.

7.2.1 Control Performance of Projected LQ MPC

The simulation results are shown in Figure 7.3. The proposed control algorithm achieves exact voltage regulation ($v_L(k) = v_{Ld}(k)$) as shown in Figure 7.3(a). In addition, the controller continuously reduces SOC imbalance throughout the driving and makes it negligible by the end of journey as shown in Figure 7.3(b) and 7.3(d). The controller is also able to keep temperature deviations within 1 ℃ limit during whole driving as shown in Figure 7.3(c) and 7.3(d). These figures show the effectiveness of the proposed balancing control algorithm.

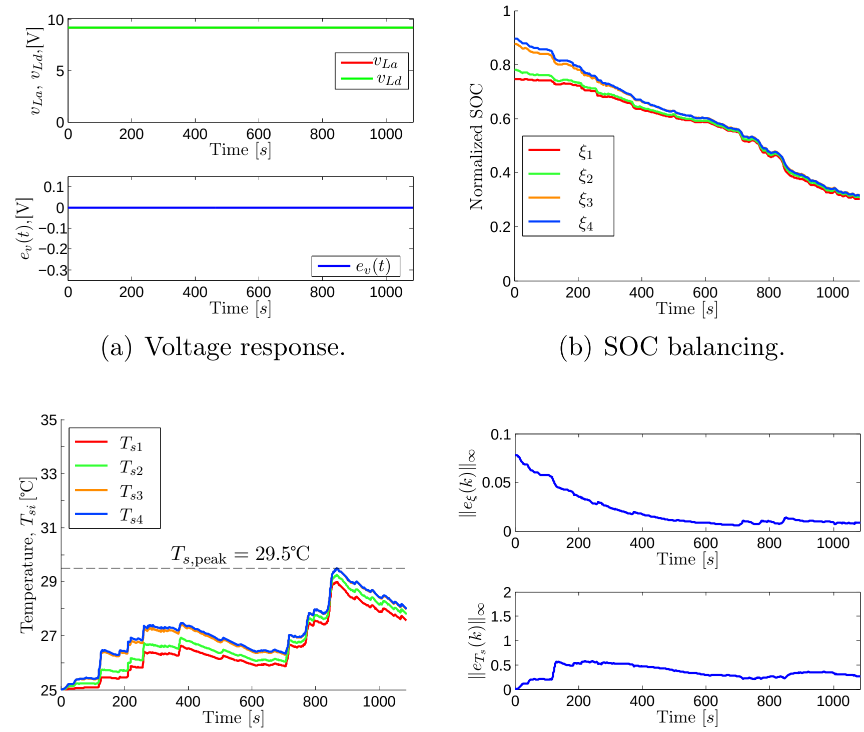

(a) Voltage response.

(b) SOC balancing.

(c) Thermal balancing.

(d) Balancing errors.

Figure 7.3: Simulation results for electro-thermal control performance of control *Algorithm 3 (pLQ MPC)* under *ARTEMIS RURAL drive cycle.*

7.2.2 Control Behavior

The unconstrained LQ controls and their projections (so-called *projected LQ controls*) on the constraint set $\mathcal{U}_b(k) \in \mathbb{R}^4$ (see Figure 7.1) are shown in Figures 7.4(a) and 7.4(b) respectively. During initial period of high SOC imbalance, the unconstrained control policy demands quite aggressive control actions (duty schedules) like fast discharging of cells 3 and 4 and charging of cells 1 and 2 to remove dischargeable capacity imbalance between these two groups of cells. However, these duty schedules violate the physical limits of the modular battery, and are thus practically infeasible. The projected control actions are relatively mild, but are physically realizable to achieve promising balancing performance. It is also interesting to note that after initial aggressive balancing phase, the unconstrained LQ control actions are mostly within limits and the projections are needed only during high load current intervals due to need of large correction for thermal balancing as well as shrinkage of balancing control polytope as shown in Figure 7.1.

The imbalance among cell duties and the difference in control behavior for each cell is quite visible. In particular, the control behavior for cells 1 and 2 is much different from that for cells 3 and 4. The difference is necessary to achieve cell balancing in the presence of capacity and resistance variations. For example, cells 1 and 2, which have lower dischargeable capacities than cells 3 and 4, are used less relative to cells 3 and 4 during initial heavy SOC balancing phase. However, to avoid overheating of cells 3 and 4 during each time interval of high load current demand, the controller decreases the duties of cells 3 and 4, which have relatively higher resistances, and increases the duties of cells 1 and 2. Note some resemblance between duties of cells 1 and 2 and also between duties of cells 3 and 4 due to closely matched characteristics of two cells in each of these pairs.

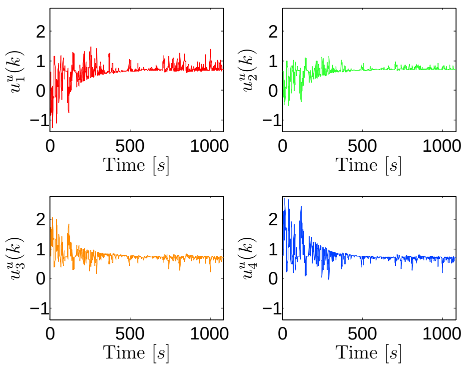

(a) Unconstrained LQ control signals.

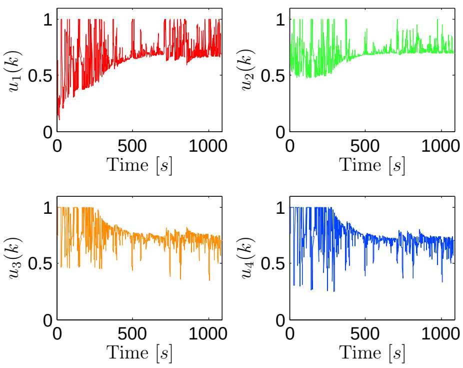

(b) Projected LQ Control Signals.

Figure 7.4: Control behavior before and after projections in Algorithm 3.

7.2.3 Comparison with Constrained LQ MPC

A quick comparison between simulation results of Algorithm 2 (see second row of Figure 6.7) and Algorithm 3 (see Figure 7.3) readily reveals that both algorithms show quite similar performance. The more detailed comparison between these two control algorithms is shown in Figure 7.5 in terms of cell duty and balancing error differences. The maximum instantaneous difference between cell duties (control signals) scheduled by the two control algorithms is shown in Figure 7.5(a), whereas the evolution of the balancing errors under both algorithms is shown in Figure 7.5(b). The maximum duty difference is less than 4% and the mean duty difference over whole drive cycle is 0.15%. This small difference between the two control trajectories has negligible effect on cell state trajectories and balancing errors as shown in Figure 7.5(b).

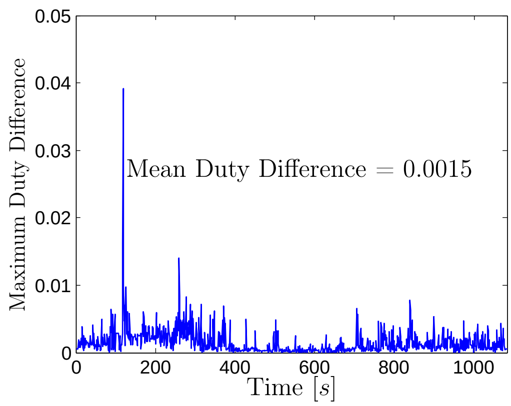

(a) Maximum difference between cell duty cycles (control signals).

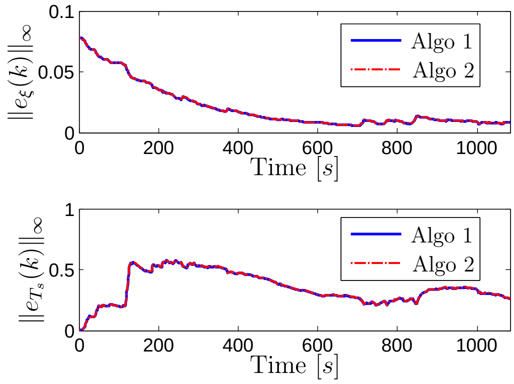

(b) Difference between balancing errors.

Figure 7.5: Closeness between control *Algorithm 2* and *Algorithm 3*.

7.3 Summary and Conclusions

The aim of this chapter was to simplify the balancing control problem (constrained LQ Problem (P-IV) on page 74). For this purpose, we proposed to solve the 1-step balancing control problem in two stages. The first stage issues a *balancing control policy* by solving a standard time-varying unconstrained LQ problem. The second stage generates *feasible control actions* ($u_i^+ \in [0, 1]$) by projecting unconstrained LQ control signals on a time-varying control constraint polytope. The novel way of splitting the balancing task into two separate subtasks (i.e. first generating a control policy and then handling control constraint separately via projections) is the main contribution of this chapter. This control algorithm, compared with control constrained LQ problem (P-IV), is not only computationally efficient and easy to implement, but also easy to understand and interpret as it reveals more structure and properties of the controller.

The performance of this simplified balancing controller is quite close to that of constrained LQ. The results revealed that the unconstrained LQ controller is mostly sufficient (i.e. projections are rarely required) if the SOC imbalance and/or the load demand is not too high. This means we may not always need to solve projection optimization problem, which may save us significant amount of computational time. The good balancing performance and computational efficiency of the proposed algorithm makes it interesting for real-time control implementation in large battery packs [see Chapter 9]. In addition, the proposed control algorithm has special underlaying structure, which may provide us deeper insight into structural and functional properties of the balancer to implement even simpler rule-based controller. This is investigated in the next chapter.

Chapter 8

Control Simplification 2: Proportional Control

This chapter is an extension of the previous chapter. The main purpose is to further simplify the balancing controller in the UPC mode. The idea is to approximate the LQ control gain matrix (7.8) by studying its structural properties and solve the control projection problem (P-VI) by a simple algorithm. This leads to a simple proportional controller with load current dependent scalar gains. The controller can be easily implemented online as it is based on evaluating simple gain functions and doing straightforward iterations for Euclidean projection instead of strictly solving an optimization problem (P-VI). In addition, this study completely unfolds the internal working and reveals two dominant operational modes of the balancing controller, which leads to very simple balancing rules based on load current magnitude.

8.1 Study of LQ Control Gain Structure

From (7.6) and (7.7), it is straightforward to verify that the complete balancing control structure has the following form

$$\rho_b^u(k) = K_{\rho_b}(k)x(k) = K_{\rho_b}^e(k)\xi(k) + K_{\rho_b}^t(k)T_s(k) + K_{\rho_b}^f(k)T_{f0}. \tag{8.1}$$

$$u_b^u(k) = V_{\mathrm{n}}(k)\rho_b^u(k) = K_{u_b}^e(k)\xi(k) + K_{u_b}^t(k)T_s(k) + K_{u_b}^f(k)T_{f0}, \tag{8.2}$$

where $K_{\rho_b}^e/K_{u_b}^e$ and $K_{\rho_b}^t/K_{u_b}^t$ are feedback control gain matrices and $K_{\rho_b}^f/K_{u_b}^f$ is a feedforward gain vector to compensate the effect of measured disturbance T_{f0}. In this section, we study the structural properties of these gains under the assumption of zero parametric variations. The main purpose of this study is to develop a simple gain-scheduled proportional balancing controller shown in Figure 8.1 on page 114.

8.1.1 Preliminaries

Let us define matrices

$$M_1 = \begin{bmatrix} 1_{n-1} & 0 \end{bmatrix}, \quad M_2 = \begin{bmatrix} 0_{n-1} & I_{n-1} \end{bmatrix}, \quad M_3 = \frac{1}{n} 1_{n-1 \times n}, \tag{8.3}$$

which we use to define matrices

$$M_{\rho_b}^1 := M_1 - M_3 = M_1 M_e \in \mathbb{R}^{n-1\times n}, \tag{8.4}$$

$$M_{\rho_b}^2 := M_2 - M_3 = M_2 M_e \in \mathbb{R}^{n-1\times n}, \tag{8.5}$$

where M_e is defined in (5.5). The matrix $M_{\rho_b}^1$ maps states to SOC and temperature errors in Cell_1 i.e.

$$e_{\xi_1}(k) = \xi_1(k) - \bar{\xi}(k) = M_{\rho_b}^1 \xi(k), \tag{8.6}$$

$$e_{T_{s1}}(k) = T_{s1}(k) - \bar{T}_s(k) = M_{\rho_b}^1 T_s(k), \tag{8.7}$$

where $\bar{\xi}$ and $\bar{T}_s$ are mean SOC and temperature of the modular battery as defined in (5.1) and (5.2) respectively. The right invertible matrix $M_{\rho_b}^2$ maps states to SOC and temperature errors of Cell_2 to Cell_n i.e.

$$e_{\xi'}(k) = \xi'(k) - \bar{\xi}(k) \cdot 1_{n-1} = M_{\rho_b}^2 \xi(k), \tag{8.8}$$

$$e_{T_s'}(k) = T_s'(k) - \bar{T}_s(k) \cdot 1_{n-1} = M_{\rho_b}^2 T_s(k), \tag{8.9}$$

where $\xi' \in \mathbb{R}^{n-1}$ and $T_s' \in \mathbb{R}^{n-1}$ are SOC and temperature of cells 2 and n. Similarly, the so-called *ambient temperature error* is defined as follows

$$e_{T_f'}(k) = \left(W_{Td}' - \overline{W}_{Td} \cdot 1_{n-1}\right) T_{f0} = M_{\rho_b}^2 W_{Td} T_{f0}, \tag{8.10}$$

where $W_{Td} = hW_T$ (h is sampling interval and $W_T = [w_{ti}] \in \mathbb{R}^n$) is the T_{f0} influence vector where each w_{ti} describes the influence of T_{f0} on each Cell_i. In (8.10), $T_f' \in \mathbb{R}^{n-1}$ and $W_{Td}' \in \mathbb{R}^{n-1}$ are ambient temperature and T_{f0} influence vector of Cell_2 to Cell_n, and $\overline{W}_{Td} = \frac{1}{n} 1_n^{\mathrm{T}} W_{Td}$ is mean influence of T_{f0} on string of cells.

8.1.2 Gain Structure

To explore the structural properties of K_{ρ_b} let us rewrite (7.8) as follows

$$K_{\rho_b}(k) = \begin{bmatrix} K_{\rho_b}^e(k) & K_{\rho_b}^t(k) & K_{\rho_b}^f(k) \end{bmatrix} = \Psi_{\rho_b}(k) \Omega_{\rho_b}(k), \tag{8.11}$$

where

$$\Psi_{\rho_b} = -[R_{\rho_b}(k) + \bar{B}_d^{\mathrm{T}}(k) \bar{P}_x \bar{B}_d(k)]^{-1} \in \mathbb{R}^{(n-1)\times(n-1)} \tag{8.12}$$

$$\Omega_{\rho_b} = \bar{B}_d^{\mathrm{T}}(k) \bar{P}_x A_d \in \mathbb{R}^{(n-1)\times(2n+1)}. \tag{8.13}$$

Here $\bar{P}_x$ = blkdiag $\left(\gamma_1\bar{P}_E, \gamma_2\bar{P}_T + \gamma_3\bar{P}_{\bar{T}}, 0\right)$ and $R_{\rho_b} = V_{\mathrm{n}}^{\mathrm{T}} R_{u_b^+} V_{\mathrm{n}}$ (for UPC mode with $R_{u_b^+} = r_{u_b^+} I_n$) as defined in (5.10) and (6.14) respectively, and

$$A_d = \begin{bmatrix} A_{Ed} & 0 & 0 \\ 0 & A_{Td} & W_{Td} \\ 0 & 0 & 1 \end{bmatrix}, \quad \bar{B}_d = B_d(k)V_{\mathrm{n}}(k), \quad B_d = \begin{bmatrix} i_L B_{Ed} \\ i_L^2 B_{Td} \\ 0 \end{bmatrix}, \tag{8.14}$$

$$V_{\mathrm{n}} = \begin{bmatrix} V_{\mathrm{n}}' \\ I_{n-1} \end{bmatrix}, \quad V_{\mathrm{n}}' = -\begin{bmatrix} \frac{d_{v2}^+}{d_{v1}^+} & \cdots & \frac{d_{vn}^+}{d_{v1}^+} \end{bmatrix} \in \mathbb{R}^{1\times(n-1)}, \tag{8.15}$$

where $A_{Ed} = I_n$, $A_{Td} = I_n + hA_T$, $W_{Td} = hW_T$, $B_{Ed} = hB_E$, $B_{Td} = hB_T$ [see page 52 for definitions of A_T, B_T, W_T, and B_E] are system matrices and V_{n} is the null-space basis matrix [cf. (6.3)].

Structure of Ω_{ρ_b}:

The matrix Ω_{ρ_b} can be simply rewritten as

$$\Omega_{\rho_b} = \begin{bmatrix} \Omega_{\rho_b}^e & \Omega_{\rho_b}^t & \Omega_{\rho_b}^f \end{bmatrix}, \tag{8.16}$$

where

$$\Omega_{\rho_b}^e = \gamma_1 i_L V_{\mathrm{n}}^{\mathrm{T}} B_{Ed}^{\mathrm{T}} \bar{P}_E, \tag{8.17}$$
$$\Omega_{\rho_b}^t = i_L^2 V_{\mathrm{n}}^{\mathrm{T}} B_{Td}^{\mathrm{T}} \left(\gamma_2\bar{P}_T + \gamma_3\bar{P}_{\bar{T}}\right) A_{Td}, \tag{8.18}$$
$$\Omega_{\rho_b}^f = i_L^2 V_{\mathrm{n}}^{\mathrm{T}} B_{Td}^{\mathrm{T}} \left(\gamma_2\bar{P}_T + \gamma_3\bar{P}_{\bar{T}}\right) W_{Td}, \tag{8.19}$$

where $\bar{P}_E = M_e^{\mathrm{T}} P_E M_e$ and $\bar{P}_T = M_e^{\mathrm{T}} P_T M_e$ with matrix M_e defined in (5.5). Using $P_E = p_e I_n, P_T = p_t I_n$, and the fact that $M_e^{\mathrm{T}} M_e = M_e$, we get $\bar{P}_E = p_e M_e$ and $\bar{P}_T = p_t M_e$.

Now let us *assume zero parametric variations* (i.e. $C_{ei} = C_{ej}, R_{ei} = R_{ej}$) among cells. This implies that $B_{Ed} = -b_e^\star I_n$, $B_{Td} = b_t^\star I_n$, and $V_{\mathrm{n}}' = -1_{n-1}^{\mathrm{T}}$. Using these simplifications and assuming $\gamma_3 = 0$[1] we get

$$\Omega_{\rho_b}^e = -\gamma_1 b_e^\star p_e i_L V_{\mathrm{n}}^{\mathrm{T}} M_e, \tag{8.20}$$
$$\Omega_{\rho_b}^t = \gamma_2 b_t^\star p_t i_L^2 V_{\mathrm{n}}^{\mathrm{T}} M_e A_{Td}, \tag{8.21}$$
$$\Omega_{\rho_b}^t = \gamma_2 b_t^\star p_t i_L^2 V_{\mathrm{n}}^{\mathrm{T}} M_e W_{Td}. \tag{8.22}$$

Note that $V_{\mathrm{n}}^{\mathrm{T}} M_e = V_{\mathrm{n}}^{\mathrm{T}} \left(I_n - \frac{1}{n} 1_{n\times n}\right) = V_{\mathrm{n}}^{\mathrm{T}} - \frac{1}{n} V_{\mathrm{n}}^{\mathrm{T}} \cdot 1_{n\times n}$. Since $1_n \in \mathcal{N}(V_{\mathrm{n}}^{\mathrm{T}})$, we have $V_{\mathrm{n}}^{\mathrm{T}} \cdot 1_{n\times n} = 0$. Therefore, we have

$$V_{\mathrm{n}}^{\mathrm{T}} M_e = V_{\mathrm{n}}^{\mathrm{T}}. \tag{8.23}$$

[1] This implies that we are penalizing only balancing errors in the objective function.

Using this in (8.20)–(8.22) we get

$$\Omega^e_{\rho_b} = -\operatorname{sgn}(i_L)\omega^e_{\rho_b}(k)V_{\mathrm{n}}^{\mathrm{T}}, \tag{8.24}$$
$$\Omega^t_{\rho_b} = \omega^t_{\rho_b}(k)V_{\mathrm{n}}^{\mathrm{T}}A_{Td}, \tag{8.25}$$
$$\Omega^f_{\rho_b} = \omega^t_{\rho_b}(k)V_{\mathrm{n}}^{\mathrm{T}}W_{Td}. \tag{8.26}$$

where

$$\omega^e_{\rho_b}(k) = \gamma_1 b_e^\star p_e|i_L| \geq 0, \tag{8.27}$$
$$\omega^t_{\rho_b}(k) = \gamma_2 b_t^\star p_t i_L^2 \geq 0. \tag{8.28}$$

Structure of Ψ_{ρ_b}:

The matrix Ψ_{ρ_b} can be simplified as follows under above assumptions

$$\Psi_{\rho_b} = -\left[r_{u_b^+}V_{\mathrm{n}}^{\mathrm{T}}V_{\mathrm{n}} + p_e(b_e^\star)^2 i_L^2 V_{\mathrm{n}}^{\mathrm{T}}M_e V_{\mathrm{n}} + p_t(b_t^\star)^2 i_L^4 V_{\mathrm{n}}^{\mathrm{T}}M_e V_{\mathrm{n}}\right]^{-1}.$$

Since $V_{\mathrm{n}}^{\mathrm{T}}M_e V_{\mathrm{n}} = V_{\mathrm{n}}^{\mathrm{T}}V_{\mathrm{n}}$ (using (8.23)), the above equation gets simplified as

$$\Psi_{\rho_b} = -\frac{1}{\psi_{\rho_b}(k)} \cdot S_{\rho_b}, \tag{8.29}$$

where

$$\psi_{\rho_b}(k) = \gamma_4\, r_{u_b^+} + \gamma_1 p_e(b_e^\star)^2 i_L^2 + \gamma_2 p_t(b_t^\star)^2 i_L^4, \tag{8.30}$$

$$S_{\rho_b} = \left(V_{\mathrm{n}}^{\mathrm{T}}V_{\mathrm{n}}\right)^{-1} = \begin{bmatrix} \frac{n-1}{n} & -\frac{1}{n} & \cdots & -\frac{1}{n} \\ -\frac{1}{n} & \frac{n-1}{n} & \cdots & -\frac{1}{n} \\ \vdots & \vdots & \ddots & \vdots \\ -\frac{1}{n} & -\frac{1}{n} & \cdots & \frac{n-1}{n} \end{bmatrix}. \tag{8.31}$$

Scalar Feedback and Feedforward Gains:

Now using (8.16) and (8.29) in (8.11), we get

$$K^e_{\rho_b}(k) = L^e_{\rho_b}(k)V_{\mathrm{n}}^{\dagger}, \tag{8.32}$$
$$K^t_{\rho_b}(k) = L^t_{\rho_b}(k)V_{\mathrm{n}}^{\dagger}A_{Td}, \tag{8.33}$$
$$K^f_{\rho_b}(k) = L^t_{\rho_b}(k)V_{\mathrm{n}}^{\dagger}W_{Td}, \tag{8.34}$$

where $V_{\mathrm{n}}^{\dagger} = S_{\rho_b}V_{\mathrm{n}}^{\mathrm{T}} = \left(V_{\mathrm{n}}^{\mathrm{T}}V_{\mathrm{n}}\right)^{-1}V_{\mathrm{n}}^{\mathrm{T}}$ is a left pseudo-inverse of null-space basis matrix V_{n} and

$$L^e_{\rho_b}(k) = \operatorname{sgn}(i_L)k^e_{\rho_b}I_{n-1}, \quad k^e_{\rho_b} = \frac{\omega^e_{\rho_b}(k)}{\psi_{\rho_b}(k)}, \tag{8.35}$$

$$L^t_{\rho_b}(k) = -k^t_{\rho_b}I_{n-1}, \qquad k^t_{\rho_b} = \frac{\omega^t_{\rho_b}(k)}{\psi_{\rho_b}(k)}, \tag{8.36}$$

are time varying matrices with tunable positive scalar gains $k^e_{\rho_b}$ and $k^t_{\rho_b}$. It is straightforward to verify that $V_\mathrm{n}^\dagger = M^2_{\rho_b}$ [see (8.5)][2]. Therefore, we have

$$K^e_{\rho_b}(k) = \mathrm{sgn}(i_L)k^e_{\rho_b}(k)M^2_{\rho_b}, \tag{8.37}$$
$$K^t_{\rho_b}(k) = -k^t_{\rho_b}(k)M^2_{\rho_b}A_{Td} \approx -k^t_{\rho_b}(k)M^2_{\rho_b} \tag{8.38}$$
$$K^f_{\rho_b}(k) = -k^t_{\rho_b}(k)M^2_{\rho_b}W_{Td}, \tag{8.39}$$

where the approximation in (8.38) is obtained assuming fast sampling and loose thermal coupling between cells. Now using (8.37)–(8.39) in (7.9), we get full control gains

$$K^e_{u_b}(k) = \mathrm{sgn}(i_L)k^e_{\rho_b}(k)V_\mathrm{n}V_\mathrm{n}^\dagger, \tag{8.40}$$
$$K^t_{u_b}(k) \approx -k^t_{\rho_b}(k)V_\mathrm{n}V_\mathrm{n}^\dagger, \tag{8.41}$$
$$K^f_{u_b}(k) = -k^t_{\rho_b}(k)V_\mathrm{n}V_\mathrm{n}^\dagger W_{Td}. \tag{8.42}$$

It is interesting to note that $V_\mathrm{n}V_\mathrm{n}^\dagger$ is the orthogonal projection on $\mathcal{R}(V_\mathrm{n}) = \mathcal{N}(D_v)$ [cf. (6.2)]. This offers nice interpretations: the battery states are first mapped to the null-space and then proportional control gains are applied. The complete balancing control structure is shown in Figure 8.1.

Remark 8.1. *A thorough empirical study of* (8.11) *suggests that the factorization (shown in* (8.32)–(8.34)*) of the feedback gain matrices is approximately valid also for small parametric variations. In this case, the invertible matrices $L^e_{\rho_b}(k) = [\ell^e_{ij}(k)]$ and $L^t_{\rho_b}(k) = [\ell^t_{ij}(k)]$ become non-diagonal, but still have special structure with the following properties*

- *The matrices are still* diagonally dominant*, for most* practical parametric variations *(*20% *in capacity and* 100% *in resistance), with order of magnitude difference between diagonal and non-diagonal entries i.e.* $|\ell^e_{ii}| \gg |\ell^e_{ij}|,\ |\ell^t_{ii}| \gg |\ell^t_{ij}|$.
- *The diagonal entries are almost equal ($\ell^e_{ii} \approx \ell^e_{jj}$, $\ell^t_{ii} \approx \ell^t_{jj}$) for s*mall parametric variations.
- *The sign of ℓ^e_{ii} is the same as sign of i_L, whereas the sign of ℓ^t_{ii} is always negative.*
- *The magnitudes of $\ell^e_{jj}(k)$ and $\ell^t_{jj}(k)$ have significant dependence on load current i_L.*

[2] $M^2_{\rho_b}$ satisfies all four Penrose properties [98, Theorem 4.2] for pseduoinverse of V_n.

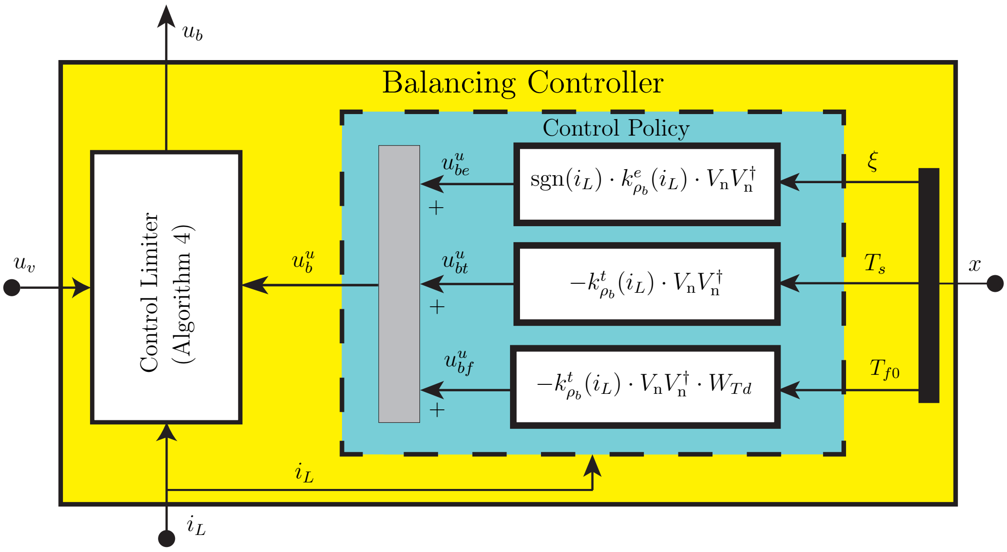

(a) Block diagram of two-stage balancing controller.

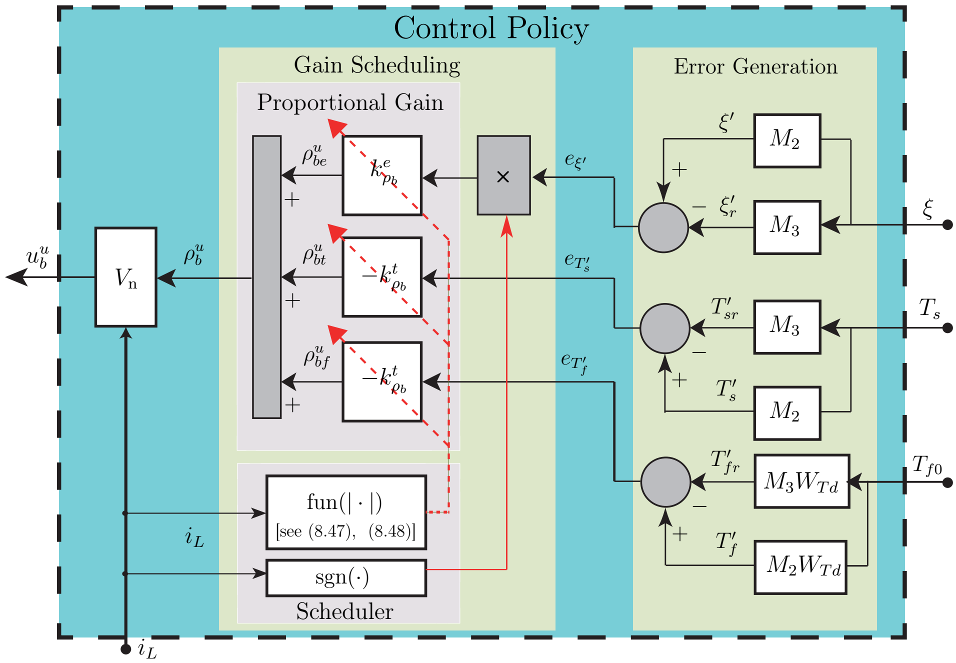

(b) Detailed internal structure of the gain-scheduled control policy.

Figure 8.1: Gain-scheduled proportional balancing controller (cf. Fig. 7.2).

8.2 Simple Proportional Balancing Scheme

The study in the previous section leads to the gain-scheduled proportional balancing controller [see Figure 8.1], which is discussed in detail below.

8.2.1 Balancing Policy and Interpretations

Using (8.40)–(8.42) in (8.2), we get the following (approximate) balancing control laws for each Cell$_i$ ($i \in \{2, \cdots, n\}$)

$$u^u_{bei}(k) \approx \mathrm{sgn}(i_L(k)) k^e_{\rho_b}(k) e_{\xi_i}(k), \tag{8.43}$$

$$u^u_{bti}(k) \approx -k^t_{\rho_b}(k) e_{T_{si}}(k), \tag{8.44}$$

$$u^u_{bfi}(k) \approx -k^t_{\rho_b}(k) e_{T_{fi}}, \tag{8.45}$$

where $e_{\xi_i}(k), e_{T_{si}}(k)$ are defined in (5.1), (5.2) respectively, and $e_{T_{fi}} = \left(w_{ti} - \overline{W}_{Td}\right) T_{f0}$ is the so-called ambient temperature error for each Cell$_i$. Note that (8.43)–(8.45) are balancing control laws for cells 2 to n (can be any $n-1$ cells), whereas the control law of Cell$_1$ is given by

$$u^u_{b1}(k) \approx V'_{\mathrm{n}}(k) \rho^u_b(k) = V'_{\mathrm{n}}(k) K_{\rho_b}(k) x(k), \tag{8.46}$$

which can be verified from (8.2), where V'_{n} is defined in (8.15). The control law (8.46) shows dependence of u^u_{b1} on control of other $n-1$ cells. In fact, the control of any Cell$_i$ can be represented as a linear combination of other controls using the fact that the balancing control does not influence the battery terminal voltage i.e. $D_v \cdot u_b = v_{Lb} = 0$.

Note that the SOC balancing rule (8.43) during charging and discharging are complement of each other. This makes sense because, to achieve SOC balancing, any Cell$_i$ with positive (negative) SOC error must be discharged more (less) during discharging and must be charged less (more) during charging. The thermal balancing rule (8.44) is same during both charging and discharging because current through a cell, regardless of its direction, always generates heat (i.e. cannot consume it). The disturbance compensation rule (8.45) only cancels out the ambient temperature errors for each cell. It makes sense as it is not required to completely cancel out the disturbance itself for balancing.

Note that if any cell has the same error sign for both SOC and temperature during discharging, then it will have conflicting usage requirements to achieve simultaneous thermal and SOC balancing. In this situation, the controller will benefit from short regeneration/charging phase, otherwise it will have to prioritize one of the two objectives. This trade-off can be established based on load current magnitude (load-based gain-scheduling).

8.2.2 Proportional Gain Scheduling

The control gains $k^e_{\rho_b}$ and $k^t_{\rho_b}$ are scheduled based on load current magnitude using following two methods.

Continuous Gain-Scheduling (PwGS):

For a battery with n *nominal cells*, $k^e_{\rho_b}$ and $k^t_{\rho_b}$ are given by the following rational functions of load current i_L [cf. (8.35) and (8.36)]

$$k^e_{\rho_b} = \frac{\gamma_1 h b^\star_e p_e |i_L(k)|}{\gamma_4 r_{u_b^+} + \gamma_1 p_e (hb^\star_e)^2 i^2_L(k) + \gamma_2 p_t (hb^\star_t)^2 i^4_L(k)}, \tag{8.47}$$

$$k^t_{\rho_b} = \frac{\gamma_2 h b^\star_t p_t i^2_L(k)}{\gamma_4 r_{u_b^+} + \gamma_1 p_e (hb^\star_e)^2 i^2_L(k) + \gamma_2 p_t (hb^\star_t)^2 i^4_L(k)}, \tag{8.48}$$

and the ratio between them is given by

$$\frac{k^t_{\rho_b}}{k^e_{\rho_b}} = \left(\frac{\gamma_2 b^\star_t p_t}{\gamma_1 b^\star_e p_e}\right) \cdot |i_L(k)|, \tag{8.49}$$

which linearly increases with current magnitude. The gains are plotted in Fig. 8.2(a) as a function of $|i_L| \in [0,\, 20c]$ for the penalty weight setting that is used in Chapter 6 for the MPC Algorithm 2. The gain curves and the ratio show strong trade-off between thermal and SOC balancing. Each of these objectives is mainly prioritized in different load current range. For example, SOC balancing is prioritized in lower to medium current range ($k^e_{\rho_b}$ peaks at $10c$ load current and then decreases) and thermal balancing is mainly prioritized in higher current range ($k^t_{\rho_b}$ peaks at $14c$). This behavior makes sense because thermal balancing is not much needed during low current intervals due to reduced thermal intensity. These *two dominant control modes* show that the simultaneous thermal and SOC balancing under unipolar control is not possible for continuously high load.

Simple Rule-based Gain-Scheduling (PwSR):

Considering the two dominant control modes in two different current ranges, we propose (assuming small control penalty) the following simpler gain scheduling [see Fig. 8.2(b)],

$$k^e_{\rho_b}(k) = \begin{cases} 0, & |i_L(k)| = 0 \\ 38, & |i_L(k)| \leq 8c \;\&\; |i_L(k)| \neq 0 \\ 19, & \text{otherwise} \end{cases} \tag{8.50}$$

$$k^t_{\rho_b}(k) = \begin{cases} 0, & |i_L(k)| = 0 \\ 1.3, & |i_L(k)| \leq 8c \;\&\; |i_L(k)| \neq 0 \\ 2.6, & \text{otherwise} \end{cases} \tag{8.51}$$

where the gain values are chosen such that the closed-loop poles remain inside unit circle for any $i_L \in [-20c, 20c]$. The above rules capture the main essence of the balancing controller i.e., if $|i_L| \leq 8c$, prioritize SOC balancing, else thermal balancing. Note that the load current level, chosen as $8c$ here, for switching gains is also a tuning parameter.

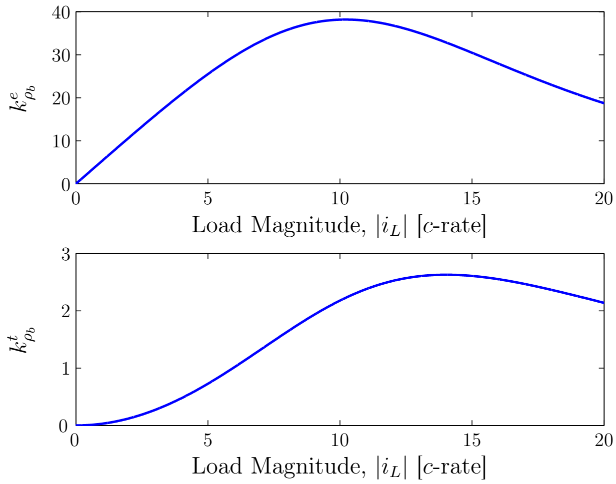

(a) Continuous gain scheduling (PwGS).

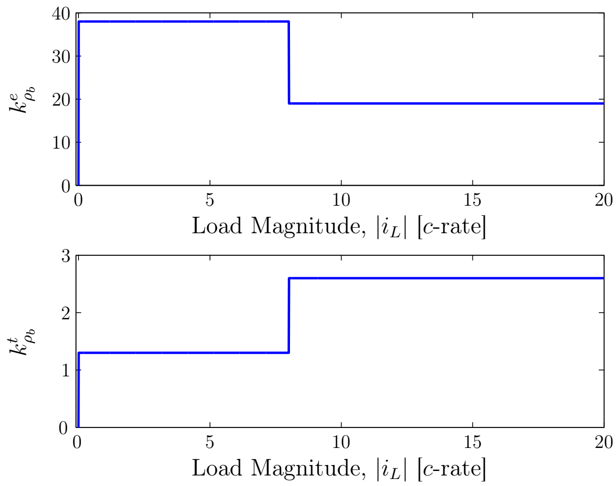

(b) Simple rule-based gain-scheduling (PwSR).

Figure 8.2: Proportional gains as function of load current i_L.

8.2.3 Simple Control Limiter

The balancing control limiter, originally formulated as problem (P-VI) in Chapter 7, is approximated here using a simple *heuristic* algorithm for easier implementation on a small embedded hardware. Let us first rewrite the balancing control polytope (7.1) as follows

$$\mathcal{U}_b(k) = \mathcal{U}_{b1}(k) \cap \mathcal{N}(D_v(k)), \tag{8.52}$$

where $\mathcal{N}(D_v)$ is a hyperplane as defined in (6.2) and

$$\mathcal{U}_{b1}(k) = \{u_b(k) \,|\, H_{u_b} u_b(k) \leq b_{u_b}(k)\}, \tag{8.53}$$

is a box constraint with H_{u_b} and b_{u_b} defined in (7.2). The problem (P-VI) gives Euclidean projection of unconstrained control u_b^u on the set $\mathcal{U}_b$. Here, we propose Algorithm 4 to approximate this projection by successively applying the following two Euclidean projections of u_b^u until convergence of the control error ε_{u_b}:

- Projection on box $\mathcal{U}_{b1}$ to satisfy $u_b \in \mathcal{U}_{b1}$ (lines 4−7).
- Projection on hyperplane $\mathcal{N}(D_v)$ to satisfy $v_L = v_{Ld}$ (lines 8−10).

Since these two projections have analytical solutions (see [97]), we get fast iterations. The algorithm converges if u_b^i moves closer to the intersection of box and hyperplane with each iteration. The solution is optimal (equivalent to solving (P-VI)) for $n = 2$, but may get suboptimal for $n > 2$ (particularly for large battery packs). Note that $u_{b,\min}$ and $u_{b,\max}$ used as inputs by Algorithm 4 are the known lower and upper limits on u_b at each time step.

Algorithm 4 Control limiter

1: **Given**: $u_b^u(k), u_{b,\min}(k), u_{b,\max}(k), D_v(k), \mathrm{tol}.$
2: **Set** $i = 1, \quad u_b^i = u_b^u, \quad \varepsilon_{u_b}^0 = 1_n$ ▷ Initialize
3: **while** $\left(\varepsilon_{u_b}^{i-1} \geq \ \mathrm{tol}\right)$ **do**
▷ Find limit violations
4: $I_{u_b}^{\mathrm{vl}} = \mathtt{find}(u_b^i < u_{b,\min})$
5: $I_{u_b}^{\mathrm{vu}} = \mathtt{find}(u_b^i > u_{b,\max})$
▷ Project on box
6: $u_b^i(I_{u_b}^{\mathrm{vl}}) = u_{b,\min}(I_{u_b}^{\mathrm{vl}})$
7: $u_b^i(I_{u_b}^{\mathrm{vu}}) = u_{b,\max}(I_{u_b}^{\mathrm{vu}})$
▷ Project on hyperplane
8: $\varepsilon_{v_{Lb}}^i = 0 - D_v u_b^i$ ▷ voltage error
9: $\varepsilon_{u_b}^i = D_v^{\dagger} \varepsilon_{v_{Lb}}^i$ ▷ balancing control error
10: $u_b^{i+1} = u_b^i + \varepsilon_{u_b}^i$ ▷ Correction/Update equation
11: $i \leftarrow i + 1$
12: **end while**
13: **return** u_b

8.2.4 Summary of Gain-Scheduled Control

The proposed *gain-scheduled proportional control* scheme is summarized as Algorithm 5. This algorithm is based on simple analytical solutions and an efficient control limiting Algorithm 4. The control block diagram is shown in Figure 8.1 where Figure 8.1(b) shows the internal structure of the balancing controller.

Algorithm 5 Gain-scheduled proportional control

Data: Load demand $(v_{Ld}(k), i_L(k))$
for $k = 1$ to N_d **do**
  Compute $u_v(k)$using (6.9),
  Compute $k^e_{\rho_b}(k)$ using either (8.47) [PwGS] or (8.50) [PwSR]
  Compute $k^t_{\rho_b}(k)$ using either (8.48) [PwGS] or (8.51) [PwSR]
  Compute $K^e_{u_b}(k)$ using (8.40)
  Compute $K^t_{u_b}(k)$ using (8.41)
  Compute $K^f_{u_b}(k)$ using (8.42)
  Compute $u^u_b(k)$ using (8.2)
  Compute $u^u(k) = u_v(k) + u^u_b(k)$
  if $u^u(k) \notin \mathcal{U}$ **then**
    Compute $u_b(k)$ by limiting $u^u_b(k)$ using Algorithm 4
  else
    $u_b(k) = u^u_b(k)$
  end if
  Compute $u(k) = u_v(k) + u_b(k)$
  Apply $u(k)$ to the modular battery system
end for

8.3 Simulation Results and Discussion

8.3.1 Simulation Setup

We evaluate, through simulations, the balancing performance of the two proposed proportional controllers (PwGS and PwSR) and compare it with that of 1-step constrained LQ MPC Algorithm 2 [see page 74][3]. The simulation results are presented for *US06* drive cycle using the same simulation setup as described in section 5.2. We must emphasize here that the MPC Algorithm 2 uses true cell parameters, but the proportional controllers are implemented assuming only nominal parameter values. All three controllers use sampling interval $h = 1\,\text{sec}$. Note that we do not require any special solvers for proportional controllers. However, for Algorithm 2, we need a QP solver like `CVX` [95] to solve control constrained LQ problem (P-IV).

8.3.2 Balancing Comparison with MPC

The evolution of SOC and temperature under three controllers (MPC, PwGS, and PwSR) is shown in Fig. 8.3 whereas the evolution of balancing errors ($\|e_\xi(k)\|_\infty$ and $\|e_{T_s}(k)\|_\infty$) is shown in Fig. 8.4. All three controllers significantly reduce SOC balancing error and achieve $\|e_\xi(k)\|_\infty \leq 2.5\%$ by the end of the driving trip as shown in upper subplot of Fig. 8.4. However, there is noticeable difference in terms of their balancing speed, performance variance (balancing error variance), evolution of temperature balancing errors, and peak cell temperature.

The MPC shows best overall performance in terms of peak cell temperature (33.1 ℃) and balancing speed. It achieves SOC balancing target while keeping temperature balancing error strictly within 1 ℃ during whole trip.

The PwGS shows SOC balancing performance that is comparable to MPC, but it results in slightly higher peak cell temperature (33.2 ℃) and higher temperature balancing error that rarely violates 1 ℃ limit.

The PwSR has slowest balancing performance, highest peak cell temperature (33.4 ℃), and highest performance variance. In particular, the temperature balancing error frequently violates 1 ℃ limit.

[3]Since 1-step projected LQ MPC Algorithm 3 proposed in Chapter 7 is shown to be almost equivalent in performance to Algorithm 2, it can be also used for comparison.

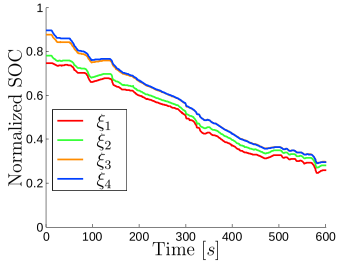

(a) **MPC**: SOC balancing.

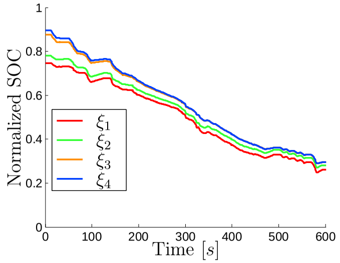

(b) **PwGS**: SOC balancing.

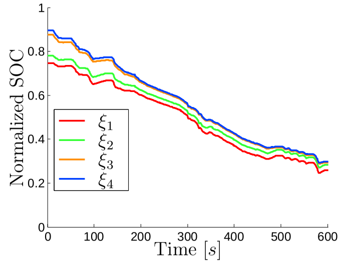

(c) **PwSR**: SOC balancing.

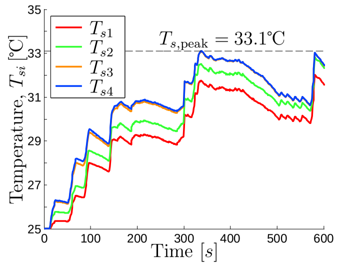

(d) Thermal balancing.

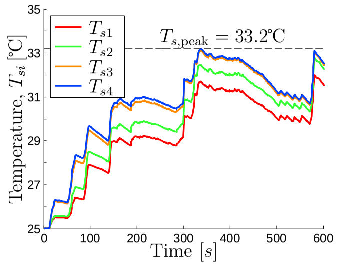

(e) Thermal balancing.

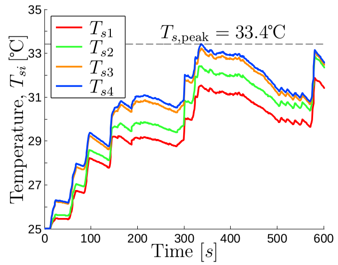

(f) Thermal balancing.

Figure 8.3: Simulation results for balancing performance of modular battery under *US06 drive cycle* are shown: first column: 1-step *consrtained MPC Scheme*; second column: *PwGS with Limiter*; and third column: *PwSR with Limiter*.

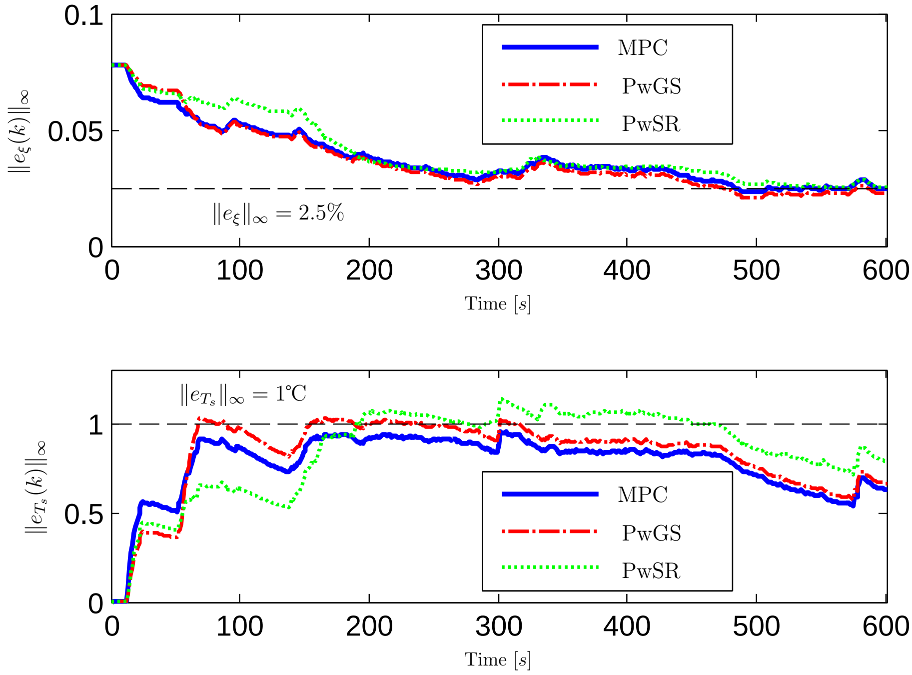

Figure 8.4: Balancing errors under three control schemes.

8.3.3 Computational Comparison with MPC

Table 8.1 shows the computational times (obtained on a PC with i7 processor and 16 GB RAM) for two stages (gain computation and projections) of PwGS and PwSR. We save significant time during the second stage of the proportional controllers compared to that of MPC Algorithm 3. There is no significant difference for first stage due to small size of problem in this simulation. However, for large n, the computation time of the first stage of Algorithm 3 may also grow significantly due to large matrix inversion in Riccati equation (7.8).

Table 8.1: Computational efficiency comparison

Online Timing ($n = 4$)	**MPC Algorithm 3**	**PwGS**	**PwSR**
Control Computation	50 μs	40 μs	23 μs
Control Projection	150 ms	1.2 ms	1.2 ms

8.4 Summary and Conclusions

In the previous chapter, we proposed LQ MPC based balancing controller with two stages to solve thermal and SOC balancing problem of a modular battery. The first stage computes time-varying LQ control gains and second stage performs Euclidean control projections to satisfy control constraint.

The main purpose of this chapter was to propose a simple proportional balancing controller by investigating the structural properties of LQ control gains. In addition, we aimed to approximate the control projections with simple heuristic algorithm. This study discovered that, under the assumption of small cell parametric variations, each time-varying control gain matrix can be factorized into a constant matrix and a time-varying scalar gain. We derived two scalar gains (one for SOC and the other for thermal balancing) as rational functions of load current. We also proposed simple iterations to compute projections. These approximations result in a simple and computationally efficient proportional balancing controller (PwGS), which can be easily implemented on low-power embedded hardware as it does not require solving any optimization problem. The study has also revealed two dominant modes of the balancing controller i.e. SOC balancing in low current range and thermal balancing in high current range. These two dominant control modes show that the simultaneous SOC and thermal balancing is not possible for continuously high load current under UPC operation of the modular battery, supporting our discussion in Section 6.4. Using this insight, we also proposed another rule-based proportional balancing controller (PwSR), capturing these two modes.

The performance of PwGS and PwSR with heuristic control limiter have been thoroughly evaluated for an aged battery with four cells having parametric variations and also compared with 1-step LQ MPC Algorithm 2, which have full access to true battery parameters. Although, both controllers have been implemented assuming new and identical battery cells, we still get acceptable balancing performance. In particular, the balancing performance of PwGS is comparable to MPC. The control performance, both in terms of balancing and computational efficiency, is promising in this simulation case study. It is also pertinent to mention here that the control performance under heuristic control limiter may degrade for large battery pack. In such cases, we may still use the proposed gain-scheduled proportional controllers, but with the QP-based control limiter (i.e., solving the original Euclidean control projection problem of the previous chapter).

Chapter 9

Case Study: Automotive Battery

This chapter presents a simulation case study of a large automotive battery pack. In the previous chapters, the simulation studies are confined to a small modular battery (4 cells) mainly due to convenience in graphical illustrations. This enabled us to thoroughly analyze the functional and structural properties of the controller. In addition, due to small size of the control problem, we were able to quickly test the controller under various driving situations and parameter settings in both UPC and BPC modes. However, the control design methodology still needs to be verified for large battery packs. In particular, the simplified control design methodology (1-step projected LQ MPC Algorithm 3) proposed in Chapter 7 needs to be validated as it is not obvious whether two-stage balancing control concept would perform equally well for large packs. In addition, the control performance in the presence of large thermal gradient in the coolant needs to be tested. In short, the main purpose is to show the scalability of our control design methodology with increased pack size and large thermal gradient in the battery coolant.

9.1 Simulation and Battery Setup

The modular battery considered for this case study consists of 63 modules, each containing 9 parallel cells ($3.3V$, $2.3Ah$, A123 ANR26650M1A). The nominal values of cell's electro-thermal parameters are shown in Table 5.1 whereas the battery configuration and the module/coolant parameters (scaled according to the module size) are shown in Table 9.1. The battery configuration is selected to match the battery of Toyota Prius PHEV I. For evaluation of balancing performance, the true cells are assumed to have capacity, resistance, and initial SOC variations as shown in Figure 9.1. The battery load profile under US06 drive cycle is shown in Figure 9.2.

Table 9.1: Large battery pack configuration and coolant parameters

Parameters	**Expression**	**Nominal Values**
Battery/Module configuration	$n_s\mathrm{S}n_p\mathrm{P}$	63S1P/1S9P
Battery/Module voltage capacity	$V_{\mathrm{B}}(v_{L,\max})/V_{Bi}$	$207.9\,V/3.3\,V$
Battery/Module charge capacity	C_{B}/C_{ei}	$20.7\,Ah/20.7\,Ah$
Battery/Module energy capacity	E_{B}/E_{Bi}	$4.30\,kWh/68.25\,Wh$
Battery/Module resistance	R_{eB}/R_{ei}	$80\,m\Omega/1.27\,m\Omega$
Module heat capacity	C_{si}	$643.5\,JK^{-1}$
Air volumetric flow rate	$\dot{V}_f$	$0.1496\,m^3s^{-1}$
Air inlet speed/temperature	U_f/T_{f0}	$7.87\,ms^{-1}/25$ ℃
Air thermal conductance	c_f	$175\,WK^{-1}$
Convective thermal resistance	R_{ui}	$0.2673\,KW^{-1}$

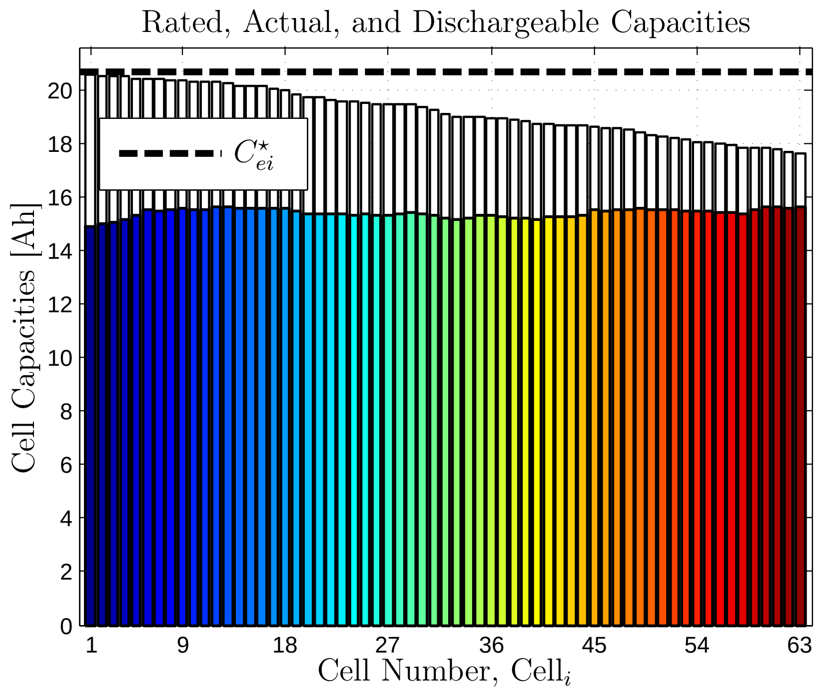

(a) Capacity distribution.

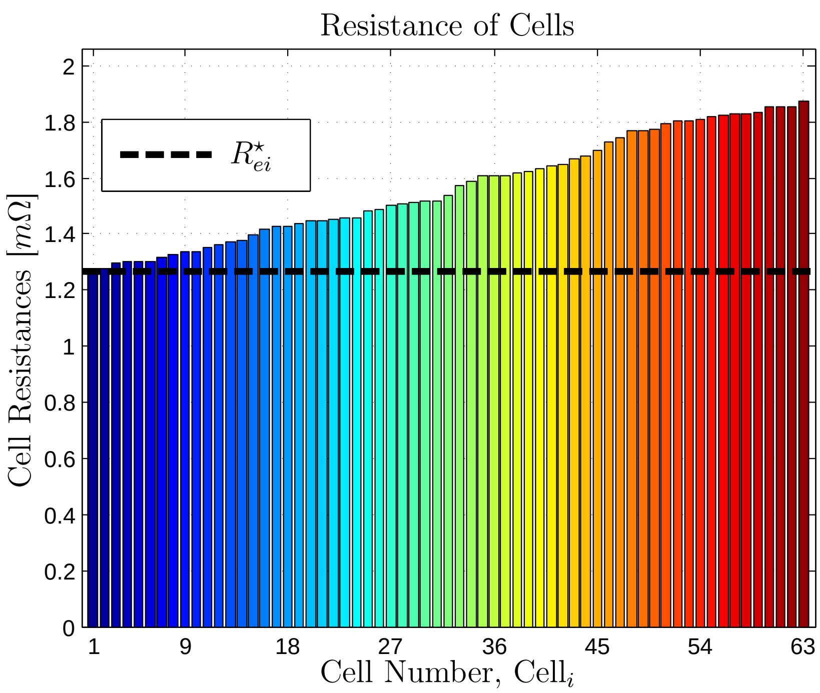

(b) Resistance distribution.

Figure 9.1: Capacity and resistance distributions of cells. These distributions are generated such that some cells in the string have conflicting usage requirement for SOC and thermal balancing [cf. discussion in section 5.2.2].

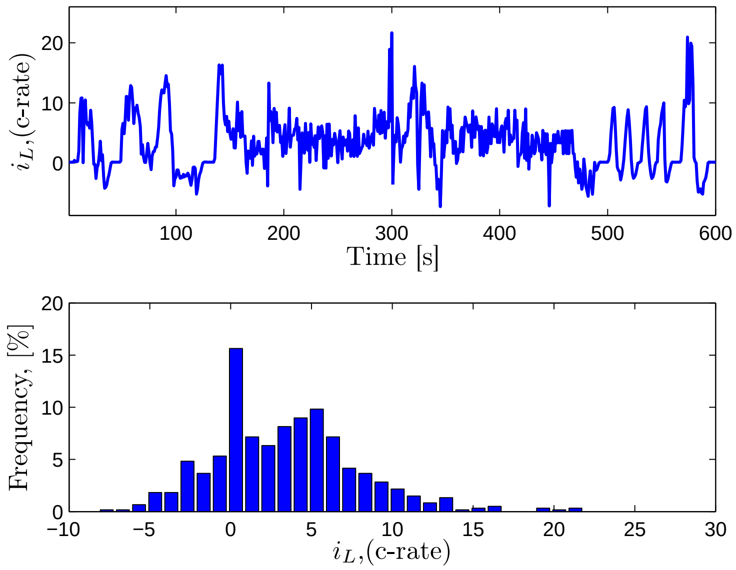

Figure 9.2: Battery load current and the histogram for one trip of *US06*.

9.2 Simulation Results and Discussion

Since the coolant temperature gradient may be significant in large battery packs with long strings of cells, we investigate the performance of our control scheme under both unidirectional and reciprocating coolant flows.

9.2.1 Unidirectional Coolant Flow

The simulation results for both UDO and 1-step MPC under unidirectional coolant flow are shown in Figure 9.3. The balancing performance is shown in terms of maximum cell-to-mean (i.e., $\|e_\xi(k)\|_\infty$ and $\|e_{T_s}(k)\|_\infty$) as well as *maximum cell-to-cell balancing errors* (i.e., $\|\Delta_\xi(k)\|_\infty = \max_{i,j}(|\xi_i(k) - \xi_j(k)|)$ and $\|\Delta_{T_s}(k)\|_\infty = \max_{i,j}(|T_{si}(k) - T_{sj}(k)|)$). These plots clearly show that our proposed MPC algorithm exhibits good thermal and SOC balancing performance. The maximum cell-to-cell SOC deviation is reduced to almost 2.3% by the end of driving trip compared to 9% under UDO. Due to SOC balancing, the final remaining dischargeable capacity distribution as shown in Figure 9.4 is now more uniform compared to its initial state shown in Figure 9.1(a). Similarly, the maximum cell-to-cell temperature deviation is mostly kept within 3 ℃ during whole driving compared to almost monotonic increase up to 6 ℃ under UDO. In addition, the peak temperature under MPC is almost 2 ℃ less than that under UDO. These benefits of our proposed control scheme may have significant long term positive impact on battery ageing and may lead to longer battery lifetime.

The average and rms current distributions under u_v, u_b, and u are shown in Figure 9.5. The controller in essence works as charge and heat shuffler similar to the small battery pack case discussed in Chapter 6.

9.2.2 Reciprocating Coolant Flow

The simulation results for both UDO and 1-step MPC under reciprocating coolant flow are shown in Figure 9.6. Comparing these plots with those of Figure 9.3, it is clear that the RF complements the MPC algorithm to achieve even better thermal balancing performance. In particular, the maximum cell-to-cell temperature deviation is now mostly within 1 ℃ during whole driving and reduces to less than 0.5 ℃ (versus 3 ℃ under UF i.e., six times reduction) by the end of driving. It is because the reciprocating flow saves some control effort of the controller by reducing the coolant temperature gradient. The controller invests this extra effort for better compensation of thermal balancing errors arising from parametric variations. Although temperature deviation under UDO now also reduces to 2 ℃ (versus 6 ℃ under UF i.e., three times reduction), it is still significantly higher than that under MPC. Similarly, the peak temperature under MPC is also less than that under UDO (31.8 ℃ versus 32.4 ℃). Therefore, the optimal load management adds significant benefit regardless of cooling scheme.

9.3 Conclusions

In this chapter, we have applied our simple control design method (1-step projected LQ MPC Algorithm 3 i.e., two stage balancing control computation) to a large automotive battery pack. The control performance is tested thoroughly in simulations under both unidirectional and reciprocating coolant flows. We get significant benefit in terms of improving charge-throughput capability of the battery, decreasing peak cell temperature, and reducing maximum cell-to-cell temperature deviation. It is also shown that the controller significantly benefits from reciprocating coolant flow i.e., controller is able to make best use of the extra control effort provided indirectly by the cooling scheme. The computational efficiency is also high. In addition, the controller has similar functional properties as discussed in previous chapters. In short, the consistent control behavior and the balancing performance in large battery pack shows the validity and scalability of our complete control design methodology.

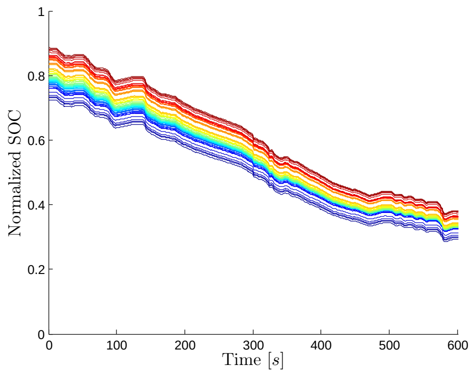

(a) *UDO under UF*: SOC balancing.

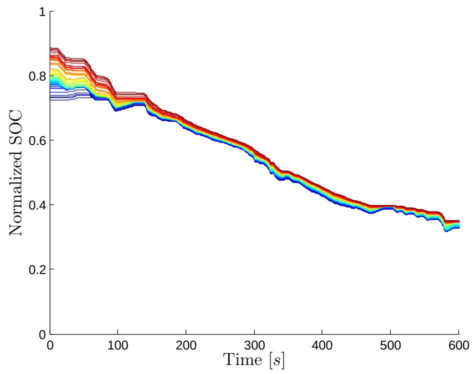

(b) *MPC under UF*: SOC balancing.

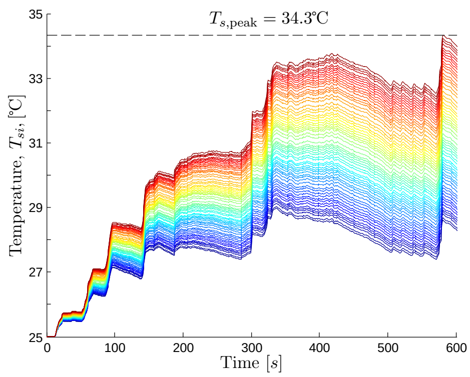

(c) Thermal balancing.

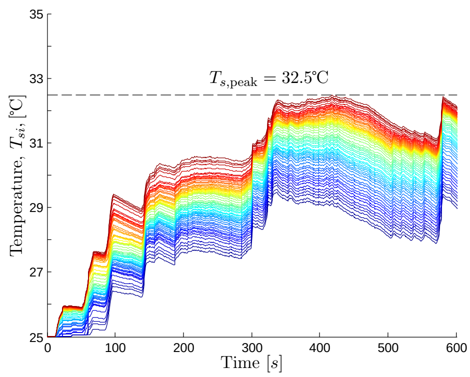

(d) Thermal balancing.

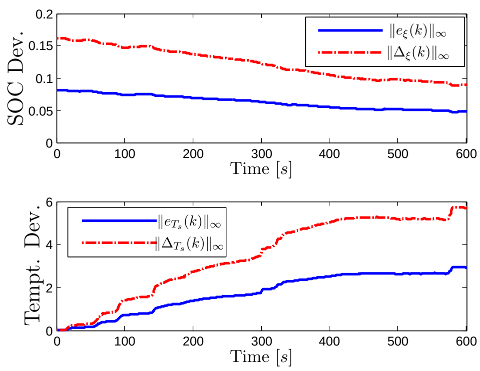

(e) Balancing errors.

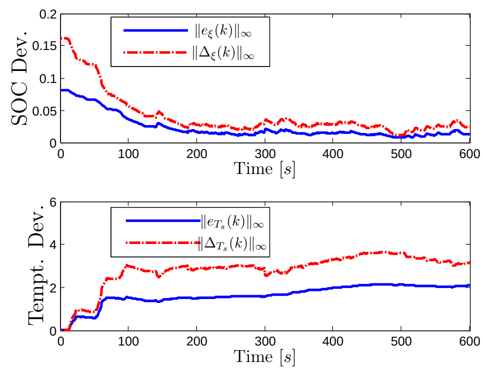

(f) Balancing errors.

Figure 9.3: Balancing performance comparison under unidirectional coolant flow (UF) for one trip of *US06 drive cycle*: *Uniform Duty Operation (UDO)*: first column; 1-*step projected LQ MPC in UPC mode*: second column.

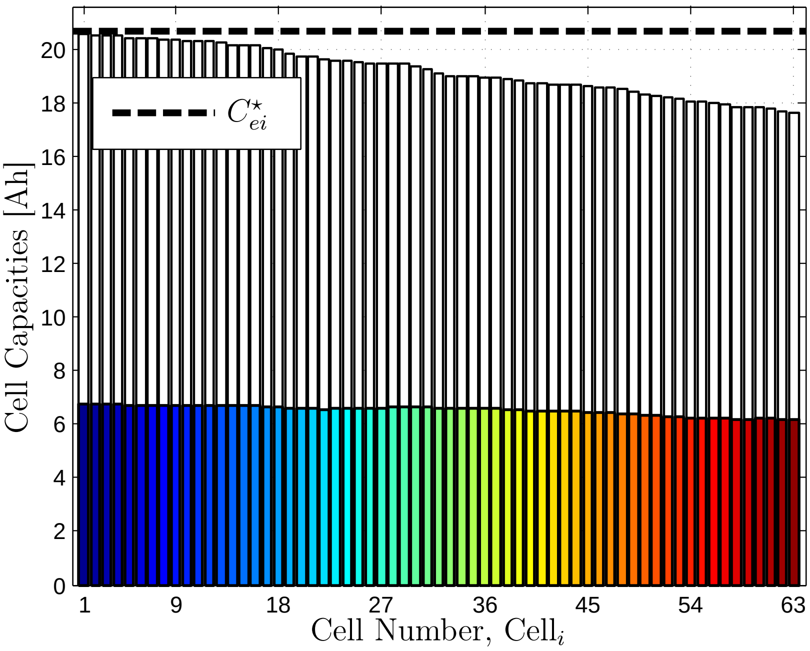

Figure 9.4: Final dischargeable capacity distribution after one trip of US06.

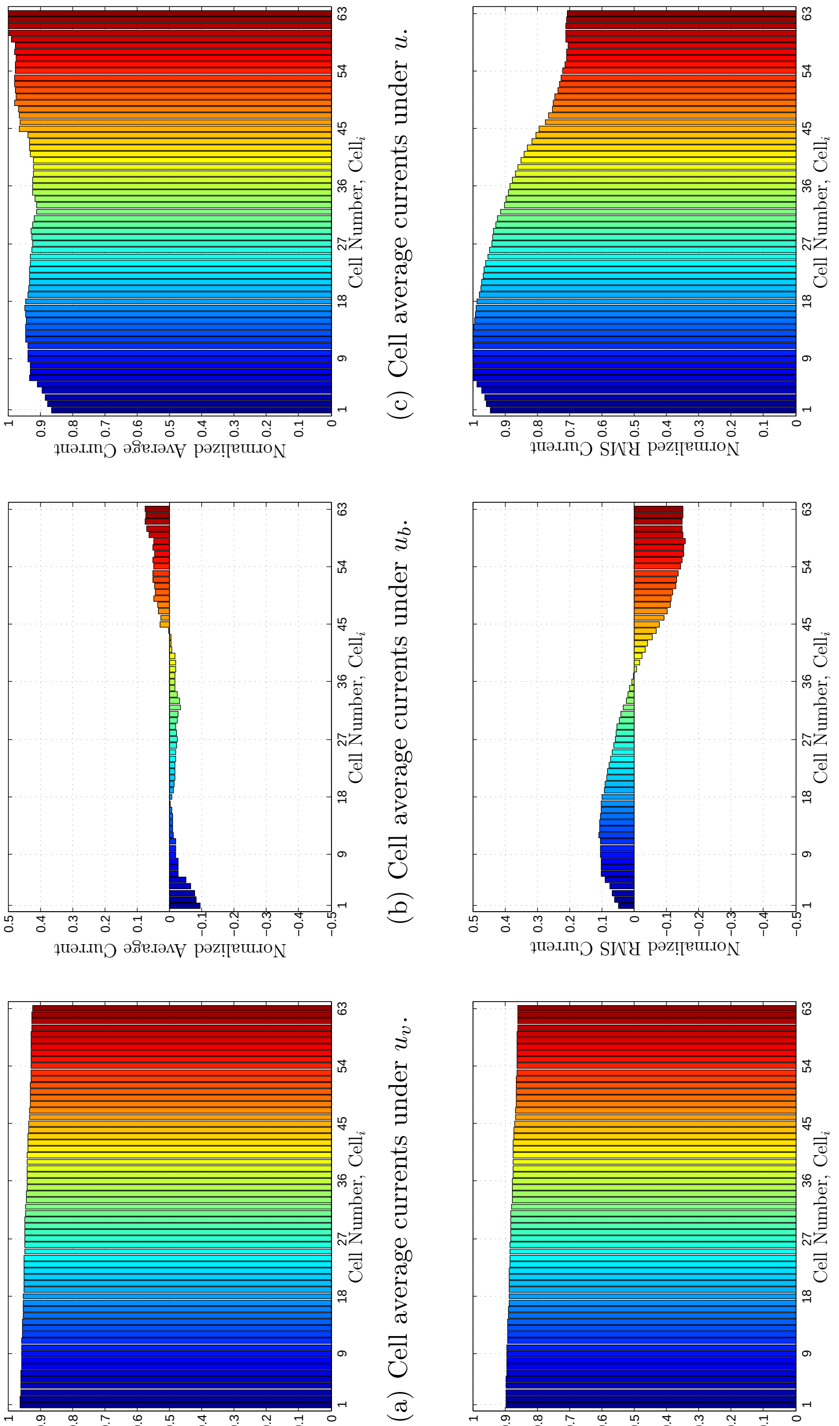

(a) Cell average currents under u_v.

(b) Cell average currents under u_b.

(c) Cell average currents under u.

(d) Cell rms currents under u_v.

(e) Cell rms currents under u_b.

(f) Cell rms currents under u.

Figure 9.5: Cell average and rms current behavior for US06 drive cycle under u_v, u_b, and u (UF case). The balancing controller slightly shuffles cell charges and heat to achieve thermal and SOC balancing simultaneously.

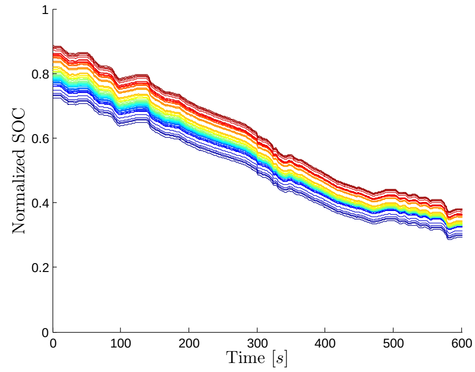

(a) *UDO under RF*: SOC balancing.

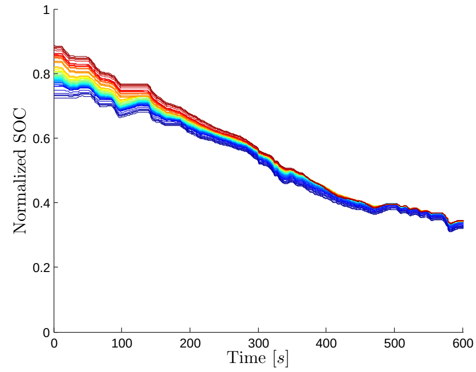

(b) *MPC under RF*: SOC balancing.

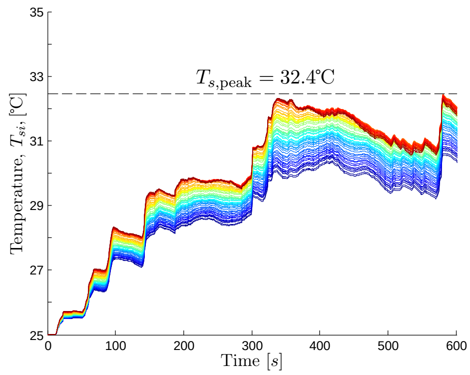

(c) Thermal balancing.

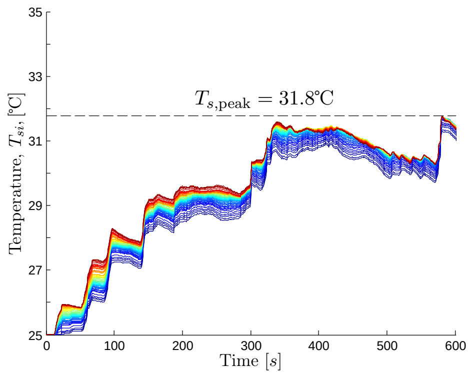

(d) Thermal balancing.

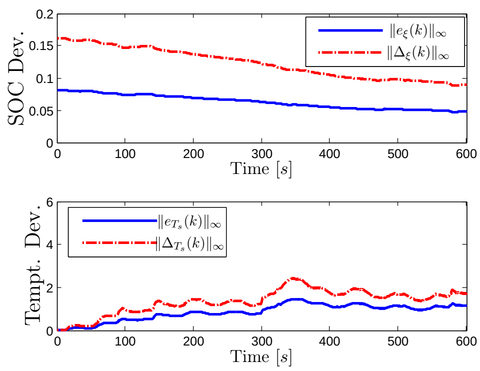

(e) Balancing errors.

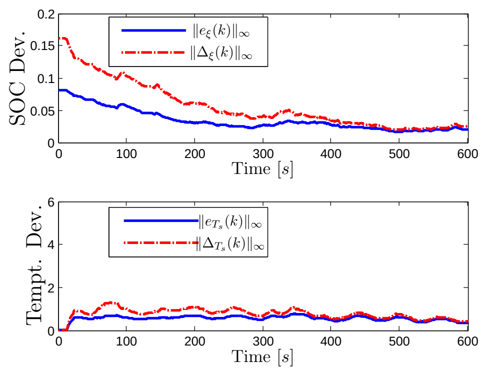

(f) Balancing errors.

Figure 9.6: Balancing performance comparison under reciprocating coolant flow (RF) for one trip of *US06 drive cycle*: *Uniform Duty Operation (UDO)*: first column; 1-*step projected LQ MPC in UPC mode*: second column.

Chapter 10

Conclusions

This thesis proposed a cascaded converter based modular battery concept, which allows cell-level control including cell-shunting. The control problem (stated on page 7) of this modular battery boils down to the *load sharing or load management problem*. We had multiple electro-thermal control objectives, including simultaneous thermal and SOC balancing as well as terminal voltage control. These control objectives have been formalized in this thesis while answering particular research questions (**Q1**–**Q5**) raised in Section 1.3. The control design is mainly based on convex optimization approach, which uses a quadratic criterion in SOC and temperature deviations, linear dynamics, and affine inequality constraints. The optimizer decides the power flow out of (or into) each cell at each time instant to meet the total driving (or regenerating) power demand such that all cells remain balanced in terms of SOC and temperature gauges.

10.1 Main Findings

We proposed various optimal control methods with decreasing complexity, which made the control problem and its solution more transparent and accessible. This enabled us to progressively investigate the aforementioned research questions. The feasibility question (**Q1**) has been addressed gradually throughout this thesis mainly using qualitative approach. In particular, Chapter 3 first added some preliminary discussion on this and then Chapter 6 investigated it further. The convex modeling and optimal control problem formulation of the modular battery have been presented in chapters 4 and 5 respectively, thereby answering **Q2.a**, whereas questions **Q2.b** and **Q2.c** have been evaluated through simulations in Chapter 5. A novel model predictive control (MPC) scheme has been presented in Chapter 6 to address **Q3** primarily. In addition, it also revealed a lot of nice structure, which enabled us to thoroughly investigate **Q4**. The approximation and simplification of the optimal control solution has been done in chapters 7 and 8, which enabled us to propose simple balancing controllers, answering **Q5**. This simplification added further insight into the internal working of thermal and SOC balancer and, therefore, shed more light on questions **Q1.c** and **Q4.e**. In the following, we summarize our main findings while answering the particular research questions.

A1. About problem feasibility:

- **a.** The simultaneous balancing of temperature and SOC is feasible in average sense subject to load variations (i.e. load is not always high) and surplus voltage (requires cell redundancy) in the modular battery. In addition, the SOC and temperature deviation allowances need to be specified. We have also observed that the availability of brake regeneration phases in the drive cycle may facilitate the balancing.
- **b.** The BPC mode, without even requiring load current variations, gives better balancing performance than UPC, but at the cost of reduced efficiency and higher voltage capacity (or cell redundancy). The UPC requires at least current direction reversal for acceptable balancing performance. In short, the UPC is a more cost and energy efficient solution for EV and PHEV applications whereas the BPC can be beneficial in applications involving load cycles with high current pulses of long duration.
- **c.** The driving behavior has significant impact on the balancing performance. The aggressive driving like US06 is more challenging for simultaneous thermal and SOC balancing compared to benign/normal drive cycles like urban stop-n-go and ARTEMIS Rural. It is mainly due to decrease in voltage capacity as a result of higher internal losses, which shrinks the balancing control constraint set (i.e., less control freedom).

A2. About global optimal control solution:

- **a.** The global optimal control (load management) of the modular battery can be formulated as a constrained convex optimization problem. The main challenge was to preserve the convexity of the electro-thermal model under switching action of power electronics in both UPC and BPC modes. This has been overcome by using state averaging approach under the assumption of orthogonality between two switching functions inside each module, fast switching, and slow load variations.

b. The optimal control of the modular battery can reduce balancing errors, peak cell temperature, and losses compared to those under uniform usage of cells. This is significant particularly in battery applications with parametric imbalance among its cells.

c. We have shown that reciprocating air flow (RF) has no significance for the optimal controller in short battery strings. However, in long battery strings, the RF may save some control effort by reducing the coolant temperature gradient. This extra control effort can then be invested for better compensation of state deviations arising from parametric variations.

A3. About control design using limited future load demand:

a. During our quest for control simplification, we proposed a novel idea of orthogonal decomposition of controller into two additive components, one for voltage control and the other for balancing control. This problem decomposition is one of the major contributions, which not only enabled the application of constrained LQ MPC scheme to solve the balancing problem elegantly, but also made it possible to analyze structural and functional properties of the balancer.

b. In the beginning, we had an intuition that using information about future load demand over long horizon would have large influence on scheduling the load of each cell at present time. However, our later investigation showed that a one-step prediction horizon using current load information is sufficient to decide reasonable load distribution for achieving acceptable balancing performance. The longer horizons may improve the performance, but the difference is not very significant.

A4. About control analysis and characterization:

a. The optimal control scheme is based on voltage and balancing controllers. The voltage controller is a feedforward type, which uses information only about load demand to regulate battery terminal voltage. The voltage control signal is computed analytically (minimum norm solution). The balancing control law in general is a piecewise-affine feedback in battery state. However, when constraints are inactive, it has a simple time-varying LQ structure. The balancing policy also uses information about load current and voltage control action to generate feasible actions for thermal and SOC balancing.

b. The controller is robust to parametric uncertainty and small resistance variation in a typical operating temperature range $[25, 40]$°C, which is normally maintained by active cooling of batteries in xEVs. In particular, the voltage controller, due to its feedforward nature, is affected more than the balancing controller. However, the voltage regulation is still acceptable as the terminal voltage error is very small as shown by the sensitivity relation derived in this thesis.

c. We have shown that the voltage and balancing control tasks are separable. However, the voltage control decisions affect the size of balancing control constraint set, which in turn affects the balancing capability.

d. The total control action is a sum of voltage and balancing controls. The total control and the voltage control are both positively constrained, whereas the balancing control may attain both positive and negative values. In this context, we can interpret the balancing control as a *control correction term* with a possibility of both positive and negative corrections. The voltage controller first decides the duty of each cell to exactly satisfy the voltage demand without caring about balancing. The balancing controller then corrects (either increase or decrease) the cells' duties in accordance with their balancing errors without disturbing the voltage. In short, the balancing controller acts as virtual charge and heat shuffler (power redistributor) to achieve thermal and SOC balancing.

e. Two dominant operational modes of the balancing controller have been identified: SOC balancing mode in low to medium load current range and thermal balancing mode in high current range.

A5. About control simplification:

a. The optimal balancing control solution (constrained LQ MPC) is approximated in two stages. The first stage computes a balancing control policy based on an unconstrained LQ problem and the second stage enforces constraint on control actions via projection on a time-varying balancing control constraint set. We have observed that the proposed approximation gives almost similar performance as constrained LQ MPC. The proposed control simplification is also verified in a large battery pack.

b. We have proposed a gain-scheduled proportional balancing controller by investigating the structural properties of constrained

LQ MPC. This investigation revealed a particular factorization of time-varying control gain matrices, which led to approximation of matrix gains as scalar gains under the assumption of small parametric variations among battery cells. The gains are scheduled in load current for nominal cells. These simplifications resulted in a simple rule-based controller, which uses only load current magnitude for switching control gains to achieve desired tradeoff between thermal and SOC balancing. We have also proposed a simple control limiter, which efficiently computes control projection on the constraint set. These simplifications led to a computationally efficient controller, which can be easily implemented on low power embedded hardware.

10.2 Concluding Remarks

The proposed control method of the modular battery is quite promising in simulations. However, an experimental validation is still required for large battery packs. In addition, an appropriate module size and the extra losses due to additional electronic components (power switches, gate drivers, and instrumentation for each module) require thorough investigation to assess the overall benefit of the modular battery. Nevertheless, this conceptual study has shown that the simultaneous balancing of SOC and temperature, which has never been formally considered before, is feasible using simple control methods.

In the end, we would like to conclude with the following major "non-technical" problems we faced while setting up this study:

- It was initially challenging to understand the lithium-ion battery ageing factors to properly motivate the need of simultaneous thermal and SOC balancing. There is a plethora of battery ageing literature, but ageing phenomena are still not completely understood and sometimes studies even conflict each other. Therefore, we had to spend significant amount of time on this literature survey.

- It was not easy to find proper simulation setup because cells with different parameter values may be combined in many configurations, which itself becomes an optimization problem. In addition, the realistic data for battery load profile, cell parameters, and coolant parameters were not easily accessible.

Chapter 11

Future Work

Our quest to develop model-based controllers for optimal load management of the modular battery, and to understand the control behavior, has generated many interesting open research questions listed below:

1. More about balancing feasibility/potential/characterization:

    a. How to characterize the least cell redundancy needed to achieve cell balancing for a given drive cycle? This question boils down to sizing of battery pack not only considering power and energy demands but also considering the balancing demands under worst driving scenario.

    b. The above question can be flipped as follows: How to characterize the level of load variations needed to achieve balancing for a given battery size? This question boils down to determining the driving style that is best for balancing.

    c. What is the maximum duration and amplitude of a constant current pulse during which thermal and SOC balancing constraints will not be violated? The length of the pulse period depends on the pulse magnitude, cell electrical and thermal time constants, steady-state gains, and the initial condition of electro-thermal state.

    d. How to assess the balancing potential of a drive cycle for a given pack size? In other words, we are interested to estimate the balancing time k_b (defined on page 58) of a modular battery with non-zero initial balancing errors for a given drive cycle.

2. More about control design and analysis:

    a. The voltage controller proposed in this thesis is a feedforward type and is, thus, prone to errors under modeling and estimation uncertainty. We recommend to develop a control scheme in which this feedforward controller works with inner feedback voltage control loop with fast sampling to compensate the errors.

b. The modular battery can be used as a variable voltage source during charging to control current. In this case, we need to define current i_L as a state. The question is how to design control algorithm for this operation. This is not a simple extension of the proposed control algorithms because the state-dynamics becomes bilinear ($i_L u$, $i_L^2 u$) in nature, making the problem nonconvex.

c. The modular battery allows complete bypassing of a faulty module. However, we need to develop fault detection and diagnosis algorithm (supervisor/master) at the higher layer, which can communicate with cell controllers (slaves) at lower layer. This will make it possible to operate the vehicle in the limp mode (reduced battery voltage).

d. The modular battery can synthesize a range of dc-link voltages. The dc-link voltage need not be constant as it can be generated as a function of electric machine speed and torque. Therefore, it is interesting to develop a control algorithm, which decides the dc-link voltage that is good for electric drive (inverter + machine) as well the battery balancing. To achieve this, the balancer and the drive need to communicate with each other.

e. The modular battery provides a great opportunity for distributed battery management and cooling at the module level. For this purpose, the distributed control/optimization methods need to be investigated. We suggest a two-layer control structure: the outer layer with supervisory control and the inner layer with local feedback voltage and balancing controllers.

f. Stability or robust control-invariant set analysis of one-step MPC based balancing controller is a challenging but an interesting research problem. The main goal is to derive conditions under which temperature and SOC balancing errors can be guaranteed to stay inside the target set.

g. Formulate the balancing controller using LMI/LPV-based robust control techniques and analyse the balancing performance under uncertain state and parameter estimates.

3. Towards cost-benefit analysis, circuit topologies, and implementation:

a. How to choose suitable battery module size considering the semiconductor losses (efficiency analysis) and the instrumentation cost in large battery packs? This question in essence boils down to cost-benefit analysis of the modular battery. The benefit of the modular battery compared to the conventional battery need to be ideally measured in terms of increase in battery energy/power capacity (e-range/driveability) and the battery lifetime.

b. Thermal and SOC balancing can also be achieved using shunt-converter across each cell in a battery string. This configuration requires extra high-power dc/dc converter to regulate the dc-link voltage whereas the modular battery configuration considered in this thesis requires converter with higher current capability inside each module. Therefore, it will be interesting to compare these two battery configurations in terms of their cost, energy efficiency, and balancing speeds.

c. A compact design of the battery module with integrated converter, modulator, instrumentation, signal conditioning, communication interface, cooling, and microcontroller unit is a challenging practical problem on power electronics side.

4. Towards advanced models:

    a. We recommend to study the load management problem of modular batteries in the context of battery state-of-energy (SOE), state-of-power (SOP), and state-of-health (SOH). An interesting question is: How much can we improve SOE, SOP, and SOH through optimal control of modular batteries?

    b. Use enhanced Thevenin electrical model to analyze the effect of polarization losses (neglected in this thesis). The inclusion of the polarization states gives rise to the bilinear terms $(x \cdot u)$ in the voltage output equation, which may pose some challenges.

    c. Modeling of OCV hysteresis and c-rate dependent capacity of cells. These factors may affect the balancing control decisions.

    d. The unequal load distribution among battery modules would also generate unequal losses on converters, which might lead to their nonuniform ageing. Therefore, it might be interesting to include converter loss models in the optimization and analyze the trade-off between battery and converter lifetime.

Appendices

Appendix A

Battery Glossary

This appendix reviews the basic battery terminology, see [60] for details. In section A.1 various classes of batteries are reviewed, main components of any battery and the battery terminology are discussed in section A.2 and A.3 respectively.

A.1 Classification of Batteries

The batteries can be classified in many ways. In the following, two types of classifications are given.

A.1.1 Classification 1

This classification of cells is based on their power to energy ratio.

Power Cells or Energy Cells

There is always a trade-off between power and energy of cells. The batteries can be either high-power or high-energy but not both. This limitation comes from electrode material. A high-power cell needs a large number of thinner electrodes and thicker current collector to ensure efficient electronic conduction whereas high-energy cell needs a small number of thicker electrodes and thinner current collectors to achieve higher amount of active material. The small number of thicker electrodes increase the over-all surface area of electrodes which facilitates the large number of atoms of active materials to take part in chemical redox reaction. The cell manufacturer normally categorize their cells according to this classification.

A.1.2 Classification 2

In this classification cells are classified according to their re-chargeability.

Primary Cells

Primary cells are not capable of being charged electrically. Energy is stored inside them once during cell manufacturing and they are discarded when they are fully drained. These cells normally have a quite high energy density and shelf-life.

Secondary Cells

Secondary cells (also known as rechargeable cells) are capable of being charged after they are fully drained. Secondary batteries are used for storage of electrical energy and are thus also known as "storage batteries" or "accumulators". The one of the most desired characteristic of secondary batteries is the long cycle-life. In order to achieve long cycle-life, the charge and discharge of battery should be highly efficient with minimum irreversible capacity loss during transformation of chemical energy to electrical energy and vice versa. In addition, secondary cells should also have other desired characteristics like high energy and power density, high discharge rates, low impedance, low leakage current (i.e. long shelf-life), and good performance over wide temperature range. Due to all these stringent requirements there are only few materials which can be employed in secondary cells. The most common types of secondary cells include lead-acid (PbA), nickel-cadmium (NiCd), nickel-metal hydride (NiMH) and the lithium-ion (LIB). The rechargeable batteries normally have higher power density compared to primary batteries and are thus capable of handling relatively very high discharge rates. However, the energy density and shelf-life of most secondary cells are lower than those of primary cells except rechargeable LIBs which have very high energy density, shelf-life as well as very long cycle-life.

A.2 Main Battery Components

A cell consists of various parts which are briefly reviewed below [60].

Anode and Cathode

Strictly speaking, in *electrochemical convention*, the anode is an electrode in a cell where oxidation takes place i.e. where atom *loses* electron and *increases* its oxidation number. Thus during discharge, the negative electrode is the anode whereas during charge the positive electrode is the anode.

Similarly, the cathode is an electrode in a cell where reduction takes place i.e. where atom *gains* electron and *reduces* its oxidation number. Thus during discharge, the positive electrode is the cathode whereas during charge the negative electrode is the cathode.

This strict naming convention may create confusion, therefore in most of the battery literature the *battery convention* is followed where the names of electrodes are fixed according to discharge process. Thus, the negative electrode is commonly called anode and positive electrode is normally called cathode.

Electrolyte

The medium inside the cell which provides the mechanism for transport of ions between anode and cathode of a cell.

Electrolyte Additives

The side reactions between electrolyte and electrodes result in capacity loss. The presence of impurity such as water inside electrolyte can also lead to capacity loss. Moreover, electrolytes may be highly flammable, like for example in LIB, and pose a great safety hazard. These problems can be mitigated by using very high-purity electrolytes as well as by using some organic or inorganic additives inside electrolytes.

Current Collectors

A part of the electrode which does not take part in chemical reaction but is a very good electronic conductor. It is used to conduct electronic current from the anode to cathode through the external circuit during discharge and the reverse during charge.

Separator

The separator is a material which is placed inside the cell as a spacer between anode and cathode to prevent the internal short-circuit between them. The separator is electronically non-conductive but it has very high permeability for ions.

A.3 Battery Terminology and Metrics

In this section, definitions of some battery related terms will be given.

A.3.1 Cell, Sub-Modules, Modules and Packs

A cell is the most basic and smallest packaged form of a battery. The voltage output from a cell normally ranges from 1.35V (NiCd) to 4V (LIB). A battery sub-module (BSM) is collection of two or more cells connected in series and a battery module (BM) is a collection of two or more BSMs connected in series or parallel to get higher energy or power or both. A battery pack (BP) is a collection of several BMs connected in series and parallel to meet voltage, energy and power requirements.

A.3.2 Functional and Performance Metrics

Cell Capacity

The total amount of charge, stored inside the active mass of electrodes, that can be delivered by a cell under certain operating conditions. There are various definitions of cell capacity. These definitions differ based on the operating conditions (i.e. end-of-discharge-voltage (EODV), end-of-charge-voltage (EOCV), rate of discharge, ambient temperature etc.) of a cell.

- The theoretical capacity C_t is the maximum number of ampere-hours (charge) that can be *theoretically extracted* from a cell *based only on the amount of active material* it contains. In this rating, we do not consider the conditions under which battery is operating.

- The rated capacity C_r is the maximum number of ampere-hours that a fully charged *fresh* cell can deliver *under standard operating conditions specified by a manufacturer* (i.e. EODV, rate of discharge, ambient temperature).

- The practical (or actual) capacity C_p is the maximum number of ampere-hours (charge) that can be *actually delivered* by a *fully* charged cell while discharging *under non-standard discharge conditions* to the *standard EODV*.

- The dischargeable (or available or releasable) cell capacity C_d is the portion of practical capacity that can be obtained from a cell at the user defined discharge rates and other specified operating conditions like initial SOC level and EODV.

- The chargeable capacity C_c of a cell is the used cell capacity that can be charged. The chargeable cell capacity is also called absorbable or used cell capacity.

Cell Energy

Cell energy is obtained by multiplying cell output voltage with its capacity. As we have various metrics for cell capacity thus we have various metrics for cell energy as well like theoretical energy, rated energy, practical energy, and available energy.

Battery Pack Capacity

The pack capacity is the maximum number of available ampere-hours that can be released from a fully charged state of a Cell_x in the battery pack to a fully discharged state of the same or some other Cell_y in the battery pack under specified operating conditions. In other words, the pack capacity can also be defined as the sum of dischargeable and chargeable pack capacities which are defined below.

- The maximum dischargeable (or available) capacity of a BP is given by a cell in a pack with the minimum remaining cell capacity that can be discharged.
- The maximum chargeable (or Used) capacity of a BP is given by a cell in a pack with the minimum used cell capacity that can be charged.

Remark A.1. *If the battery pack is assumed to be in the fully charged state then the pack total capacity is simply given by that cell which has the minimum dischargeable capacity in the whole fully charged pack.*

Cell State-of-Charge

The cell SOC at any time 't' refers to the dischargeable cell capacity as a percentage of some reference. Most commonly, the total actual capacity of a cell is used as a reference.

$$SOC(t) = \frac{C_d(t)}{C_p(t)} \tag{A.1}$$

The SOC describes how the battery at time 't' is different, in terms of its currently available energy content, from that of its fully charged state. The SOC of a fully charged cell, whether fresh or aged, is always equal to 1.

Cell Depth-of-Discharge

The depth-of-discharge (DOD) of a cell at a given time is a ratio between the quantity of charge (ampere-hour) removed from a cell up to that time instant and the actual capacity (in some literatures rated capacity is used as well) of a cell. It is expressed as a percentage (0% = full, 100% = empty). A cell will be considered under a deep discharge when it is discharged to at least 80% DOD.

Theoretical Cell Voltage

Theoretical cell voltage is the voltage output from a cell under equilibrium conditions i.e. when no current is being drawn or delivered from a cell. It is also called open-circuit or equilibrium voltage and is denoted by V_{oc}.

Cell Polarizations and Losses

The cell polarization is the deviation of cell output voltage from its theoretical voltage. The measure of the magnitude of the polarization is called over-potential. In a cell, ideally all the electrochemical energy should get converted to electrical energy. However, some losses occur due to polarization effects when the external load current passes through the electrodes and the electrochemical reactions (called electrode reactions) take place at electrodes. The electrode processes consist of the electrode reaction and the mass transport process (or charge transport). The electrode reaction is a solid/electrolyte interfacial reaction that involves various process but the main step is the charge transfer reaction. The polarization effects appear in a cell due to kinetic limitations of these steps in electrode reaction. These polarization effects inside a cell consumes some part of the chemical energy stored inside electrodes and dissipate it as heat. Thus, all the theoretical energy, which is calculated based on active materials in electrodes, of a cell is not converted into electrical energy and therefore the cell performance is degraded. Thus, the voltage output from a cell under operation is given by

$$V_B = V_{oc} - V_{op} - V_{cp} - V_{ap} \tag{A.2}$$

where V_{oc} is open-circuit voltage, V_{op} is ohmic polarization (or over-potential), V_{cp} is the concentration polarization, and V_{ap} is the activation polarization of the cell which are respectively defined as follows.

- The voltage drop inside a cell due to internal ohmic resistance is called ohmic polarization. This voltage drop is proportional to load current and thus follows the ohm's law.
- The activation polarization appears due to limitation of charge-transfer reaction kinetics. The activation polarization is dynamic in nature and thus it does not develop or collapse instantly. In equivalent circuit cell models, this behavior is modeled using a parallel RC branch.

- The concentration polarization is the potential difference across the diffusion layer on the electrode/electrolyte interface (interfacial region). It develops due to concentration gradient across the diffusion layer. It develops due to limitation of charge-transport kinetics. The concentration polarization is also dynamic in nature however it has slower dynamics compared to activation polarization because the charge-transport happens through the diffusion process which is a slower process than charge transfer reaction. In equivalent circuit approach, this behavior is also modeled using a parallel RC branch.

Battery Cycle

The full battery cycle is the discharge of a fully charged battery followed or preceded by the charging process such that the battery is restored to its original initial condition. The cycle is called deep-discharged cycle if at least 80% of the battery energy is consumed otherwise it is called shallow (or micro or flat) cycle.

C-Rate

The c-rate of a charing or discharging current is the ratio of the battery current to the rated capacity of a cell

$$c = \frac{I_B}{C_r} \tag{A.3}$$

A cell discharging at 1 c-rate will be completely discharged in one hour.

Total Ah Throughput

The total amount of charge processed (delivered or absorbed) by a cell before its EOL.

A.3.3 Battery Life-time and Ageing Terms

Cell ages when they are used. There are various metrics and terms which are used in this context, some of them are defined below.

Calendar Life

Calendar ageing is the proportion of irreversible capacity loss that occurs with time especially during storage. The expected lifespan (in time) of a cell under storage (or periodic cycling) conditions is called calendar-life.

Cycle Life

Cycle life is the number of charge/discharge cycles that a cell can undergo, under specified conditions, before its end-of-life (EOL). Various performance limits can be used to mark EOL. For example, when the practical cell capacity falls below minimum desired level of 80% of rated capacity.

State-of-Health

State-of-health (SOH) is a unitless quantity used to measure the current condition of a cell *relative to a fresh cell.* There are various cell parameters which vary with cell age and thus can be used to indicate the SOH of a cell. However, the SOH based on capacity loss is normally used as given below

$$SOH = \frac{\text{Maximum capacity of an aged cell}}{\text{Maximum capacity of a fresh cell}} = \frac{C_p}{C_r} \tag{A.4}$$

The SOH describes how a battery at time 't' is different, in terms of its fully charged energy content, from that of a fresh cell.

References

[1] C. Chan and Y. S. Wong, "Electric vehicles charge forward," *Power and Energy Magazine, IEEE*, vol. 2, no. 6, pp. 24–33, 2004.

[2] M. Ehsani, Y. Gao, and A. Emadi, *Modern electric, hybrid electric, and fuel cell vehicles: fundamentals, theory, and design.* CRC press, 2009.

[3] K. Ç. Bayindir, M. A. Gözüküçük, and A. Teke, "A comprehensive overview of hybrid electric vehicle: Powertrain configurations, powertrain control techniques and electronic control units," *Energy Conversion and Management*, vol. 52, no. 2, pp. 1305–1313, 2011.

[4] "USABC Goals for Advanced Batteries for EVs," *US Advanced Battery Consortium (USABC)*, 2006.

[5] "USABC Energy Storage Goals for Power-Assist HEVs," *US Advanced Battery Consortium (USABC), FreedomCAR*, 2002.

[6] A. A. Pesaran, T. Markel, H. S. Tataria, and D. Howell, *Battery Requirements for Plug-in Hybrid Electric Vehicles–analysis and Rationale.* National Renewable Energy Laboratory, 2009.

[7] R. Dell, "Batteries: fifty years of materials development," *Solid State Ionics*, vol. 134, no. 1-2, pp. 139–158, 2000.

[8] S. G. Chalk and J. F. Miller, "Key challenges and recent progress in batteries, fuel cells, and hydrogen storage for clean energy systems," *Journal of Power Sources*, vol. 159, no. 1, pp. 73–80, 2006.

[9] M. Armand and J.-M. Tarascon, "Building better batteries," *Nature*, vol. 451, no. 7179, pp. 652–657, 2008.

[10] N. Terada, T. Yanagi, S. Arai, M. Yoshikawa, K. Ohta, N. Nakajima, A. Yanai, and N. Arai, "Development of lithium batteries for energy storage and ev applications," *Journal of Power Sources*, vol. 100, no. 1, pp. 80–92, 2001.

[11] C. A. Vincent, "Lithium batteries: a 50-year perspective, 1959–2009," *Solid State Ionics*, vol. 134, no. 1-2, pp. 159–167, 2000.

[12] J.-M. Tarascon and M. Armand, "Issues and challenges facing rechargeable lithium batteries," *Nature*, vol. 414, no. 6861, pp. 359–367, 2001.

[13] E. Karden, S. Ploumen, B. Fricke, T. Miller, and K. Snyder, "Energy storage devices for future hybrid electric vehicles," *Journal of Power Sources*, vol. 168, no. 1, pp. 2–11, 2007.

[14] A. Barré, B. Deguilhem, S. Grolleau, M. Gérard, F. Suard, and D. Riu, "A review on lithium-ion battery ageing mechanisms and estimations for automotive applications," *Journal of Power Sources*, vol. 241, no. 0, pp. 680 – 689, 2013.

[15] M. Broussely, P. Biensan, F. Bonhomme, P. Blanchard, S. Herreyre, K. Nechev, and R. Staniewicz, "Main aging mechanisms in li ion batteries," *Journal of Power Sources*, vol. 146, no. 1, pp. 90–96, 2005.

[16] J. Vetter, P. Novak, M. Wagner, and et.el., "Ageing mechanisms in lithium-ion batteries," *Journal of power sources*, vol. 147, no. 1, pp. 269–281, 2005.

[17] J. Wang, P. Liu, Hicks-Garner, and et.el., "Cycle-life model for graphite-$LiFePO_4$ cells," *Journal of Power Sources*, vol. 196, no. 8, pp. 3942–3948, 2011.

[18] J. Groot, *State-of-Health Estimation of Li-ion Batteries: Ageing Models*, ser. PhD Thesis. New Series, no: 3815. Chalmers University of Technology, 2014.

[19] S. Paul, C. Diegelmann, H. Kabza, and W. Tillmetz, "Analysis of ageing inhomogeneities in lithium-ion battery systems," *Journal of Power Sources*, 2013.

[20] M. Dubarry, N. Vuillaume, and B. Y. Liaw, "Origins and accommodation of cell variations in li-ion battery pack modeling," *International Journal of Energy Research*, vol. 34, no. 2, pp. 216–231, 2010.

[21] T. M. Bandhauer, S. Garimella, and T. F. Fuller, "A critical review of thermal issues in lithium-ion batteries," *Journal of the Electrochemical Society*, vol. 158, no. 3, pp. R1–R25, 2011.

[22] B. Wu, V. Yufit, M. Marinescu, G. J. Offer, R. F. Martinez-Botas, and N. P. Brandon, "Coupled thermal-electrochemical modelling of uneven heat generation in lithium-ion battery packs," *Journal of Power Sources*, 2013.

[23] R. Mahamud and C. Park, "Reciprocating air flow for li-ion battery thermal management to improve temperature uniformity," *Journal of Power Sources*, vol. 196, no. 13, pp. 5685 – 5696, 2011.

[24] V. Viswanathan and M. Kintner-Meyer, "Second use of transportation batteries: Maximizing the value of batteries for transportation and grid services," *Vehicular Technology, IEEE Transactions on*, vol. 60, no. 7, pp. 2963–2970, Sept 2011.

[25] S. J. Moura, "Techniques for battery health conscious power management via electrochemical modeling and optimal control," Ph.D. dissertation, University of Michigan, 2011.

[26] S. Moura, J. Siegel, D. Siegel, H. Fathy, and A. Stefanopoulou, "Education on vehicle electrification: Battery systems, fuel cells, and hydrogen," in *Vehicle Power and Propulsion Conference (VPPC), 2010 IEEE*, 2010, pp. 1–6.

[27] S. Moura, J. Stein, and H. Fathy, "Battery-health conscious power management in plug-in hybrid electric vehicles via electrochemical modeling and stochastic control," *Control Systems Technology, IEEE Transactions on*, vol. 21, no. 3, pp. 679–694, May 2013.

[28] S. Moura, N. Chaturvedi, and M. Krstic, "Constraint management in li-ion batteries: A modified reference governor approach," in *American Control Conference (ACC), 2013*, 2013, pp. 5332–5337.

[29] S. Moura, J. Forman, S. Bashash, J. Stein, and H. Fathy, "Optimal control of film growth in lithium-ion battery packs via relay switches," *Industrial Electronics, IEEE Transactions on*, vol. 58, no. 8, pp. 3555–3566, 2011.

[30] L. Tang, G. Rizzoni, and S. Onori, "Energy management strategy for HEVs including battery life optimization," *IEEE Transactions on Transportation Electrification*, vol. 1, no. 3, pp. 211–222, Oct 2015.

[31] C. D. Rahn and C.-Y. Wang, *Battery systems engineering.* John Wiley & Sons, 2012.

[32] N. Chaturvedi, R. Klein, J. Christensen, J. Ahmed, and A. Kojic, "Algorithms for advanced battery-management systems," *Control Systems, IEEE*, vol. 30, no. 3, pp. 49–68, 2010.

[33] K. B. Hatzell, A. Sharma, and H. K. Fathy, "A survey of long-term health modeling, estimation, and control of lithium-ion batteries: Challenges and opportunities," in *2012 American Control Conference (ACC)*, June 2012, pp. 584–591.

[34] K. A. Smith, C. D. Rahn, and C.-Y. Wang, "Control oriented 1d electrochemical model of lithium ion battery," *Energy Conversion and Management*, vol. 48, no. 9, pp. 2565–2578, 2007.

[35] X. Lin, H. E. Perez, S. Mohan, J. B. Siegel, A. G. Stefanopoulou, Y. Ding, and M. P. Castanier, "A lumped-parameter electro-thermal model for cylindrical batteries," *Journal of Power Sources*, vol. 257, pp. 1 – 11, 2014.

[36] X. Lin, H. Fu, H. E. Perez, and et.el., "Parameterization and observability analysis of scalable battery clusters for onboard thermal management," *Oil & Gas Science and Technology–Revue d'IFP Energies nouvelles*, vol. 68, no. 1, pp. 165–178, 2013.

[37] X. Lin, H. Perez, J. Siegel, A. Stefanopoulou, and et.el., "Online parameterization of lumped thermal dynamics in cylindrical lithium ion batteries for core temperature estimation and health monitoring," *Control Systems Technology, IEEE Transactions on*, vol. 21, no. 5, pp. 1745–1755, Sept 2013.

[38] A. Cordoba-Arenas, S. Onori, and G. Rizzoni, "A control-oriented lithium-ion battery pack model for plug-in hybrid electric vehicle cycle-life studies and system design with consideration of health management," *Journal of Power Sources*, vol. 279, pp. 791 – 808, 2015.

[39] G. L. Plett, "Extended kalman filtering for battery management systems of lipb-based HEV battery packs: Part 1. background," *Journal of Power Sources*, vol. 134, no. 2, pp. 252 – 261, 2004.

[40] ——, "Extended kalman filtering for battery management systems of lipb-based HEV battery packs: Part 2. modeling and identification," *Journal of Power Sources*, vol. 134, no. 2, pp. 262 – 276, 2004.

[41] ——, "Extended kalman filtering for battery management systems of lipb-based HEV battery packs: Part 3. state and parameter estimation," *Journal of Power Sources*, vol. 134, no. 2, pp. 277 – 292, 2004.

[42] J. Gallardo-Lozano, Romero-Cadaval, and et.el., "Battery equalization active methods," *Journal of Power Sources*, vol. 246, pp. 934–949, 2014.

[43] W. C. Lee, D. Drury, and P. Mellor, "Comparison of passive cell balancing and active cell balancing for automotive batteries," in *Vehicle Power and Propulsion Conference (VPPC), 2011 IEEE*, sept. 2011, pp. 1 –7.

[44] J. Cao, N. Schofield, and A. Emadi, "Battery balancing methods: A comprehensive review," in *Vehicle Power and Propulsion Conference, 2008. VPPC '08. IEEE*, sept. 2008, pp. 1 –6.

[45] W. Bentley, "Cell balancing considerations for lithium-ion battery systems," in *Battery Conference on Applications and Advances, 1997., 12th Annual*, jan 1997, pp. 223 –226.

[46] P. Krein, "Battery management for maximum performance in plug-in electric and hybrid vehicles," in *Vehicle Power and Propulsion Conference, 2007. VPPC 2007. IEEE*, sept. 2007, pp. 2 –5.

[47] J. Barreras, C. Pinto, and et.al., "Multi-objective control of balancing systems for li-ion battery packs: A paradigm shift?" in *Vehicle Power and Propulsion Conference (VPPC), 2014 IEEE*, Oct. 2014.

[48] M. Malinowski, K. Gopakumar, J. Rodriguez, and M. Pérez, "A survey on cascaded multilevel inverters," *Industrial Electronics, IEEE Transactions on*, vol. 57, no. 7, pp. 2197 –2206, july 2010.

[49] K. Wilkie, D. Stone, C. Bingham, and M. Foster, "Integrated multilevel converter and battery management," in *Power Electronics, Electrical Drives, Automation and Motion, 2008. SPEEDAM 2008. International Symposium on*, june 2008, pp. 756 –759.

[50] A. Manenti, A. Abba, A. Merati, S. Savaresi, and A. Geraci, "A new bms architecture based on cell redundancy," *Industrial Electronics, IEEE Transactions on*, vol. 58, no. 9, pp. 4314–4322, 2011.

[51] W. Huang and J. Abu Qahouq, "Energy sharing control scheme for state-of-charge balancing of distributed battery energy storage system," *Industrial Electronics, IEEE Transactions on*, vol. 62, no. 5, pp. 2764–2776, May 2015.

[52] M. A. Xavier and M. S. Trimboli, "Lithium-ion battery cell-level control using constrained model predictive control and equivalent circuit models," *Journal of Power Sources*, vol. 285, pp. 374 – 384, 2015.

[53] Z. Zheng, K. Wang, L. Xu, and Y. Li, “A hybrid cascaded multilevel converter for battery energy management applied in electric vehicles,” *Power Electronics, IEEE Transactions on*, vol. 29, no. 7, pp. 3537–3546, July 2014.

[54] Y. Li and Y. Han, “A module-integrated distributed battery energy storage and management system,” *Power Electronics, IEEE Transactions on*, vol. PP, no. 99, pp. 1–1, 2016.

[55] T. Soong and P. Lehn, “Evaluation of emerging modular multilevel converters for bess applications,” *Power Delivery, IEEE Transactions on*, vol. 29, no. 5, pp. 2086–2094, Oct 2014.

[56] C.-M. Young, N.-Y. Chu, L.-R. Chen, Y.-C. Hsiao, and C.-Z. Li, “A single-phase multilevel inverter with battery balancing,” *Industrial Electronics, IEEE Transactions on*, vol. 60, no. 5, pp. 1972–1978, 2013.

[57] O. Josefsson, A. Lindskog, S. Lundmark, and T. Thiringer, “Assessment of a multilevel converter for a PHEV charge and traction application,” in *Electrical Machines (ICEM), 2010 XIX International Conference on*, sept. 2010, pp. 1 –6.

[58] O. Josefsson, *Investigation of a Multilevel Inverter for Electric Vehicle Applications*, ser. Doktorsavhandlingar vid Chalmers tekniska högskola. Ny serie, no:. Department of Energy and Environment, Electric Power Engineering, Chalmers University of Technology,, 2015, 146.

[59] F. Altaf, *Thermal and State-of-Charge Balancing of Batteries using Multilevel Converters.* Licentiate Thesis, Department of Signals and Systems, Automatic Control, Chalmers University of Technology, 2014. [Online]. Available: http://publications.lib.chalmers.se/publication/194660/194660.pdf

[60] T. Reddy, *Linden's Handbook of Batteries, 4th Edition*, 4th ed. McGraw-Hill Professional, 10 2010.

[61] P. Liu, J. Wang, J. Hicks-Garner, E. Sherman, S. Soukiazian, M. Verbrugge, H. Tataria, J. Musser, and P. Finamore, “Aging mechanisms of lifepo4 batteries deduced by electrochemical and structural analyses,” *Journal of the Electrochemical Society*, vol. 157, no. 4, pp. A499–A507, 2010.

[62] B. Scrosati and J. Garche, “Lithium batteries: Status, prospects and future,” *Journal of Power Sources*, vol. 195, no. 9, pp. 2419–2430, 2010.

[63] P. Ramadass, B. Haran, P. M. Gomadam, R. White, and B. N. Popov, "Development of first principles capacity fade model for li-ion cells," *Journal of The Electrochemical Society*, vol. 151, no. 2, pp. A196–A203, 2004.

[64] P. Ramadass, B. Haran, R. White, and B. N. Popov, "Mathematical modeling of the capacity fade of li-ion cells," *Journal of Power Sources*, vol. 123, no. 2, pp. 230–240, 2003.

[65] K. Smith, J. Neubauer, E. Wood, M. Jun, and A. Pesaran, "Models for battery reliability and lifetime," 2013.

[66] M. Ecker, J. B. Gerschler, J. Vogel, S. Käbitz, F. Hust, P. Dechent, and D. U. Sauer, "Development of a lifetime prediction model for lithium-ion batteries based on extended accelerated aging test data," *Journal of Power Sources*, vol. 215, pp. 248–257, 2012.

[67] M. Broussely, S. Herreyre, P. Biensan, P. Kasztejna, K. Nechev, and R. Staniewicz, "Aging mechanism in li ion cells and calendar life predictions," *Journal of Power Sources*, vol. 97, pp. 13–21, 2001.

[68] R. Darling and J. Newman, "Modeling side reactions in composite $Li_yMn_2O_4$ electrodes," *Journal of The Electrochemical Society*, vol. 145, no. 3, pp. 990–998, 1998.

[69] A. V. Randall, R. D. Perkins, X. Zhang, and G. L. Plett, "Controls oriented reduced order modeling of solid-electrolyte interphase layer growth," *Journal of Power Sources*, vol. 209, pp. 282–288, 2012.

[70] G. L. Plett, "Algebraic solution for modeling sei layer growth," *ECS Electrochemistry Letters*, vol. 2, no. 7, pp. A63–A65, 2013.

[71] D. Andre, C. Appel, T. Soczka-Guth, and D. U. Sauer, "Advanced mathematical methods of soc and soh estimation for lithium-ion batteries," *Journal of Power Sources*, 2012.

[72] L. Lu, X. Han, J. Li, J. Hua, and M. Ouyang, "A review on the key issues for lithium-ion battery management in electric vehicles," *Journal of Power Sources*, vol. 226, pp. 272–288, 2013.

[73] Y. Zheng, M. Ouyang, L. Lu, J. Li, X. Han, and L. Xu, "On-line equalization for lithium-ion battery packs based on charging cell voltages: Part 1. equalization based on remaining charging capacity estimation," *Journal of Power Sources*, vol. 247, pp. 676–686, 2014.

[74] L. Zhong, C. Zhang, Y. He, and Z. Chen, “A method for the estimation of the battery pack state of charge based on in-pack cells uniformity analysis,” *Applied Energy*, vol. 113, pp. 558–564, 2014.

[75] Y. Zheng, L. Lu, X. Han, J. Li, and M. Ouyang, “Lifepo4 battery pack capacity estimation for electric vehicles based on charging cell voltage curve transformation,” *Journal of Power Sources*, 2013.

[76] W. Bentley, “Cell balancing considerations for lithium-ion battery systems,” in *Battery Conference on Applications and Advances, 1997., Twelfth Annual*. IEEE, 1997, pp. 223–226.

[77] P. A. Cassani and S. S. Williamson, “Significance of battery cell equalization and monitoring for practical commercialization of plug-in hybrid electric vehicles,” in *Applied Power Electronics Conference and Exposition, 2009. APEC 2009. Twenty-Fourth Annual IEEE*. IEEE, 2009, pp. 465–471.

[78] D. Andrea, *Battery Management Systems for Large Lithium Ion Battery Packs*, 1st ed. Artech House, 2010.

[79] F. Altaf, *Thermal and State-of-Charge Balancing of Batteries using Multilevel Converters*. Licentiate Thesis, Chalmers University of Technology, 2014. [Online]. Available: http://publications.lib.chalmers.se/records/fulltext/194660/194660.pdf

[80] C.-H. Kim, M. young Kim, H. sun Park, and G.-W. Moon, “A modularized two-stage charge equalizer with cell selection switches for series-connected lithium-ion battery string in an hev,” *Power Electronics, IEEE Transactions on*, vol. 27, no. 8, pp. 3764–3774, 2012.

[81] M. Preindl, C. Danielson, and F. Borrelli, “Performance evaluation of battery balancing hardware,” in *Control Conference (ECC), 2013 European*. IEEE, 2013, pp. 4065–4070.

[82] R. Elger, “On the behaviour of the lithium ion battery in the hev application,” Ph.D. dissertation, KTH Royal Institute of Technology, 2004.

[83] J. Newman and W. Tiedemann, “Porous-electrode theory with battery applications,” *AIChE Journal*, vol. 21, no. 1, pp. 25–41, 1975.

[84] X. Hu, S. Li, and H. Peng, “A comparative study of equivalent circuit models for li-ion batteries,” *Journal of Power Sources*, vol. 198, no. 0, pp. 359 – 367, 2012.

[85] S. Al Hallaj, R. Venkatachalapathy, J. Prakash, and J. Selman, "Entropy changes due to structural transformation in the graphite anode and phase change of the licoo2 cathode," *Journal of the Electrochemical Society*, vol. 147, no. 7, pp. 2432–2436, 2000.

[86] K. Smith and C.-Y. Wang, "Power and thermal characterization of a lithium-ion battery pack for hybrid-electric vehicles," *Journal of power sources*, vol. 160, no. 1, pp. 662–673, 2006.

[87] R. Steinbrecher, A. Radmehr, K. M. Kelkar, and S. V. Patankar, "Use of flow network modeling (fnm) for the design of air-cooled servers," in *Advances in Electronics Packaging, Proceedings of the Pacific RIM/ASME Intersociety Electronics and Photonic Packaging Conference*, vol. 2, 1999, pp. 1999–2008.

[88] T. L. Bergman, F. P. Incropera, and A. S. Lavine, *Fundamentals of heat and mass transfer*. John Wiley & Sons, 2011.

[89] F. Altaf, L. Johannesson, and B. Egardt, "On Thermal and State-of-Charge Balancing using Cascaded Multi-level Converters," *Journal of Power Electronics*, vol. 13, no. 4, pp. 569–583, July 2013.

[90] J. Rawlings, "Tutorial overview of model predictive control," *Control Systems, IEEE*, vol. 20, no. 3, pp. 38–52, Jun 2000.

[91] S. Karlsson, "The swedish car movement data project final report." Tech. Rep., 2013, 81.

[92] Test Site Sweden, "Vehicle research database," 2014. [Online]. Available: http://www.testsitesweden.eu/environment/vehicle-research-database

[93] K. Wipke, M. Cuddy, and S. Burch, "Advisor 2.1: a user-friendly advanced powertrain simulation using a combined backward/forward approach," *Vehicular Technology, IEEE Transactions on*, vol. 48, no. 6, pp. 1751–1761, Nov 1999.

[94] G. F. Franklin, J. D. Powell, and A. Emami-Naeini, *Feedback control of dynamics systems*, 4th ed. Prentice Hall, NJ, 2002.

[95] M. Grant and S. Boyd, "CVX: Matlab software for disciplined convex programming, version 1.21," Apr 2011.

[96] M. Grant, S. Boyd, and Y. Ye, "Disciplined convex programming," in *Global Optimization: From Theory to Implementation, Nonconvex Optimization and Its Application Series*. Springer, 2006, pp. 155–210.

[97] S. Boyd and L. Vandenberghe, *Convex Optimization.* Cambridge University Press, 2006.

[98] A. J. Laub, *Matrix analysis for scientists and engineers.* Siam, 2005.

[99] A. Domahidi, "FORCES: Fast optimization for real-time control on embedded systems," http://forces.ethz.ch, Oct. 2012.